Investigation of a Cluster of High-Power Helicon Thrusters for Advanced In-Space Electric Propulsion Applications

Keon L Vereen

A dissertation submitted in partial fulfillment

of the requirements for the degree of

Doctor of Philosophy

University of Washington

2019

Reading Committee:

Robert Winglee, Chair

Adam Bruckner

Brian Nelson

Program Authorized to Offer Degree:

Department of Aeronautics and Astronautics

University of Washington

Abstract

Investigation of a Cluster of High-Power Helicon Thrusters for Advanced In-Space Electric Propulsion Applications

Keon L Vereen

Chair of the Supervisory Committee:

Professor Robert Winglee

Earth and Space Sciences

The High-Power Helicon (HPH) cluster experiment aimed to investigate whether clustered helicon thrusters could outperform a single monolithic thruster in terms of beam collimation and exit velocities. The clustered HPH experiment operated at power levels $\geq$100 kW and could produce high energy, collimated plasma beams for in-space propulsion and beamed momentum applications. For this dissertation research, three magnetic flux conserving configurations were housed within a compact structural chassis in a space simulation facility. For variant 1 and 2 configurations, the thruster units were oriented at 12.7 degree off-parallel yaw angle and 15.8-degree pitch angle for single and double HPH operations. Magnetic nozzles were repositioned to measure the effect on downstream plume properties. For variant 3 configuration, the thruster units were oriented at 12.7 degree off-parallel yaw angle and 0.0-degree pitch angle for double HPH operations and slight axial adjustments of the magnetic nozzles. Variant 3

configuration was implemented to minimize potential plume asymmetries present in the initial architectural design.

Measurements were gathered using the double Langmuir probe, RF-compensated double Langmuir probe, time-of-flight probe, and nude Faraday probe at axial locations downstream of the Z = 0 source region. In the variant 1 configuration, the double HPH plasma density was measured as 50% larger than the sum of the left and right HPH thruster densities. In the variant 2 configuration, the single HPH operation yielded ion velocity and peak ion flux of 11 km/s and $1.29x10^{22}m^{-2}s^{-1}$ respectively. The double HPH operation yielded ion velocity and peak ion flux of 18.3 km/s and $9.15x10^{22}m^{-2}s^{-1}$ respectively. For variant 2 configuration, the double HPH peak ion flux was estimated as 256% (3.56-fold) larger than the sum of the left and right helicon thrusters. The radial profiles of plasma density and ion current density exhibited wide beam profiles, full width at half maximum (FWHM) of 35 cm and 37.5 cm respectively. In the variant 3 configuration, the double HPH operation yielded ion velocity and peak ion flux of 21.1 km/s and $1.56x10^{23}m^{-2}s^{-1}$ respectively. The double HPH peak ion flux was approximately 71% larger than the variant 2 configuration. Narrow beam profiles, FWHM of ~16 cm, were obtained from the radial plasma density and ion current density profiles. A narrower beam profile combined with an increase in peak ion flux could suggest an improvement in coupling mechanism. The results from this dissertation can be considered a 1st pass investigation into the clustering effects of helicon thrusters. Additional work is needed to develop two-dimensional mapping of the downstream clustered plume properties.

Table of Contents

List of Figures

List of Tables

List of Symbols and Acronyms

EP	Electric Propulsion
Isp	specific impulse
F	force or thrust
$\dot{m}_p$	propellant mass flow rate
g_0	acceleration due to Earth's gravity
v_e	exit velocity
ΔV	velocity increment
m_0	initial vehicle mass
m_f	final vehicle mass
m_p	propellant mass
EHT	electrothermal hydrazine thruster resistojet
NSSK	North-South Station Keeping
NEXT	NASA's Evolutionary Xenon Thruster
MPD	Magnetoplasmadynamic thruster
PPT	pulsed plasma thruster
HET	Hall-effect thruster
SPT	stationary plasma thruster
RF	radiofrequency
HDLT	Helicon Double Layer Thruster
VASIMR	Variable Specific Impulse Magnetoplasma Rocket
HPH	High-Power Helicon

W	watt
kW	kilowatts
ISS	International Space Station
PPU	power processing unit
HERMeS	Hall Effect Rocket with Magnetic Shielding
PPE	Power and Propulsion Element
R	Right-hand circularly polarized wave
ω_{c_i}	ion cyclotron frequency
ω_{c_e}	electron cyclotron frequency
ω_H	helicon gyration frequency
B	magnetic field vector
E	electric field vector
j	current density vector
m	azimuthal wave number
k_z	wave vector in axial z direction
ω	phase velocity
a	radius of the cylindrical source
B_0	base magnetic field scalar
n_0	plasma density scalar
PPA	plasma phased array
TRL	technology readiness level
IGBT	insulated gate bipolar transistor
FEMM	finite element method magnetics

OES	optical emission spectroscopy
RF-DLP	RF-compensated double Langmuir probe
DLP	double Langmuir probe
TOF	time-of-flight probe
$I_{i_{sat}}$	ion saturation current
e	electron charge
A_s	sheath area
k_B	Boltzmann constant
T_e	electron temperature
m_i	ion mass
RPA	retarding potential analyzer
RFEA	retarding field energy analyzer
IVDF	ion velocity distribution function
$< nv >$	ion flux
$I_c(V_d)$	collector current from RPA
A	probe area
$f(v)$	velocity space distribution function
v_i	ion velocity
V_d	discriminator voltage
θ	beam divergence half-angle
SEE	secondary electron emission
NFP	nude Faraday probe
ICP	inductively coupled plasma

SNR	signal-to-noise ratio
FWHM	full-width at half maximum
I – V	current – voltage curve
CEX	charge-exchange collisions
β	ratio of ion kinetic energy to magnetic pressure
PIC	particle-in-cell
PMFS	plasma momentum flux sensor
SEP	solar electric propulsion
NEP	nuclear electric propulsion
LEU	low-enriched uranium
LEO	low-Earth orbit
GEO	geosynchronous orbit
GTO	geosynchronous transfer orbit
GYO	graveyard orbit
NEA	near-Earth asteroid
NRHO	near rectilinear halo orbit

Acknowledgements

How does one even begin to say thank you to the numerous people who have helped me along my journey at the University of Washington? I will try. For me, thank you is an understatement of my deep appreciation to everyone who has contributed in a small or large part to my journey. I am incredible grateful for people sharing their time, energy, and resources to help me academically, professionally, and socially. It has meant a lot and I have attempted to pay in kind when working with young scholars interested in pursuing STEM degrees. Here are ≥100 kW worth of thank you!

First, a genuine thank you to my advisor, Professor Robert Winglee. Since my time joining the university, he has always had an open-door policy where I could come ask questions and seek constructive feedback. Working in his research group, he encouraged innovative thinking on everything, from the very small projects to the very large projects. He always asked the right questions and forced me to think really "really" big. As a result, I was able to work on a research project that was really challenging, but deeply meaningful as well. Even after setbacks on the many experimental campaigns, he would provide the words of encouragement…a shot in the arm…to propel me forward again. Thank you for your guidance and support.

Second, I would like to thank the other members of my supervisory committee, Adam Bruckner, Brian Fabien, Brian Nelson, and Justin Little, for providing me with technical and programmatic knowledge about plasmas, propulsion, and engineering design. Adam Bruckner always reminded me to never treat anything as a black box. Brian Nelson and I had many insightful chats on helicon sources, pulsed power experimentation, and diagnostics. Brian Fabien always encouraged me to think about the engineering design process in my projects. The

message of “keep it simple” allowed for fast prototyping while saving costs in the design to manufacturing process. Justin Little, as a new electric propulsion professor, provided insights on plasma thruster design and analysis techniques. His journal articles and dissertation on electrodeless plasma thrusters were extremely helpful as I redesigned the high-power helicon experiment. In addition, I would like to thank the administrative staffs from Earth & Space Sciences department, Aeronautics & Astronautics department, and Washington NASA Space Grant Consortium for their assistance over the many years. I would also like to thank the College of Engineering for allowing me the opportunity to teach and mentor students. I greatly enjoyed working with the staff and students from STARS, WiSE, and the Engineering Academic Centers over the many years. Even when experimental campaigns did not always go as planned, the teaching and learning sessions with students always reenergized me to keep going.

Third, I would like to thank our research partners, Eagle Harbor Technologies, for the in-kind technical support and loaned equipment over the many years. I greatly appreciate the timely advice from Tim Ziemba, James Prager, John Carscadden, Ken Miller and Kyle McEleney on resonant tank circuits, PCB board designs, high-voltage experimentation, and safety best practices. Your guidance allowed for me to maintain operationality of the seed plasma generators throughout my experimental test campaigns. Wishing you all continued growth in your business.

Fourth, I would like to thank my colleagues within the Advanced Propulsion Laboratory for support and guidance throughout this journey. Paige, Paul, and Manolo, thank you, for words of encouragement in the initial reboot days of the helicon experiment. It took longer than expected to get the thrusters into their characteristic blue discharges, but it was well worth it as nothing was a black box. Wishing you’ll a strong finish to your respective dissertations. Thank you to my team of undergraduate research fellows, John Correy, Hans Martin, Kaito Durkee,

Andrew Kullman, and Simon Fraser, for your continued hard efforts. Even as a multi-disciplinary team, each one of you wanted to learn as much as possible to contribute to the research projects is greatly appreciated. I couldn't have hit nearly as many benchmarks without your assistance. I hope the research experience was as memorable for you as it was for me. You guys are very talented, and I look forward to seeing your future endeavors. John Correy, wishing you all the best as you take the quad-beam experiment to new levels.

Fifth, on a personal level, I would like to thank my family, close friends, and mentors across the country. Your support throughout this process has meant the world to me. It took a tribe to do it and we did it. Thank you! Mom, Dad, Sister, thanks for the continued unwavering support throughout this eight-year journey. Lastly, thank you to my partner, Jessica, for continued encouragement, support, and patience. You're up next in completing your doctoral journey.

As my advisor would say, "we need more power", hence ≥1 MW worth of thank you to everyone. ~ "Ad Astra Et Ultra"

Chapter 1. Introduction

Electric propulsion (EP) involves the conversion of electrical energy into kinetic energy for the purposes of accelerating a spacecraft. One of the advantages of using electric propulsion systems instead of conventional chemical propulsion systems is that an electrically-augmented energy source can accelerate ejected particles to much higher exit velocities than a solid or liquid chemical propellant source. These higher exit velocities correspond to an improvement in the propulsion system's specific impulse (Isp), which is a measure of thrust produced per unit of propellant weight flow rate, i.e., a measure of propellant utilization efficiency, resembling miles per gallon for an automobile. The relationship between a propulsion system's specific impulse, thrust produced, propellant weight flow rate, and average exit velocity is shown in Equation 1.1.

$$Isp = \frac{F}{\dot{m}_p g_0} = \frac{v_e}{g_0} \tag{1.1}$$

Although state-of-the-art EP systems are incapable of producing high thrusts like their chemical counterpart, the reduced propellant flow rate and high specific impulse make them advantageous for many in-space applications. For instance, EP systems are more advantageous for orbit raising, station-keeping, deep space, and interplanetary missions. The rocket equation shown in Equation 1.2 relates the velocity increment ΔV of the spacecraft to the propellant ejection velocity (V_e). In the equation, m_o is the initial mass, which includes the propellant mass (m_p) and the final mass (m_f). The rocket equation shows that there are two options for increasing the velocity increment: (1) either burn a substantial amount of propellant, whereby $m_p \approx m_o$ or (2) use a propulsion system that has a high exit velocity (v_e) capability. Typically, mission planners and spacecraft operators seek to minimize propellant mass usage and hence prefer the high v_e

option which has three distinct benefits: (1) increased payload mass for scientific and spacecraft enabling operations, (2) lower spacecraft initial mass and launch costs, (3) increased spacecraft longevity by performing mission-specific maneuvers for a longer duration. The usage of a high Isp propulsion system enables a broad range of ΔV missions. Some typical ΔV for various space mission scenarios are listed in Table 1.1. Because of the ΔV being defined for specific maneuvers and space missions, the rocket equation is rewritten in terms of the propellant mass in Equation 1.3. The ratio of the propellant mass to the initial mass (m_p/m_o) as a function of exit velocity for two velocity increments is shown in Figure 1.1. As can be seen in the figure, the chemical propulsion system has a large propellant consumable fraction for velocity increments and is only affordable within a specific region [Ref. 1]. With a high v_e EP propulsion system, the propellant consumable fraction drops off significantly allowing for significant increase in payload fraction and mission duration. High exit velocity EP systems provide a realistic and flexible architecture to pursue large ΔV missions that are not constrained by time limitations.

$$\Delta V = V_e \ln\left(\frac{m_o}{m_f}\right) = V_e \ln(1 + \frac{m_p}{m_f}) \tag{1.2}$$

$$m_p = m_o \left[1 - \exp\left(\frac{-\Delta V}{V_e}\right)\right] \tag{1.3}$$

Table 1.1: Typical ΔV for Various Space Mission Scenarios [Ref. 1]

Satellite displacement	Δv (m s^{-1} per year)
Drag compensation (500 km)	30
Attitude control	2–6
Station keeping in GEO	50
Orbit transfer	**Δv (km s^{-1})**
Earth—LEO	9,7
LEO—GEO	4,3
LEO—Moon	5,9
LEO—L1	3,7
LEO—L2	3,4
LEO—Mars	4,3
Interplanetary journeys	**Δv (km s^{-1})**
Nearby planets	5–8
Far-off planets	10–15
100–1000 au	100
10 000 au	1000
Interstellar medium	30 000

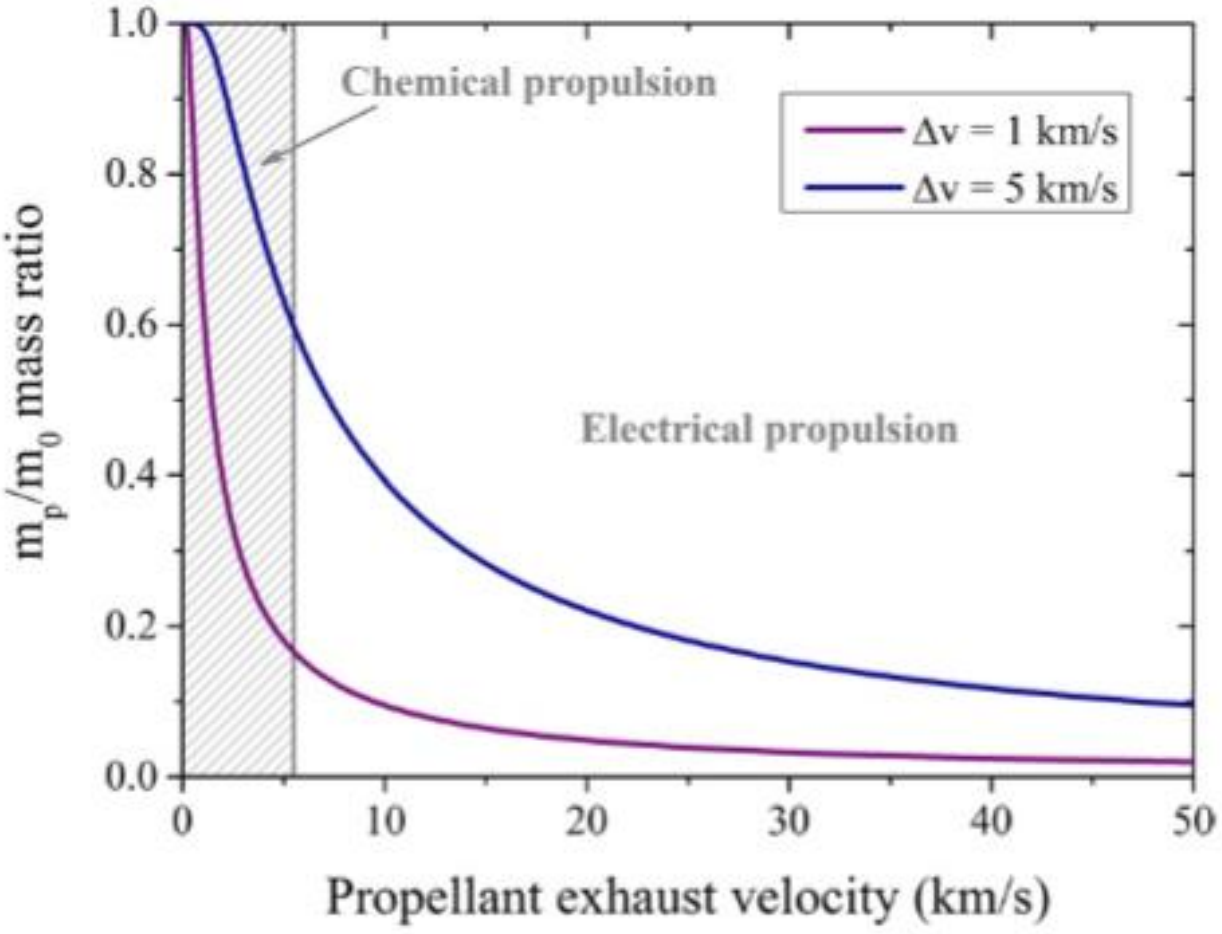

Figure 1.1: The evolution of the ratio of propellant mass to initial mass (m_p/m_o) for two velocity increments. Chemical propulsion technologies are only viable within the shaded region of the figure, while EP systems can pursue large ΔV missions with a significant reduction in the propellant mass fraction [Ref. 1].

1.1 Electric Propulsion Overview

Although electric propulsion devices use electrical energy to accelerate a propellant to higher exit velocities than their chemical counterparts, the mechanism for plasma production and acceleration can be sub-divided into three distinct categories: (1) electrothermal propulsion, (2) electrostatic propulsion, and (3) electromagnetic propulsion.

Electrothermal propulsion systems are most like conventional chemical propulsion devices, as the working fluid interacts with a nozzle to allow for isentropic expansion of the heated fluid. Electrothermal propulsion uses the electrical energy to heat propellants thermally by resistive heaters in different geometric configurations, as is the case for resistojets, or by passing the propellants through an electrical arc discharge between a cathode and anode, as is the case for arcjets. Resistojets and arcjets are flight-proven EP systems, commonly operated at power levels ranging from several hundred watts up to one kilowatt, specific impulse from 100 – 300 s for resistojets and up to 500 s for arcjets. These electrothermal devices are compatible with a wide range of propellants, i.e. nitrogen, xenon, ammonia, hydrogen and hydrazine; however, these thrusters typically use hydrazine due to ease of integration into standardized propellant management assembly commonly used on chemical rocket engines. These electrothermal thrusters are considered low-thrust devices with thrust ranging from 100 – 200 mN [Ref. 1], applicable for position adjustment and station-keeping applications. An example of an electrothermal hydrazine resistojet thruster used for communication satellite station-keeping is shown in Figure 1.2. An example of an electrothermal hydrazine arcjet thruster used for communication satellites is shown in Figure 1.3.

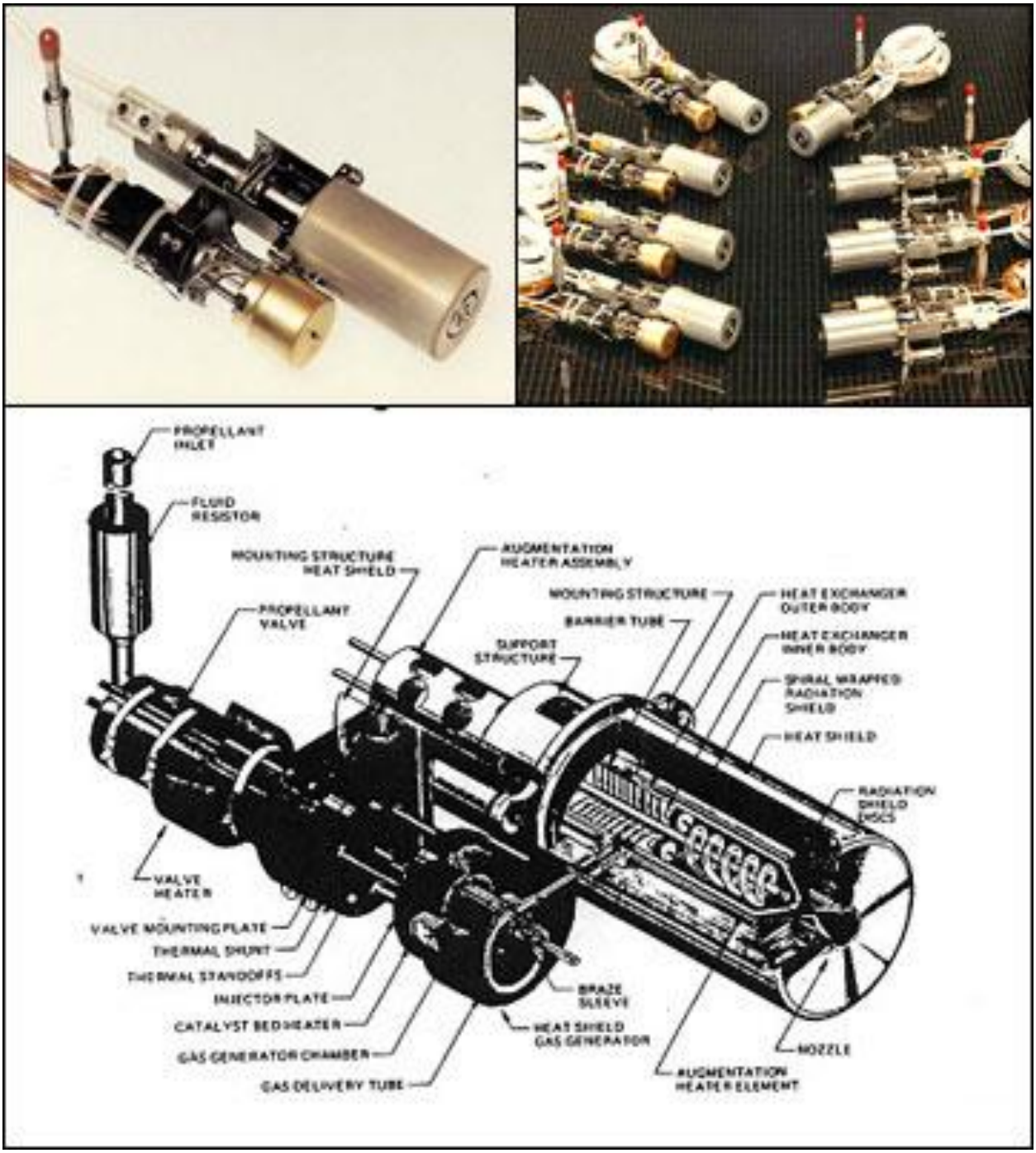

Figure 1.2: Picture and schematic of the 500 W Aerojet MR-501B electrothermal hydrazine thruster (EHT) resistojet used for communication satellite station-keeping. The MR-501B generates up to 360 mN of thrust and specific impulses of 303 s [Ref. 2].

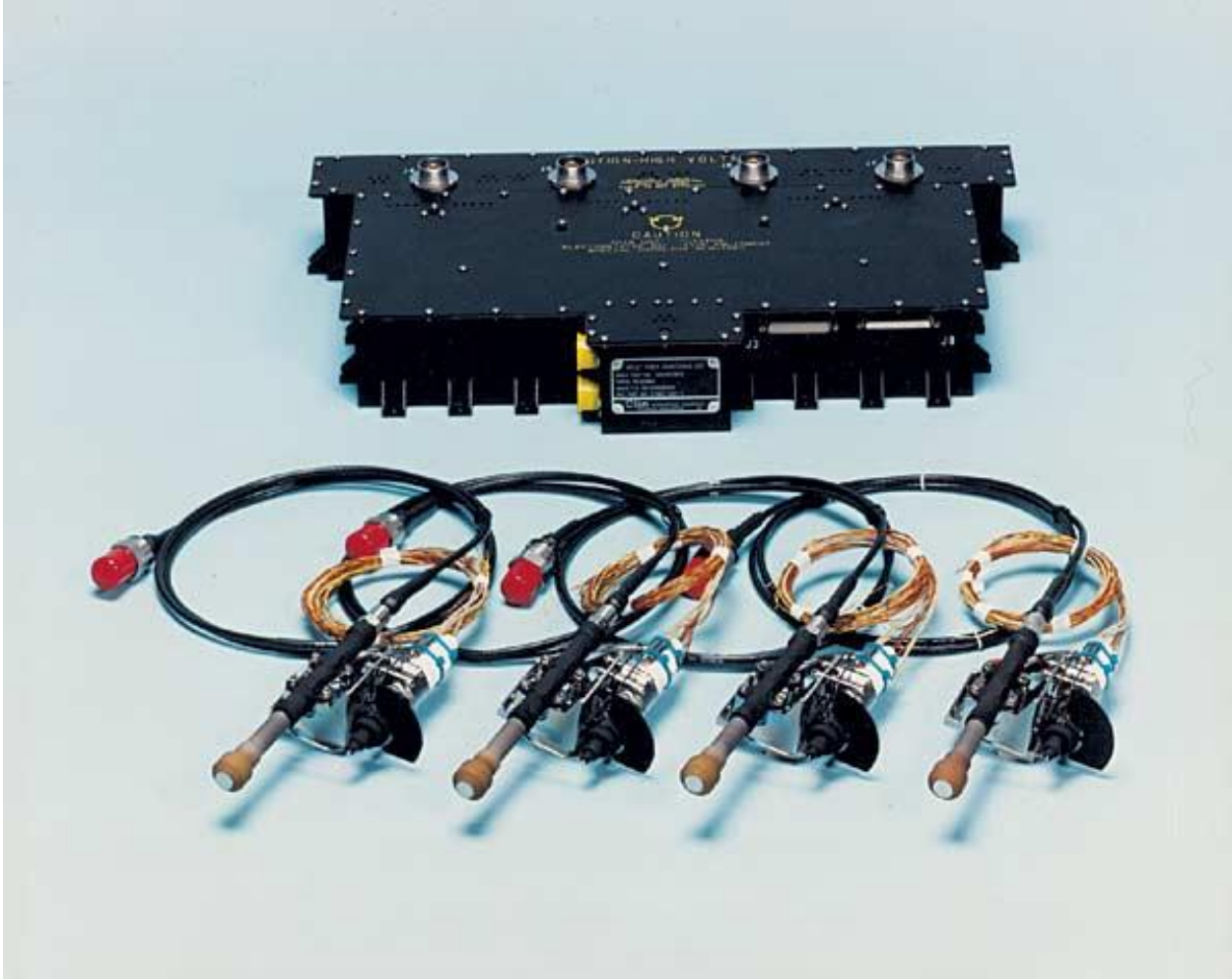

Figure 1.3: Aerojet MR-510 arcjets for repositioning of communication satellites in North-South Station Keeping (NSSK) [Ref. 3].

Electrostatic propulsion systems use electrical energy to first ionize the propellant and then use a set of biased grids to create an electric field to accelerate the ions to high exit velocities, exerting an electrostatic force on charged particles to generate thrust. The working principles of the electrostatic ion gridded thrusters can be seen in Figure 1.4. For the ion gridded thrusters, the amount of extracted ion current through the gridded apertures is limited by the repulsion of similarly charged species. This space-charge saturation limit is known as the Child-Langmuir Law

and defines the maximum allowable ion current that can pass through a gridded aperture of an ion thruster. For most ion thrusters, they consist of three main regions: (1) the discharge chamber, (2) the gridded assembly, (3) and the neutralizer cathode. The first region acts to efficiently ionize the propellant in the source chamber. The second region uses a two-grid (electrode) system to electrically focus ions downstream of the ion engine. The first grid is biased at high positive electrical potential to screen electrons while the second grid is biased at negative electrical potential to accelerate the ions through the gridded aperture. The third region uses an external cathode source – the neutralizer to mix electrons with the ion beam such that the downstream thruster plume is quasi-neutral, minimizing the effect of partial space-charge buildup that could drastically decrease thruster performance. NASA's Evolutionary Xenon Thruster (NEXT) is a next generation ion thruster to supersede the performance characteristics of the NSTAR ion engine previously used on the Deep Space 1 and Dawn spacecraft missions. The NEXT ion thruster can operate at electrical powers up to 6.9 kW with specific impulse and thrust production of 4,190 s and 236 mN respectively. The NEXT propulsion device has operated well over 43,000 hours in a space-simulation facility at NASA Glenn Research Center, as depicted in Figure 1.5.

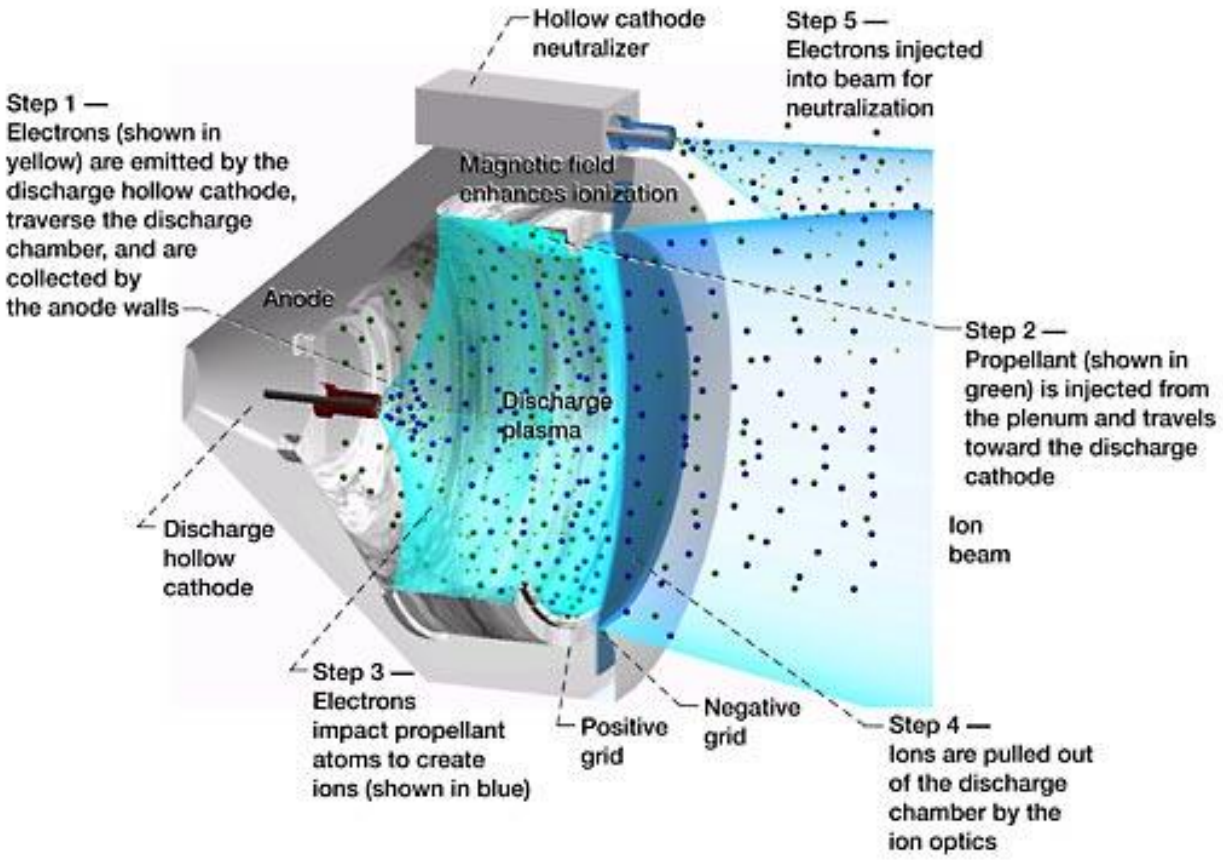

Figure 1.4: Schematic Diagram – Working Principles of an Ion Gridded Thruster. Credit: NASA

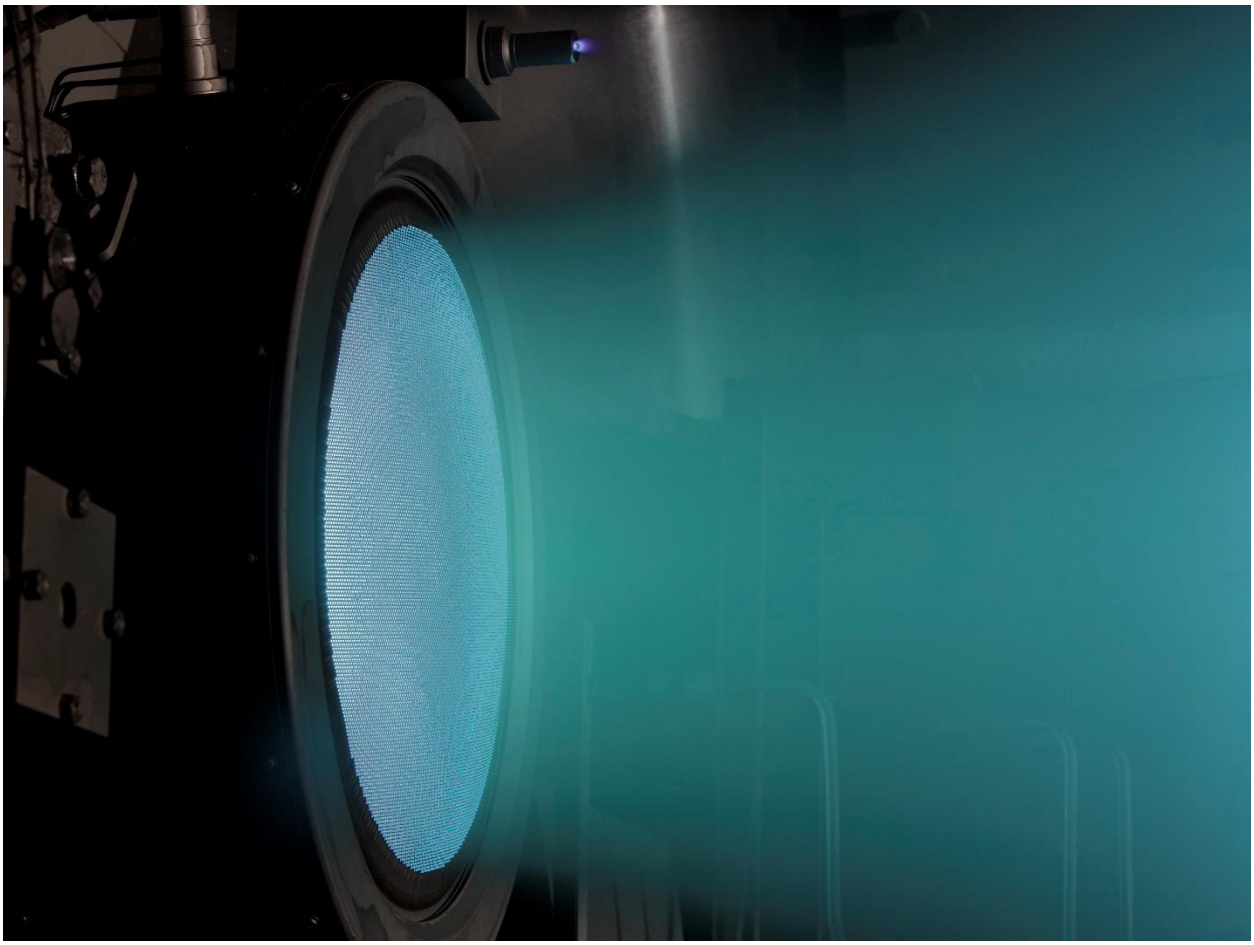

Figure 1.5: NASA's Evolutionary Xenon Thruster (NEXT) Ion Gridded Thruster Under Operating Conditions at NASA Glenn Research Center. Credit: NASA

Electromagnetic propulsion systems ionize propellant and accelerate ions to high exit velocities via the combined action of electric and magnetic fields, which assert a Lorentz force on charged particles to generate thrust. Three common types of electromagnetic thrusters are the (1) Magnetoplasmadynamic (MPD) thruster, (2) pulsed plasma thruster (PPT), and (3) Hall-effect thrusters. MPD thrusters are simple, robust, and compact architectures using a magnetic Lorentz force, resulting from a radial current density interacting with a self-induced magnetic field, to accelerate the plasma to high exit velocities in the axial direction. An MPD thruster has

performance characteristics with thrust at 0.5 – 50 N, specific impulse at 1,000 – 10,000 s, thrust efficiency at 40% when operating hydrogen, helium, or argon propellants. MPD thrusters must operate at sufficiently high discharge current ~ several kA to obtain the self-induced magnetic field necessary to drive its performance. As a result, MPD thrusters are considered optimum choices for megawatt-class missions, although the high discharge current limits the engine lifetime due to cathode deterioration. The PPT device provides a high-current short pulse mode ~ 10 μs discharge that ablates and ionizes a small amount of solid propellant, i.e. Teflon [Ref. 4] or Sulfur [Ref. 5]. The high instantaneous current induces a magnetic field that imparts a magnetic Lorentz force responsible for high exit velocities. Since PPTs are pulsed devices, key performance characteristics are impulse bit at 0.1 mN s and specific impulse at 500 – 1500 s. PPTs are suitable for attitude control, station-keeping, and primary propulsion of power-limited nanosatellites.

The Hall-effect thruster (HET), in a stationary plasma thruster (SPT) configuration, is considered an electrostatic – electromagnetic propulsion that encompasses five main components: (1) anode – positive electrode, (2) cathode – negative electrode, (3) gas distributor, (4) the magnetic circuit, (5) ceramic discharge channel. Neutral gas, typically xenon or krypton propellant, is injected into the back of the ceramic channel via a gas distributor. A strong axial electric field is created due to the potential difference between the anode and cathode. A small portion of the neutral gas is fed through the hollow cathode, emitting high-energy electrons that exhibit an azimuthal **E**x**B** drift colliding with the neutrals in the rear of the discharge channel to generate ions. The magnetic circuit provides a sufficient magnetic field strength to confine electrons within the discharge channel, with an electron Larmor radius less than the discharge channel dimensions, to continue ionizing propellant while the axial electric field imparts an electrostatic force on the ions to generate thrust. Hall thrusters have demonstrated thruster efficiency between 50 – 60%,

with specific impulse up to 3000 s, and thrust up to 5.4 N for power levels approaching 100 kW [Refs. 6-7]. Figure 1.6 demonstrates the working principles of HETs while Figure 1.7 showcases key thruster development at different power regimes.

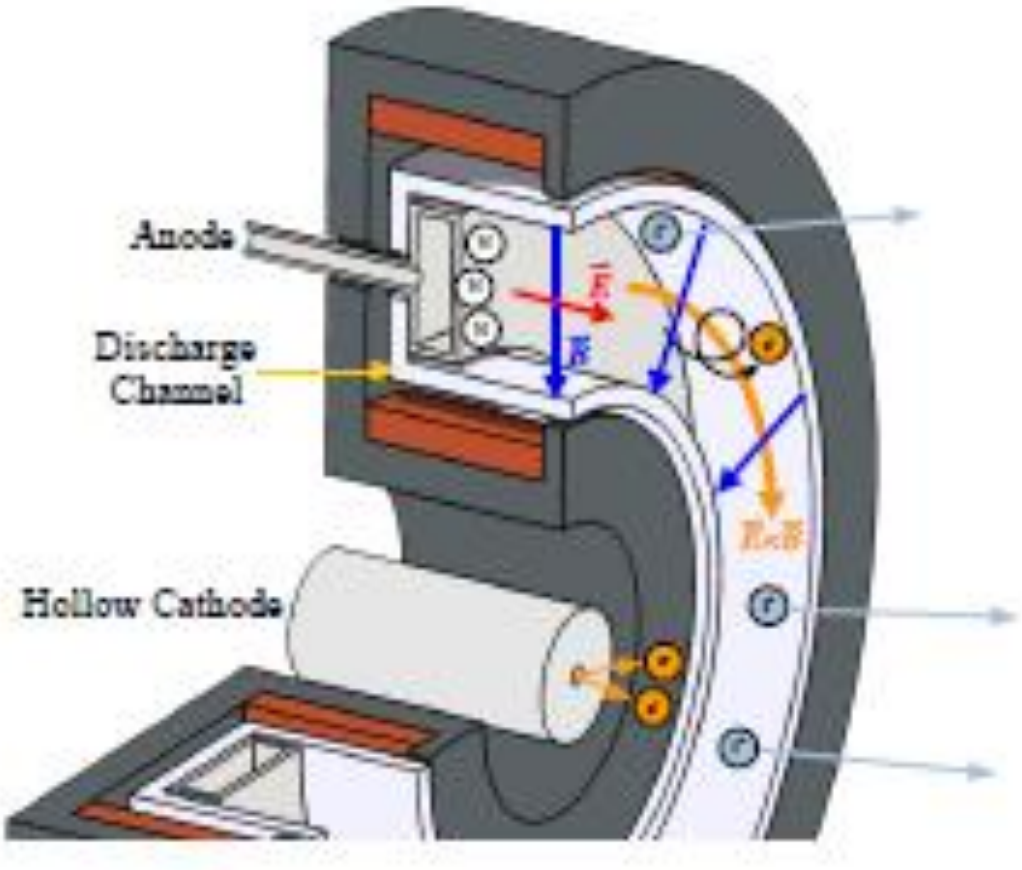

Figure 1.6: A schematic diagram of a single channel Hall-effect thruster [Ref. 8].

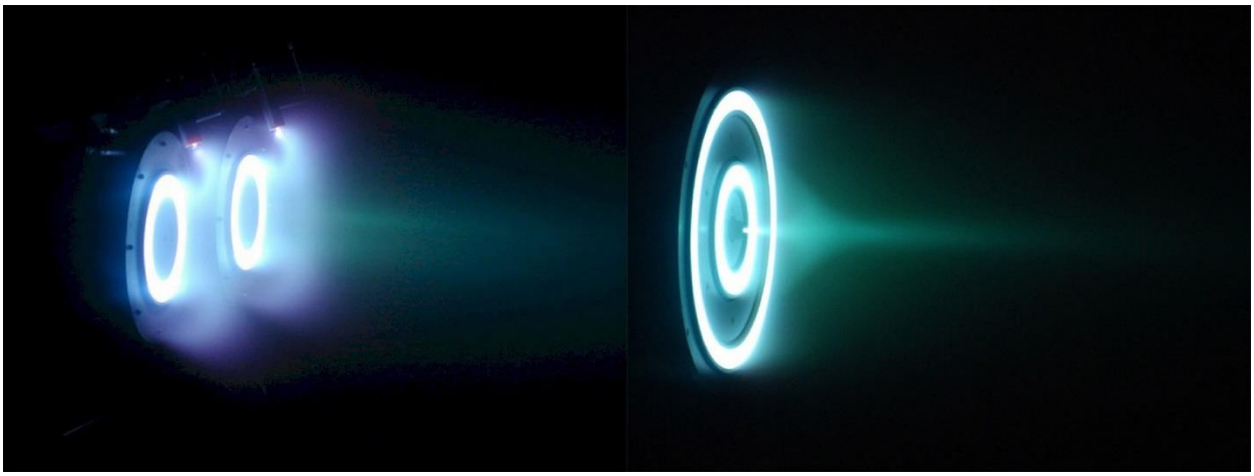

Figure 1.7: Hall thruster development at University of Michigan's PEPL. (Left) 5 kW x P5 Cluster Hall Thruster [Ref. 9]. (Right) 100 kW X3 Nested Channel Hall Thruster [Refs. 6-7].

1.2 Advanced Electric Propulsion: Helicon Thruster Overview

Helicon plasma discharges have been intensively studied in the last three decades as high-density plasma sources up to 10^{19} m^{-3} or higher. With an order of magnitude higher in density than similar power-level inductive systems, helicons have become a leading candidate for a variety of applications, i.e., semiconductor processing, plasma injection into toroidal devices, and electric propulsion systems [Refs. 10-12]. As concerns within the electric propulsion community have grown over grid and electrode erosion, helicon plasma thrusters have emerged as an electrodeless electric thruster concept, offering redundancy, flexibility, extended engine lifetime, lower complexity, and reduced costs when compared to other electric propulsion technologies. A helicon thruster consists of four physical parts: a gas injection line, a dielectric source tube for plasma generation, a helical radiofrequency (RF) antenna and an external applied magnetic field [Ref. 13]. A schematic diagram of a helicon plasma thruster is shown in Figure 1.8.

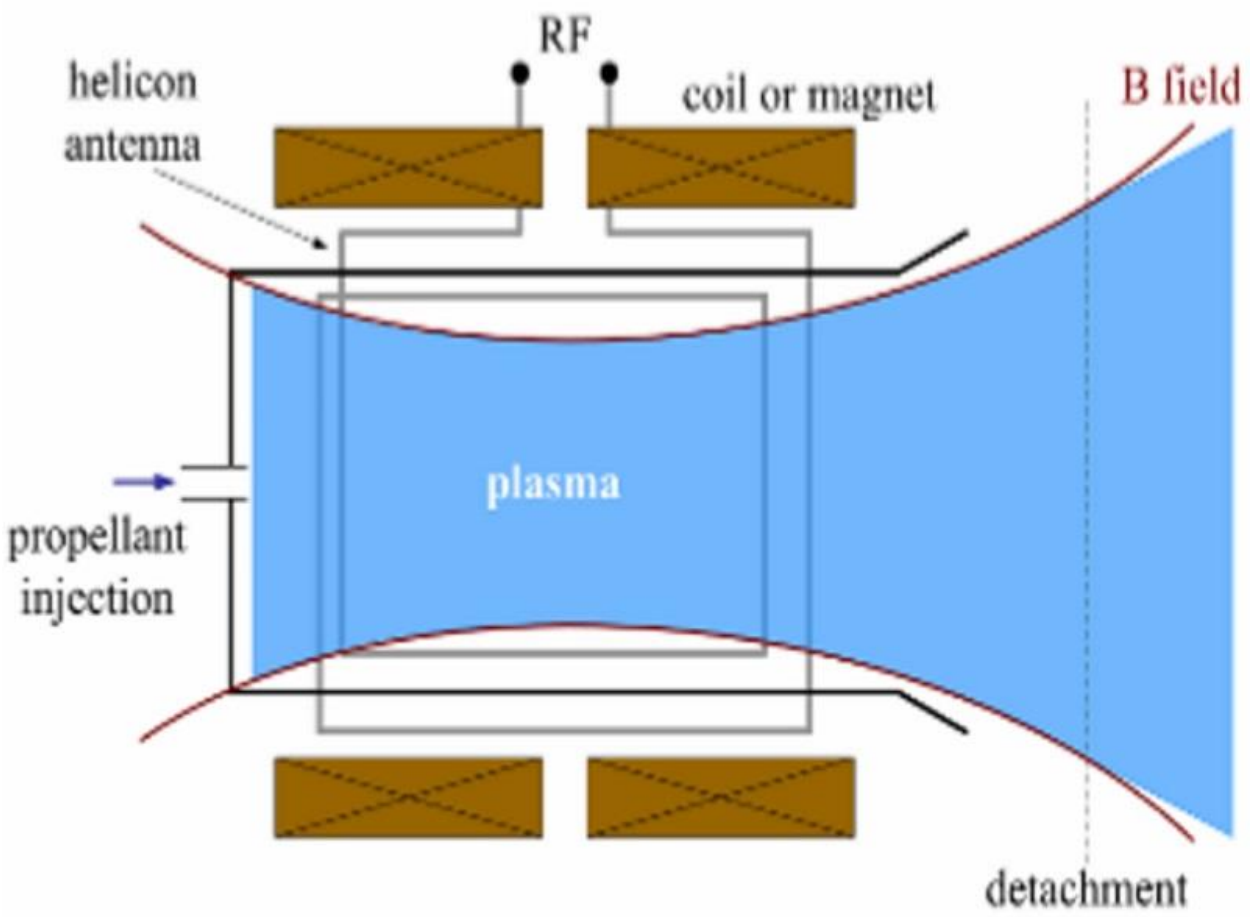

Figure 1.8: Schematic diagram of a helicon plasma thruster [Ref. 1]

Across the globe, there are numerous experimental research programs investigating helicon thrusters as a spacecraft propulsion concept. In Australia, the 2 kW Helicon Double Layer Thruster (HDLT) accelerates ions to supersonic velocities via a current-free double layer, a potential drop that forms at the boundary between high density plasma in the source region and low-density plasma in the exhaust region [Ref. 14]. In Europe, a consortium of fifteen institutions representing seven European countries designed and developed a low power, 50 W, helicon thruster (HPH.com) for small satellite operation [Ref. 15]. In the United States, the mini-helicon thruster was tested at RF powers ~ 1 kW, using a variety of propellants, i.e. argon and nitrogen to understand the governing physics behind helicon systems [Ref. 16]. For high-power helicon thruster operation

(≥100 kW), the Variable Specific Impulse Magnetoplasma Rocket (VASIMR) has successfully demonstrated good thruster performance at powers up to 200 kW, 72% thruster efficiency, and specific impulse of 5,000 s. VASIMR uses a helicon source for ionization, ion cyclotron resonance for additional heating, and a superconducting magnetic nozzle for plasma acceleration. The VX-200SS aims to demonstrate 100 kW steady-state operation for 100 hours [Ref. 17]. The operation of helicon thrusters in space-simulation facilities for a range of power levels can be seen in Figure 1.9. Most of the development work in helicon thruster technology has been explored in a low power regime ≤ 2.5 kW, except for Ad Astra Rocket company's VX-200 device. In addition to the previously discussed helicon thruster development, researchers at the University of Washington have sought to investigate the high-power, high density regime of helicon sources for space applications, which will be discussed in greater detail in the next section.

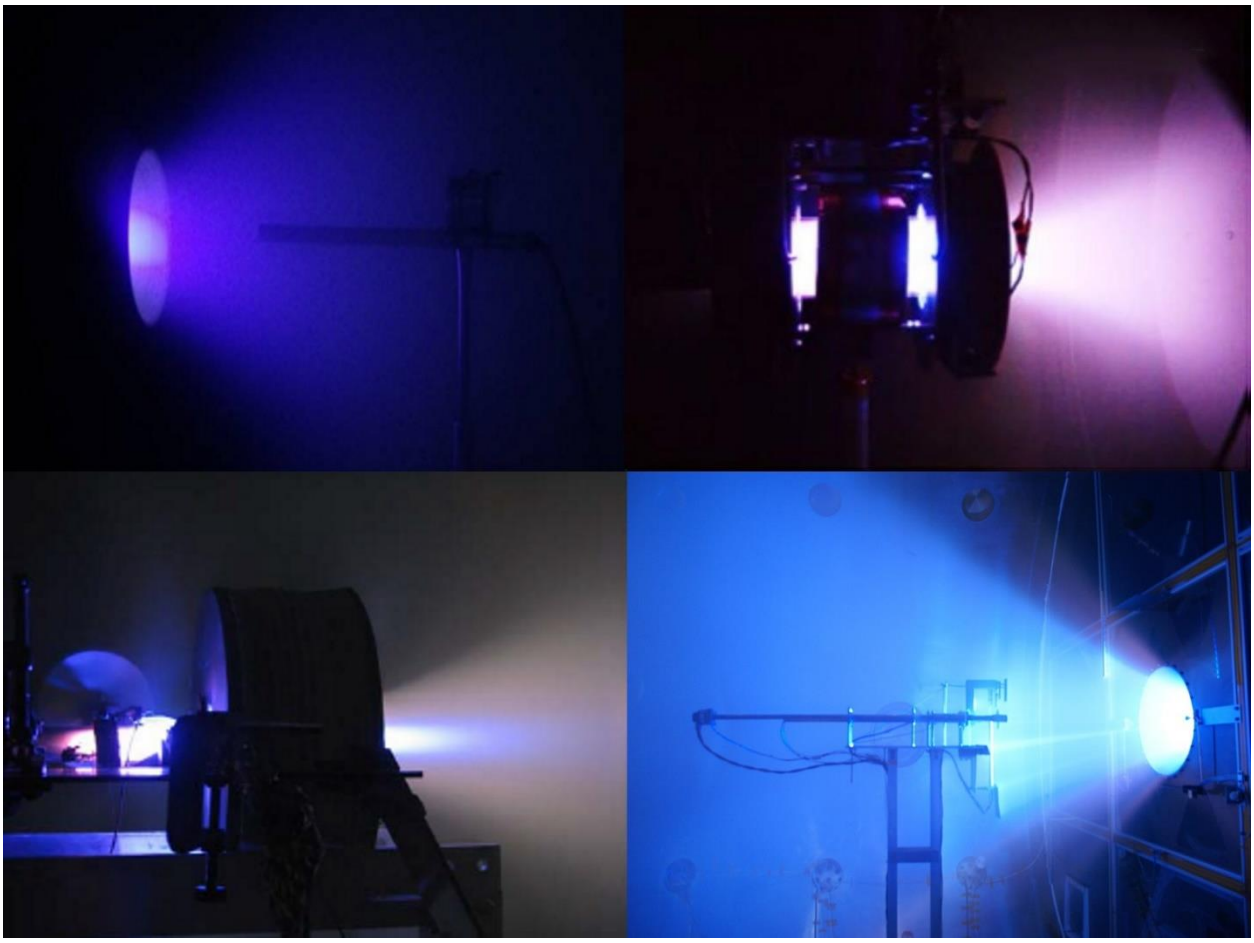

Figure 1.9: Helicon thruster development in the past two decades for various power regimes using Argon propellant. (Top Left) 50-W helicon thruster for nanosatellite applications [Ref. 15]. (Top Right) 1 – 2.5 kW Helicon Double Layer Thruster (HDLT) [Ref. 14]. (Bottom Left) 1 kW mini-Helicon plasma thruster [Ref. 16]. (Bottom Right) VX-200 VASIMR rocket engine at 200 kWe for high power missions [Ref. 17].

1.3 Historical Perspective: High-Power Helicons at the University of Washington

The University of Washington's High-Power Helicon (HPH) thruster experiment has explored the high-power regime since the early 2000's, with an aim of understanding the helicon physics and developing advanced architectures for deep space exploration. The HPH thruster is

designed to produce dense plasma (>90% ionization fraction) operating at lower RF frequencies (≤1 MHz) that is accelerated downstream at supersonic velocities (>10 km/s) without the need for electrodes [Refs. 18-19]. HPH accomplishes this by driving a wave magnetic field with an amplitude a significant fraction of the base magnetic field. The electromagnetic wave energizes electrons to ionize neutral gas, creating a positive space charge density as electrons leave the source region, and accelerates ions via a large ambipolar electric field to maintain a quasi-neutral plasma in the exhaust region. In 2005, Ziemba et al. tested the first HPH prototype using a time-of-flight probe to measure the plasma acceleration downstream of the source [Ref. 20]. In 2007, Winglee et al. performed numerical and experimental work, using magnetic nozzles to convert random thermal energy into axial kinetic energy, improving ion collimation downstream of the source and producing a net thrust [Ref. 21]. In 2008, Prager et al. confirmed that ion energies were propagating downstream of the source region because of the helicon wave, with a diamagnetic effect reported leading to enhanced exit velocities [Ref. 22]. In 2011, Roberson et al. used an optimum magnetic topology combined with a larger downstream RF antenna to drive additional helicon wave energy further from the source, improving electrical coupling efficiency and leading to higher exit velocities [Ref. 23]. In 2014, Murakami et al. tested the HPH double gun thruster to extend the power regime of a single helicon, and to investigate whether additional efficiency can be achieved due to coherent addition of two helicon waves [Ref. 24]. The operation of HPH variants in space-like conditions at the University of Washington can be depicted in Figure 1.10.

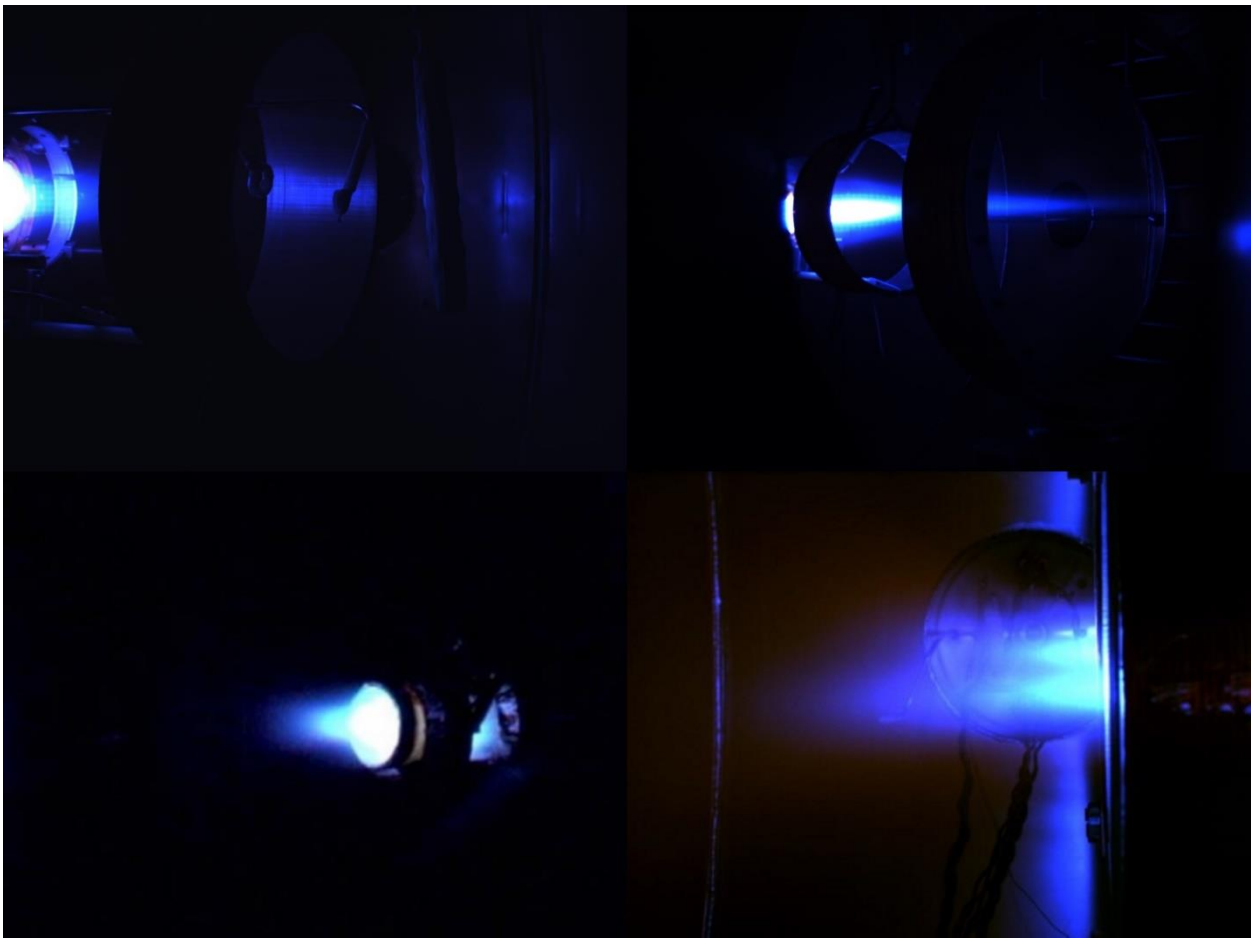

Figure 1.10: HPH thruster development in a 4800-L space simulation facility at the University of Washington using Argon propellant. (Bottom Left) single HPH thruster at 160 G base magnetic field, circa 2005. (Top Left) single HPH thruster at 400 G base magnetic field with activation of a downstream magnetic nozzle, circa 2009. (Top Right) single HPH thruster at 400 G base magnetic field with activation of two downstream magnetic nozzles, circa 2009. (Bottom Right) double HPH thruster at 160 G base magnetic field, in a parallel configuration, circa 2014.

1.4 Clustered Helicon Thrusters for High-Power Missions

It has been identified by NASA and international collaborators across the globe that high specific impulse, high-power solar electric propulsion (SEP) will be an affordable and sustainable

architecture for our exploration pursuits beyond low-Earth orbit (LEO) toward the Moon, Mars and beyond [Refs. 25-27]. NASA's vision for human exploration beyond LEO is illustrated in Figure 1.11. In the past, the implementation of high-power SEP has been limited due to two key factors: (1) available space solar power and (2) technology maturation of high-power electric propulsion devices. For the first key factor, space solar power advancements are cataloged in chronological order onboard spacecraft, as seen in Figure 1.12. Space solar power has evolved from just one watt (W) of power available on the Vanguard spacecraft in 1959 toward 260 kilowatts (kW) on the International Space Station (ISS) [Ref. 28]. The power onboard spacecraft has effectively doubled every four years for over five decades, allowing for spacecraft designers to consider using high-power electric engines for more ambitious in-space exploration missions. Addition enhancements have been made with the development of MegaFlex solar array wings, which exhibit excellent stowing capability with high strength to weight ratio and high specific power (W/kg) [Ref. 29]. For the second key factor, there has been a resurgence in high-power electric thruster development in the United States due to NASA's NextSTEP program, a public-private 50:50 partnership between NASA and companies Aerojet Rocketdyne and Ad Astra Rocket Company, to demonstrate 100-kW operation for 100 hours of their EP variants. Aerojet Rocketdyne is developing the X3 nested-channel Hall thruster, with an integrated Xenon propellant management assembly (PMA) for flow control and the power processing unit (PPU) for delivering electrical powers between 100 – 200 kW. The X3 will be tested at NASA Glenn's VF5 and University of Michigan's PEPL space-simulation facilities [Refs. 30-31]. Ad Astra Rocket company, on the other hand, has tested its advanced helicon thruster, VASIMR VX-200SS device using Argon propellant at its Houston headquarters $150\,m^3$ vacuum testing facility. The VX-200SS device has demonstrated 62% thruster efficiency with an Isp of 4500 s during its 100-hour

steady state operation [Ref. 32]. With recent technology maturation in solar array technology and high-power electric propulsion, large-scale science missions and in-space cargo transportation to the Moon, asteroids, and Mars may be on the horizon.

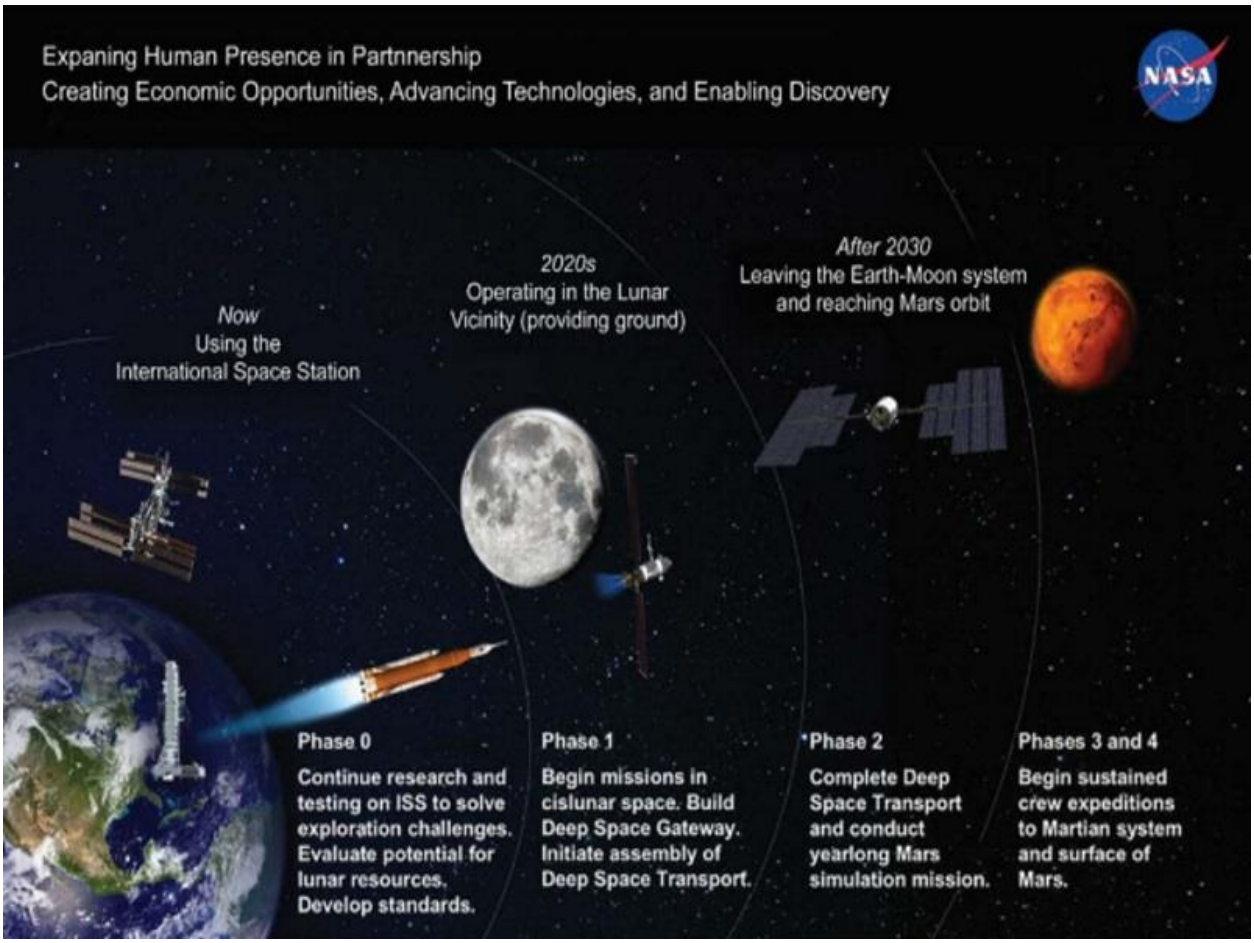

Figure 1.11: NASA's Human Exploration Vision, including the Lunar Orbital Platform – Gateway (aka Deep Space Gateway) and the Deep Space Transfer Vehicle [Ref. 33].

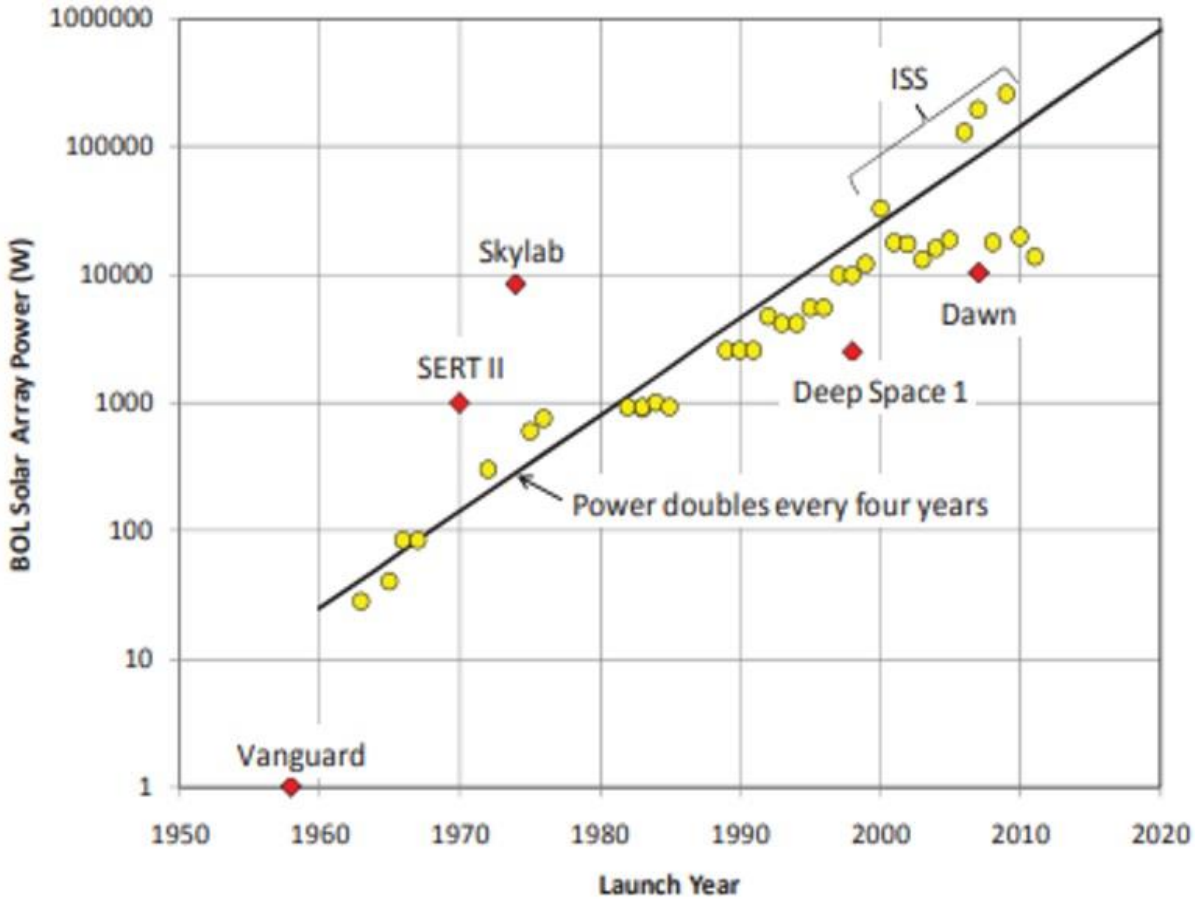

Figure 1.12: Space solar power advancements over the many years on satellites and spacecraft [Ref. 28].

As high-power electric propulsion devices continue to be matured, a key question needs to be asked: Should only monolithic devices be developed beyond high-power regimes ≥100-kW or should clustered devices also be developed? Table 1.2 provides the relative merits of either monolithic or clustered devices for high-power missions [Ref. 34]. Clustering of electric thrusters has several advantages over a single unit which include: (1) increased reliability due to inherent redundancy of operating multiple thruster devices, (2) throttling of EP engines by selectively using certain engines to modulate power and propulsion for mission-specific purposes, and (3) high-degree of scalability to explore ambitious deep space endeavors. There have been several clustered

thruster studies that measured the downstream plume properties of relatively low-power Hall-effect thrusters at 200 W [Ref. 35], 600 W [Ref. 36], and 5 kW [Ref. 9]. As a relatively new example, a cluster of four, 12.5 kW Hall Effect Rocket with Magnetic Shielding (HERMeS) thrusters is planned for integration into the Power and Propulsion Element (PPE) to provide a total of 50 kW for station-keeping and orbital maneuvering of the Deep Space Gateway in a lunar orbit, expected by 2022 [Ref. 33].

From the authors perspective, key questions of inquiry include: (1) How will the cluster of HERMeS thrusters perform, when operating collectively? (2) Will the combined plasma plume interact with the orbiting platform? As the power levels for each thruster unit are scaled up in the future, these questions will become increasingly important. To the authors knowledge, there is not any literature on numerical modeling and/or experimental work of a cluster of high-power electric propulsion devices and potential interactions with spacecraft. A study by Squire et al. determined that the advanced helicon thruster, VASIMR VX-200 has advantages in system performance and mass in comparison to Hall effect thrusters as you increase the power and total number of thruster units [Ref. 37].

By investigating the clustering effects on downstream plume properties, this research aims to provide insights for current and future advanced high-power helicon architectures. For the clustered HPH research, an optimum clustered configuration may yield additional improvements to the electrical coupling efficiency and specific impulse outlined in Table 1.2 while maintaining system reliability, scalability, and flexibility. A clustered high-power helicon architecture with a compact form factor and high specific impulse capability could be mission enabling, allowing expanded in-space commercialization and exploration endeavors. High-power mission scenarios enabled by the clustered HPH system are discussed in Appendix A and Appendix B sections.

Table 1.2: Merits of Monolithic (200 kW) and Clustered (2 x 100 kW) High-Power EP Devices. Adapted from [Ref. 34].

Criteria	Monolithic	Cluster
Performance		
Efficiency	Approximately the Same	Approximately the Same
Specific Impulse	Approximately the Same	Approximately the Same
System Dry Mass	Lower	Higher
Reliability		
Individual Thruster	Same	Same
Overall System	Lower	Higher (Redundancy)
Operational Flexibility		
Throttling Range	Lower	Higher
Suitability for Orbit Raising	Same	Same
Suitability for Station-keeping	Lower (Off-design State)	Higher
Development Flexibility	Lower	Higher
Development Cost	Higher	Lower
Suitable Test Facilities	Few	Few

1.5 Contribution of Research

In this research, the author seeks to address technical challenges from an experimental perspective involved with operating a cluster of ≥100 kW HPH thrusters such as: (1) What is the effect of plasma properties and beam divergence downstream from the source? (2) Is there possible electrical cross-talk between adjacent thruster units that affects overall thruster efficiency? (3) Is the lifetime of any individual thruster unit affected by its placement within the clustered configuration? (4) Within a compact thruster form factor, is there an optimum clustered configuration to yield an increase in beam collimation and specific impulse?

Chapter 2. Background

This section provides a general overview of wave propagation in helicon plasma sources. It also discusses the plasma phased array as a novel arrangement scheme to improve overall thruster efficiency for the HPH cluster experiment.

2.1 Helicon Wave Physics

Helicon wave sources are low-frequency electromagnetic waves bounded in a cylindrical column under the presence of a magneto-static field. Specifically, helicon waves are bounded whistler waves, which are one of several electromagnetic waves that travel parallel to the base magnetic field. Figure 2.1 shows the dispersion relationship for parallel electromagnetic waves [Ref. 38]. In the illustration, the whistler region of the right-hand circularly polarized (R) wave occurs at low frequencies bounded between the ion cyclotron frequency and the electron cyclotron frequency.

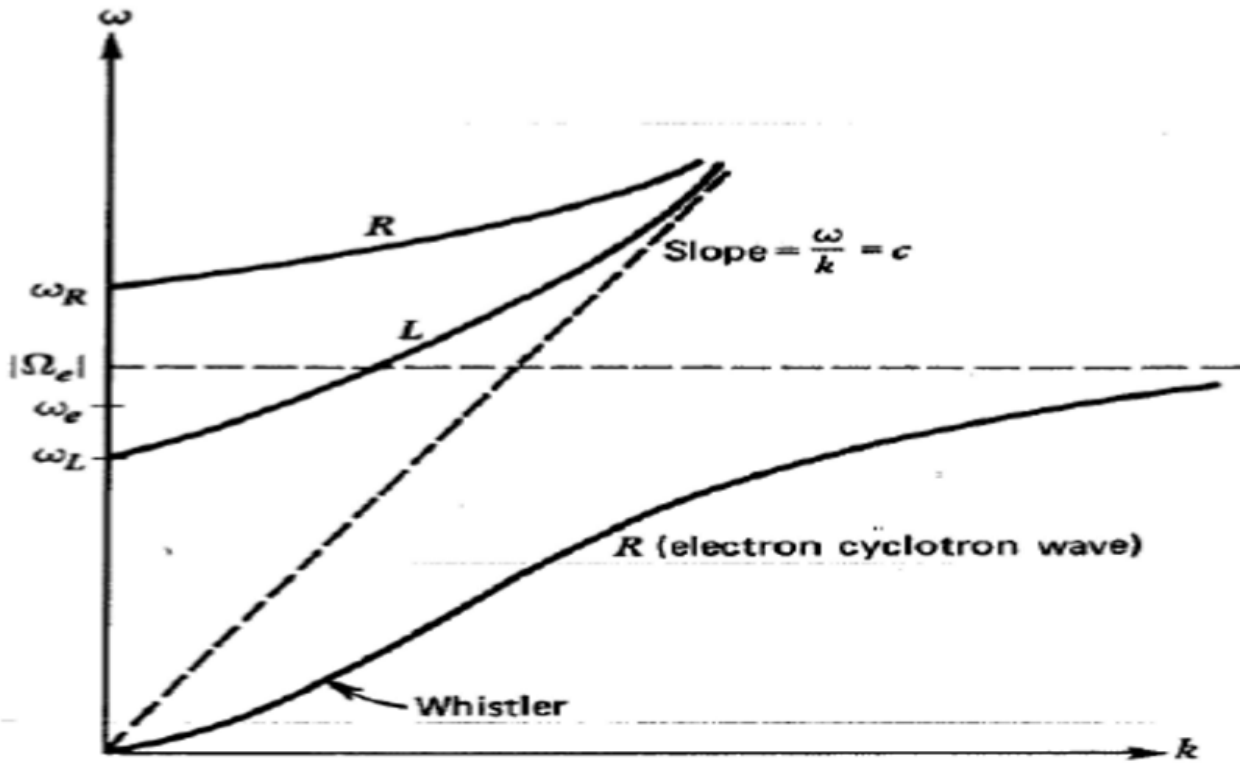

Figure 2.1: Dispersion Relation for Parallel Electromagnetic Waves [Ref. 38]

As such, helicon waves have gyration frequencies between the ion cyclotron frequency and the electron cyclotron frequency, which can be expressed in the following form

$$w_{c,i} \ll w_H \ll w_{c,e} \tag{2.1}$$

where $w_{c,i}$ is the ion cyclotron frequency, w_H is the helicon gyration frequency, and $w_{c,e}$ is the electron cyclotron frequency. Based on the relationship above, ions are too slow to respond to the helicon wave oscillations while electrons gyrate so quickly that they can be neglected. Henceforth, ion motion is neglected while electron motion is restricted to the guiding center motion and the plasma current is carried by the $\boldsymbol{E} \times \boldsymbol{B}$ drift [Ref. 39]. The dispersion relation for helicon sources can be derived using Maxwell's equations, excluding Gauss's Law since a helicon plasma source is quasi-neutral. The relevant Maxwell's equations are:

$$\nabla \cdot \boldsymbol{B} = 0 \tag{2.2}$$

$$\nabla x \boldsymbol{E} = -\frac{\partial \boldsymbol{B}}{\partial t} \tag{2.3}$$

$$\nabla x \boldsymbol{B} = \mu_0 \boldsymbol{j} + \mu_0 \varepsilon_0 \frac{\partial \boldsymbol{E}}{\partial t} \tag{2.4}$$

In equation 2.4, the displacement current term can be neglected since the phase velocity is much smaller than the speed of light. As such, the remaining equations can be linearized assuming the magnetic field (**B**) and electric field (**E**) consist of an equilibrium component (denoted by subscript 0) and a perturbation component (denoted by subscript 1). For reference, the magnetic field in terms of its equilibrium and perturbation components can be expressed as

$$B(\theta, z, t) = B_0 + B_1 e^{i(m\theta + k_z z - \omega t)} \tag{2.5}$$

where m is the azimuthal wave number corresponding to wave rotation, k_z is the wave vector in the axial z direction, and ω is the phase velocity. In addition to Maxwell's equations, the electron fluid momentum equation in the form

$$m_e n_e \left[\frac{\partial v_e}{\partial t} + (v_e \cdot \nabla) v_e\right] = n_e e(\boldsymbol{E} + v_e \, x \, \boldsymbol{B}) - (\nabla P_e) - \overline{\nu_{eo}} n_e m_e (v_e - v_0) \tag{2.6}$$

will be linearized assuming the pressure and magnetic resistivity terms are neglected. By linearizing these key equations and imposing cylindrical boundary conditions, the complete dispersion relation can be found, as done previously by Chen in several works [Refs. 39-40]. The derivation has also been completed for high-power, high density helicon sources in previous HPH experiments [Refs. 41-42] and other helicon plasma thruster research [Refs. 43-44]. The dispersion relation for $m = \pm 1$ mode of the helicon wave has the form

$$\frac{\omega}{k_z} = \frac{3.83}{a} \frac{B_0}{\mu_0 e n_0} \tag{2.7}$$

where B_0 is the base magnetic field, a is the radius of the cylindrical source, and n_0 is the plasma density. This dispersion relation implies that an increasing base magnetic field will lead to an increase in plasma density. The electrical (dotted lines) and magnetic field (solid lines) patterns for $m = \pm 1$ mode are shown in Figure 2.2. The left-handed circular polarized ($m = -1$) wave has a much narrower profile than the right-handed circular polarized ($m = +1$) wave, which may indicate weaker density profiles for the left-handed circular polarized wave. For a given source diameter and base magnetic field, the plasma density can be improved by selecting the appropriate antenna type. Dawson's experiment determined that the Nagoya Type III antenna (Figure 2.3) has the largest excitation of RF fields in the plasma core in comparison to other inductive antenna types [Ref. 45] due in part to the space-charge effect creating larger electrostatic fields [Ref. 46]. Figure 2.3 includes the directional flow of the current, electromagnetic field, and electrostatic fields produced within a Nagoya Type III antenna.

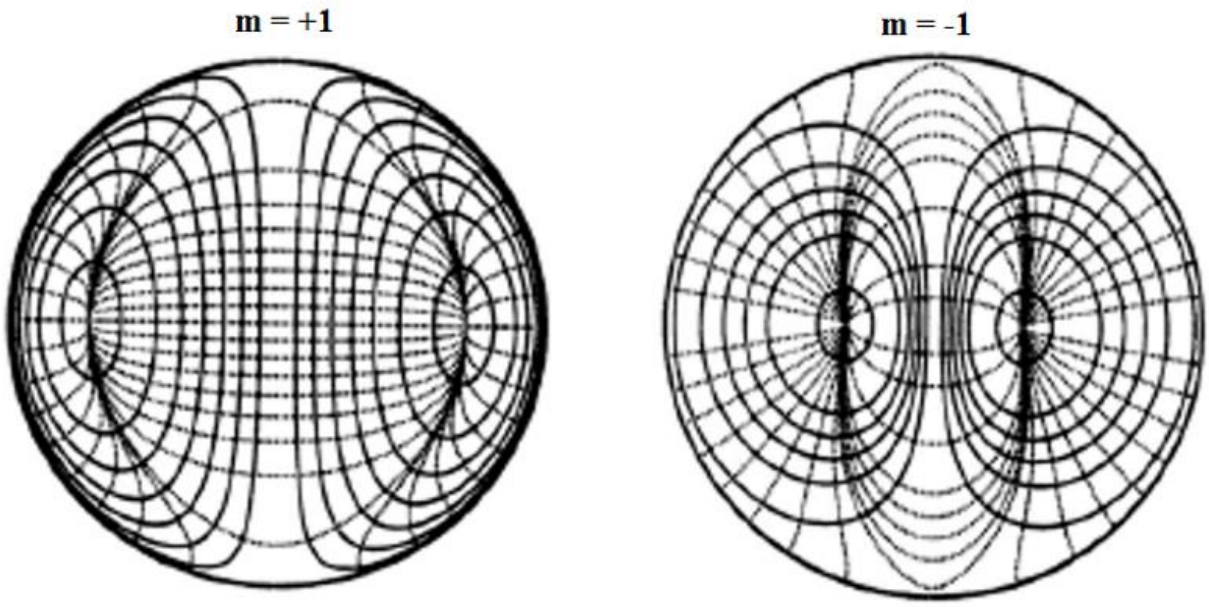

Figure 2.2: Electrostatic (dashed) and electromagnetic (solid) field patterns for $m = +1$, right-circular polarized wave (left) mode and for $m = -1$, left-circular polarized wave (right) mode [Ref. 40].

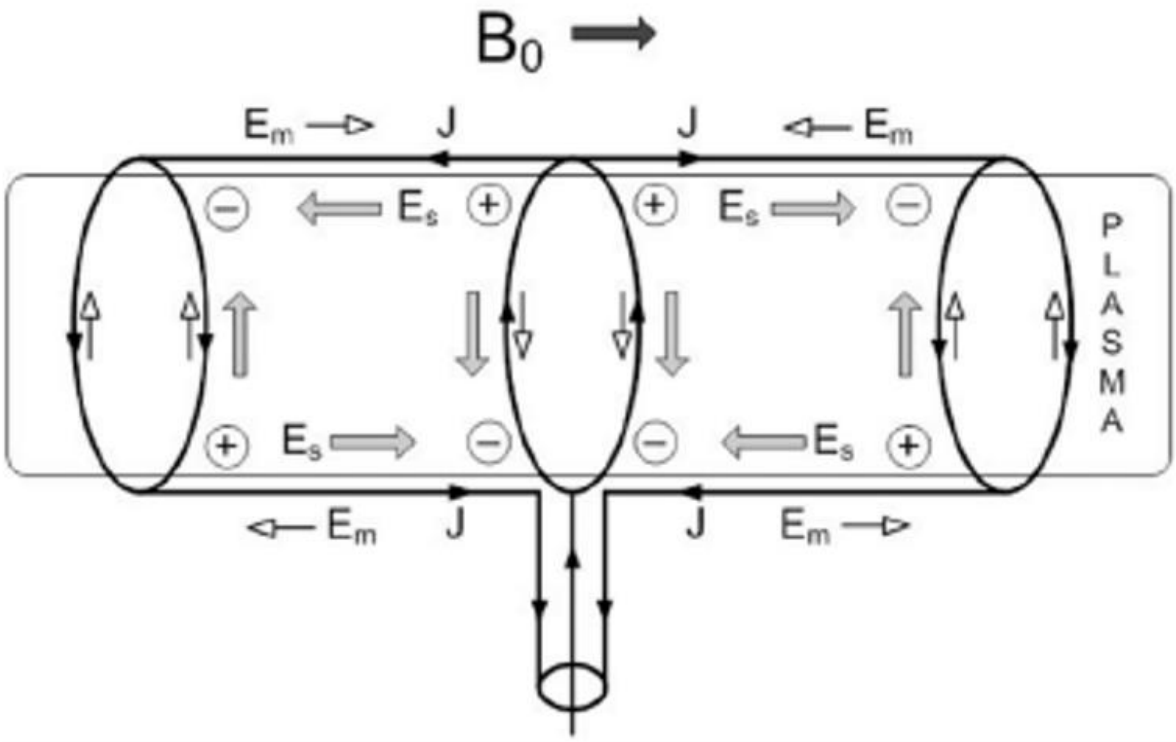

Figure 2.3: Flow diagram of the Nagoya type III antenna [Ref. 46]

There are three variants of the Nagoya Type III antenna: (1) a straight bi-directional, (2) a right-handed helical, and (3) a left-handed helical. These antenna variants are shown in Figure 2.4, where the **B** and **k** are moving from right to left. As such, the right-handed helical antenna has leads twisting in a counterclockwise direction seen from a stationary observer (Figure 2.4 middle). A left-handed helical antenna has leads twisting in a clockwise direction (Figure 2.4 right). The twisting direction of the helical antennas are not to be confused with the rotation direction of the helicon wave, which depends on the excitation mode. Furthermore, the rotation direction of the helicon wave is determined with respect to the direction of the base magnetic field, B_0. Table 2.1 has the relationship between helical antennas and wave polarization with respect to the base magnetic field.

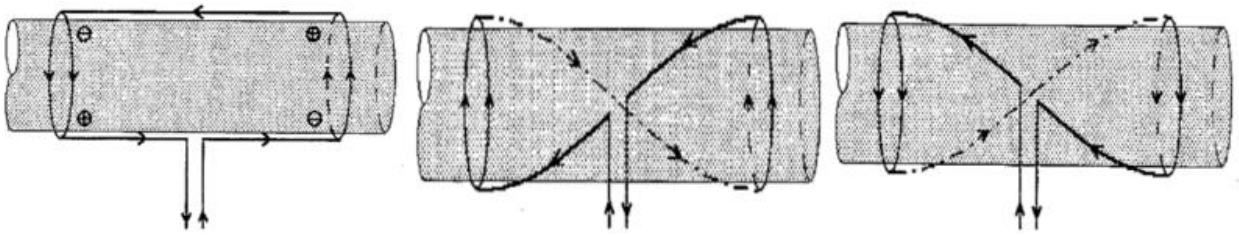

Figure 2.4: Nagoya Type III Variants: Straight, Bidirectional polarized antenna (left), right-handed helical antenna (middle), and left helical antenna (right). [Ref. 40]

Table 2.1: Relationship between helicon antenna and wave polarization

Type of Helicon Antenna	Wave Polarization	
Nagoya Type III	**Parallel to B_0**	**Antiparallel to B_0**
Right-handed helical	Right-handed circular polarized ($m = +1$) wave	Left-handed circular polarized ($m = -1$) wave
Left-handed helical	Left-handed circular polarized ($m = -1$) wave	Right-handed circular polarized ($m = +1$) wave

In helicon experiments, it was determined that the $m = +1$ wave mode is preferentially excited in all three antenna variants of the Nagoya Type III antenna. Two-dimensional imaging has shown that the right-handed helical antenna provided a long, dense plasma in comparison to the other variants where the plasma density would decrease axially along the z direction [Ref. 47]. In HPH experiments, the left helical Nagoya Type III demonstrated higher peaked density profiles for source diameter and length of 7 cm and 15 cm respectively [Ref. 48]. As such, the HPH clustered research used left-helical antennas with a base magnetic field aligned antiparallel to the phase velocity, to preferentially excite the $m = +1$ mode with the aim of achieving high plasma densities in the source region.

Extending beyond the dispersion theory for helicon waves in bounded plasmas, a dispersion relationship is needed to better predict downstream wave propagation of helicon

sources; specifically, a dispersion relation for the whistler mode, for helicon sources propagating into regions of weaker magnetic fields. Stenzel and Urrutia have taken the first 3D spatial and time-resolved measurements of whistler wave properties in highly non-uniform magnetic fields [Refs. 49-51]. The research on whistler modes in non-uniform fields may provide key insights about the importance of orbital angular momentum and its effect on wave propagation in helicon plasma thrusters, which exhibit a flaring magnetic field in the exhaust region.

In addition to understanding the whistler wave properties downstream from the source, it will be equally important to understand the interaction of a cluster of whistler-mode helicon sources. In the next section, phased arrays are introduced as a possible arrangement scheme for improving the electrical coupling efficiency, beam collimation, and specific impulse of the HPH cluster experiment.

2.2 Plasma Phased Arrays

Phased-arrays are commonly used to increase directivity of RF communications as illustrated in Figure 2.5 (left). The phases of the different wave fronts are used to constructively build the signal strength to values of 10-20 dB or greater depending on the number of elements included [Refs. 52-54]. The directed power generated in this manner can be much greater than the simple addition of the same number of units acting independently. Figure 2.5 (right) illustrates the changes in the energy directivity as one moves from a single antenna system to 4 and 16 element systems using the Ansys HFSS simulation package. Even with a modest array, gains of 10 dB or more can be easily achieved.

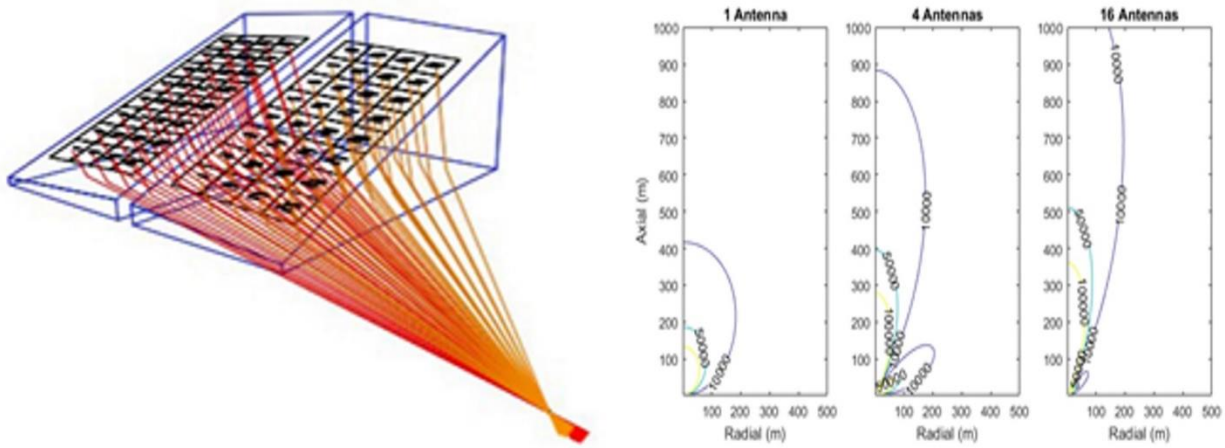

Figure 2.5: RF phased array where the different wave fronts are used to constructively add to create high directivity over large scale lengths (left), and calculated increase in directivity for various array sizes where the individual elements have dipole radiation patterns (right).

The plasma phased array seeks to demonstrate that the same type of power amplification can be generated by a phased-array of RF generated plasma sources. Because the RF propagates well beyond the plasma generation region, this research aims to use the same physics as an RF phased array to generate a plasma phased array (PPA). The main difference is that the RF is embedded in the plasma so that both are entrained in a PPA. In addition, if a system could be used where the collimation of each element is greater than the dipole elements in Figure 2.5, then even greater overall directivity could be achieved. The development of such a PPA would be a significant innovation for advanced in-space electric propulsion.

An excellent candidate for the PPA is the high-power helicon plasma thruster [Ref. 20], which not only produces a high density (10^{19} m^{-3}) plasma using high power (100's kW) RF interactions, but the radio waves are known to propagate well beyond the source region [Ref. 55]. These helicons operate at frequencies in between 0.5 – 1 MHz so that the power units can be supported by fast solid-state switches that allows power transfer with short (ms) rise times. The

solid-state switching system also means that the power supply for each of the units can be very compact. Another important feature of the system is that it operates in a nonlinear regime where $\Delta B/B$ is of order unity so that the wave interaction occurs by non-resonant particle trapping which causes all particles in the population to be swept up or trapped in the wave fields. This trapping means that both beam and ambient plasma particles can be trapped in the wave fields, with the trapping of ambient particles adding to the overall efficiency of the system.

Because of these developments, this research aims to create a compact multi-element phased beam-plasma system that can generate very fast high-power beam interactions. In prior work, a double gun helicon source was implemented and tested to measure a 20 – 50 % increase in the velocity and momentum flux profiles [Ref. 56]. Those results showed that a two-element PPA, in a parallel configuration, can yield more directed energy than by just increasing the power on a single element system.

Extending beyond previous work, the clustered helicon experiment, in a linear phased array configuration, seeks significant improvement in the ion beam collimation and specific impulse. In a linear phased array configuration, the structural chassis of the two-element PPA source has been upgraded to include downstream magnetic nozzles and mechanical adjustment of PPA elements with the aim of increasing the technology readiness level (TRL) from 2 to 3. Further details of the system components will be discussed in the next section.

Chapter 3. Experimental Apparatus

The HPH cluster experiment, in a linear phased array configuration, seeks to optimize thruster performance by adding downstream magnetic nozzles from the source region. The thruster architecture has been upgraded to adjust the relative spacing between thrusters. Initial operation and testing included a cluster of two HPH thrusters (12.7 degree off-parallel yaw angle and 15.8-degree pitch angle) firing simultaneously into a larger downstream nozzle. Figure 3.1 shows the experimental setup of the HPH cluster system, with labeled thruster naming convention and coordinate system. The sub-components of the HPH cluster experiment are discussed in the subsequent sections within this chapter.

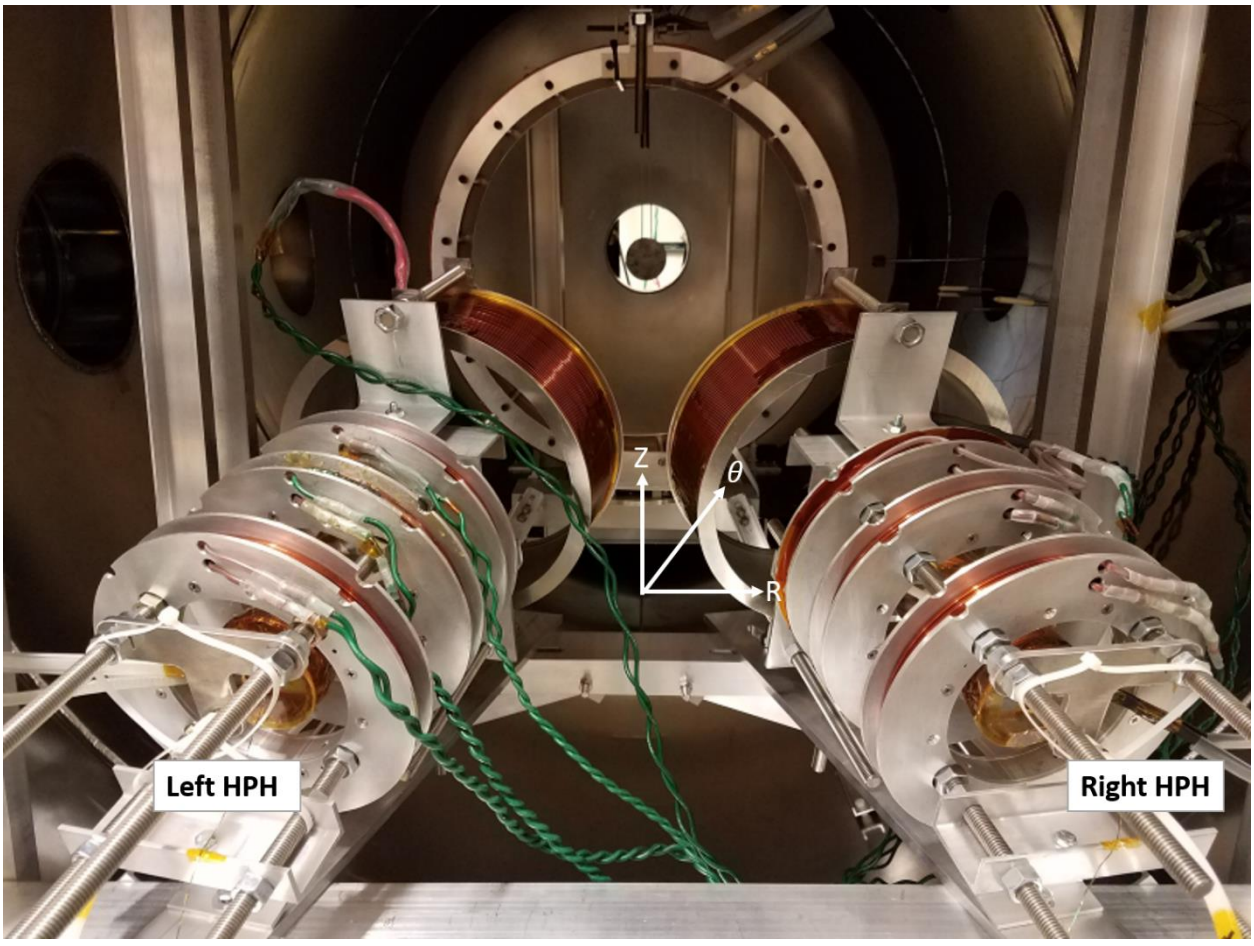

Figure 3.1: Experimental setup of the HPH cluster, including thruster naming conventions.

3.1 Vacuum Facilities and Neutral Effects

The vacuum chamber simulates a space-like environment for HPH system operation. The vacuum facility is a large cylindrical chamber ~ 4800 L, 2.7 m long with a radius of 0.75 m, featuring several flanges equipped with electrical, gas, and optical feed-throughs. The base vacuum pressure is achieved in two stages. First, a Varian DS-602 rotary vane rough pump lowers the chamber pressure to about 20 mTorr. Once the pressure drops below 20 mTorr, a Varian Turbo-V 551 turbo-molecular pump is turned on, which lowers the pressure to around 3±2 μTorr. At pressures above 10^{-4} Torr, the pressure is monitored by Pirani gauges. At pressures below 10^{-4} Torr, the pressure is monitored using a Bayard-Alpert ion gauge. Figure 3.2 shows the external features of the large vacuum facility.

At the beginning of an experimental shot, the fast puff valve is triggered. After a time-delay of about 76 ms, the gas transitions from the puff valve entrance to the source region. The pre-ionizer and the antenna are then triggered for $1\,\mu s$ and $200\,\mu s$ respectively. For a $200\,\mu s$ thruster discharge with ≤12 ms of gas injection, there is not sufficient Argon neutral density to backfill the vacuum facility [Ref. 41], minimizing the effect of plasma interactions with neutrals. Throughout the shot duration, the chamber pressure remains at the $4\,x\,10^{-6}$ Torr, which satisfies Randolph's limit for characterizing thruster plumes and minimizing the impact of neutrals on plasma production and acceleration [Ref. 57].

A low background pressure is desirable to minimize the impact of plasma interactions with neutrals, which could have an anomalous effect on the characterization of thruster plumes. The mean free path must be calculated to ensure space-like conditions are maintained, to improve the characterization of downstream plume properties. The mean free path for ionization can be expressed as in equation 3.1, where λ is the mean free path, n is the neutral gas density, and σ

cross sectional area for Argon propellant. The neutral gas density can be determined using a modified form of ideal gas law as shown in equation 3.2 [Ref. 58], where P is the pressure in Torr, and T is the temperature in Kelvin.

$$\lambda = \frac{1}{n\sigma} \tag{3.1}$$

$$n = 9.65\ x\ 10^{24}\ \frac{P}{T} \tag{3.2}$$

At a pressure of $4\ x\ 10^{-6}$ Torr and temperature of 294 K, the downstream neutral density is calculated to be $1.3\ x\ 10^{17}\ m^{-3}$. The peak ionization cross section for Argon is $4\ x\ 10^{-19}\ m^2$ [Ref. 59], which gives a mean free path for ionization of 19 m. Since the mean free path for ionization is much larger than the diameter and length of the vacuum chamber, there should be negligible ionization effect downstream of the source. The cross section for elastic electron-neutral collisions is peaked at $10^{-19}\ m^2$, which gives a mean free path of 77 m. Furthermore, the cross section for ion-neutral collisions is peaked at $8\ x\ 10^{-19}\ m^2$, which gives a mean free path of 9.6 m. Since the mean free path for electron-neutral collisions and ion-neutral collisions are much greater than the physical dimensions of the vacuum facility, the downstream thruster plume properties can be characterized in a collision-less, space-like environment where neutral effects are negligible.

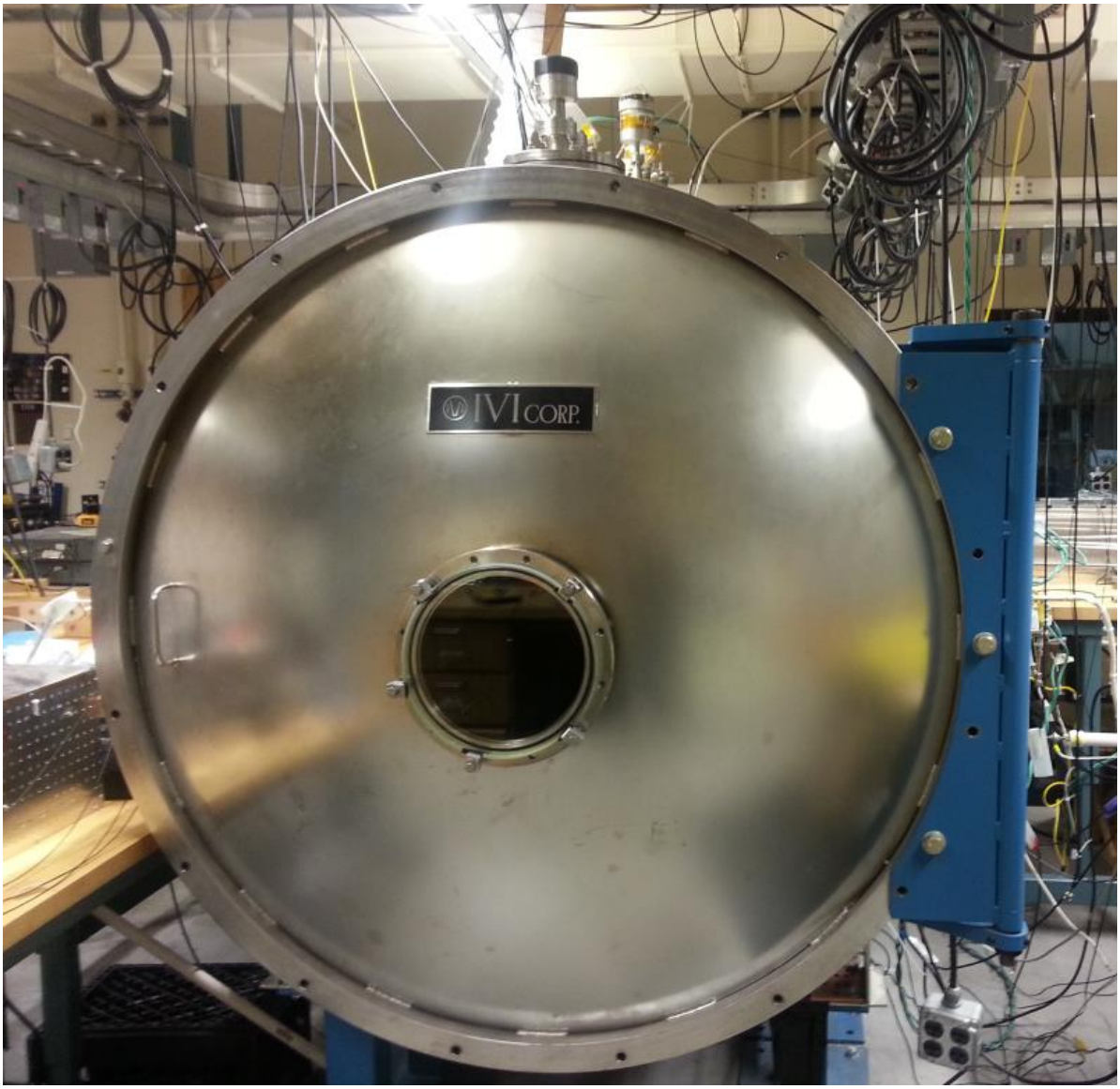

Figure 3.2: External features of the large vacuum facility ~ 4800 L at Advanced Propulsion Laboratory

3.2 Experimental Control and Data Acquisition System

Experimental control and data management is accomplished via a custom LabVIEW platform. The LabVIEW software controls the pulse width and duration of many key experimental apparatus, i.e. gas puff gates, igniter sources, magnets, helicon antennas, and spectrometer. Figure

3.3 shows the typical operating parameters defined in LabVIEW for the HPH cluster experiment. A fiber optic transmitter FTB8-1000 by Eagle Harbor Technologies, Inc is used as the interface board, allowing fiberoptic cables to transmit signals to all the experimental apparatus. Two Tektronix TDS 3034, 4-channel oscilloscopes were used to display and collect experimental data. The data is then stored via LabVIEW and converted to text files. The text data files are then exported into Python for post-processing analysis.

Figure 3.3: Typical operating parameters within LabVIEW experimental control

3.3 RF Power Generation Systems

RF plasma generation is accomplished using a custom-built solid-state power supply. The resonant RLC network driven by insulated gate bipolar transistors (IGBT) drives peak-to-peak current ≥1.2 kA at a frequency of 625 kHz to the helical antenna, an order of magnitude lower in excitation frequency than most helicon experiments. Figure 3.4 (left) shows the electrical schematic of the resonant RLC network. Figure 3.4 (right) shows the internal components of the power supply. The power supply contains 300 V charging capacitors (blue), an array of 8 IGBTs, a fiber optic trigger receiver, and an IGBT driver. The tuning capacitors (black), set at 36 nF, are used to tune the LC circuit to the desired operating frequency.

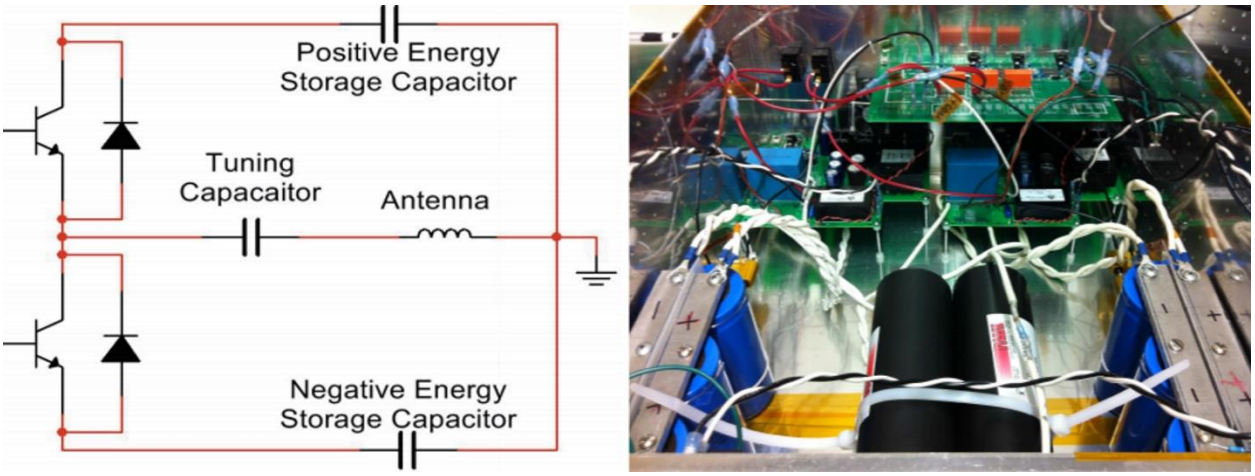

Figure 3.4: Electrical schematic diagram of the resonant RLC network (Left). Internal features of the solid-state power supply (right).

3.4 Gas Injection & Pre-Ionization Systems

The gas feed assembly includes (1) a pressure management assembly to regulate gas pressure (2) a gas puff valve, and (3) a pre-ionization igniter source, which is shown in Figure 3.5. The pressure management assembly, not shown in the schematic, includes a pressurized tank of inert gases, typically Argon for the HPH cluster experiment, to regulate the pressure reaching the gas puff valve. The gas puff valve (Parker 009-1669-900 fast pulse valve), shown in Figure 3.6, provided consistent gas flow control in the time durations between 1 – 40 milliseconds. The gas puff valve is opened for the desired duration using a 200 V output, IGBT drive circuit. After the gas flows through the valve, it travels into the vacuum chamber via gas injection lines connected in-line with each respective thruster source region.

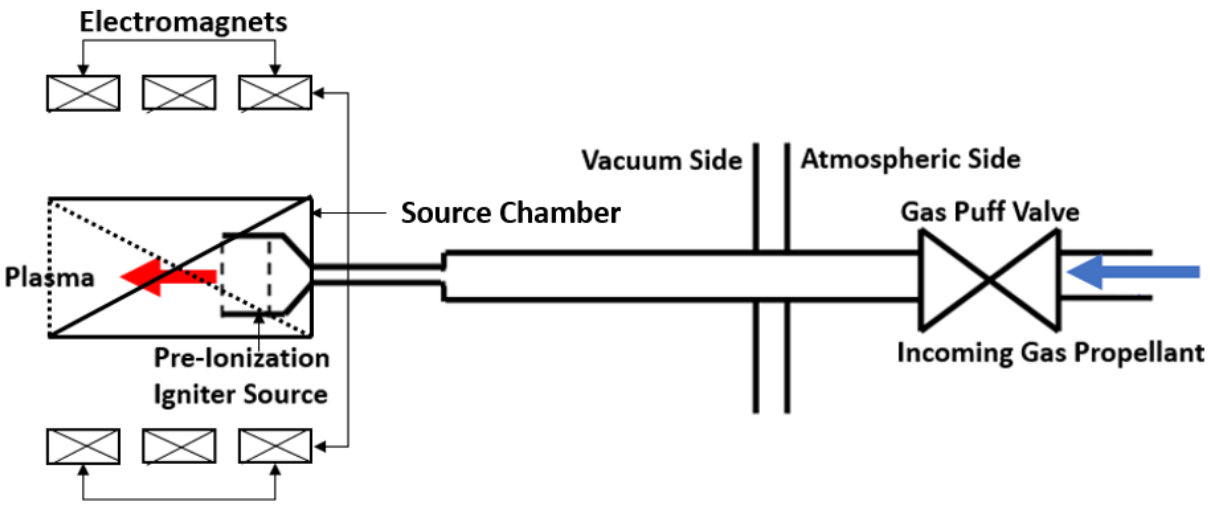

Figure 3.5: Gas feed assembly includes a pressure management system, a gas puff valve, and a pre-ionization source to generate seed plasma inside the cylindrical source tube.

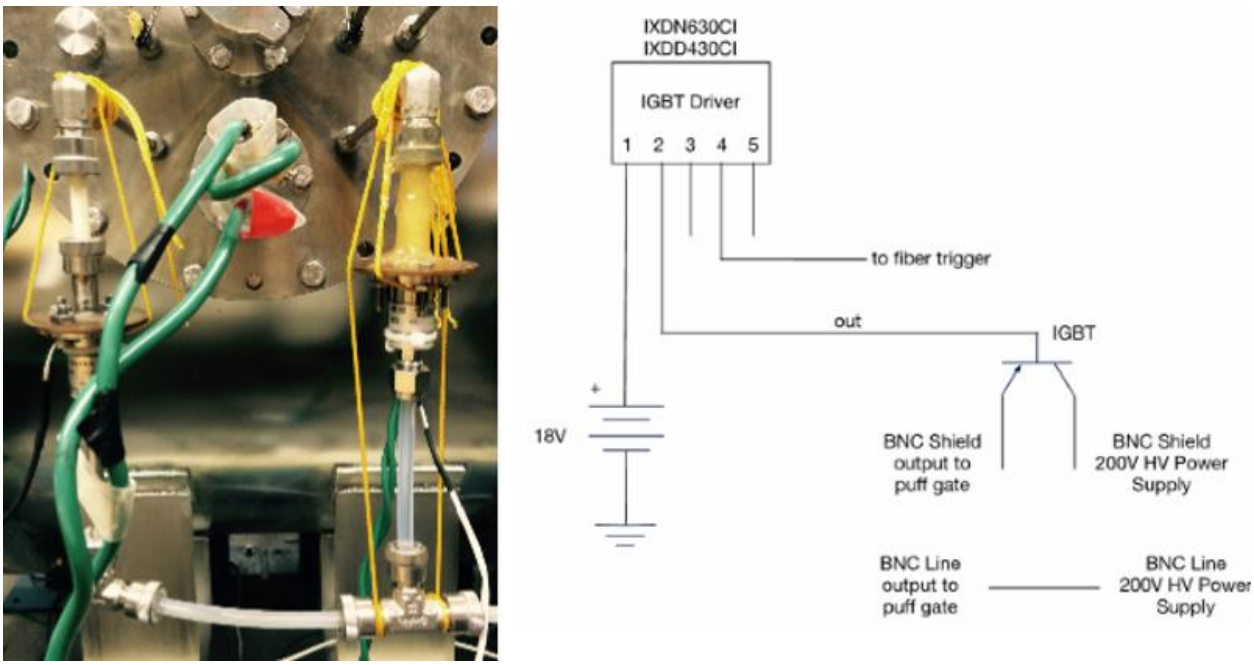

Figure 3.6: Gas Puff Valves (Left) and IGBT Controller Circuit (Right)

A pre-ionization igniter source is connected in-line with each gas feed assembly to initiate reliable plasma discharges. Figure 3.7 shows the design and development of the igniter sources. The pre-ionization igniter source is positioned 5 cm into the source region, along source centerline. The pre-ionization system creates an electric arc across two parallel steel grids at a potential of 1600 V for a duration of 1 µs. Once Argon gas is injected into the source tube, the pre-ionizer is turned on to create seed plasma. Figure 3.8 (left) shows the IGBT circuit board for the pre-ionization stage. Figure 3.8 (right) shows an un-calibrated trace from a Rogowski coil of the pre-ionization source.

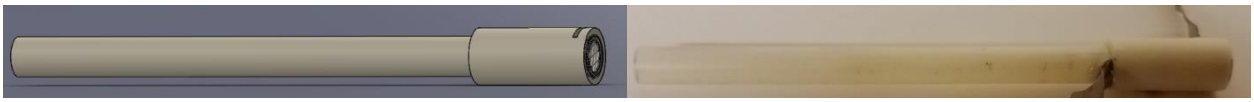

Figure 3.7: Pre-ionization source: design (Left) and actual (Right) using ceramic alumina tubes for electrical isolation

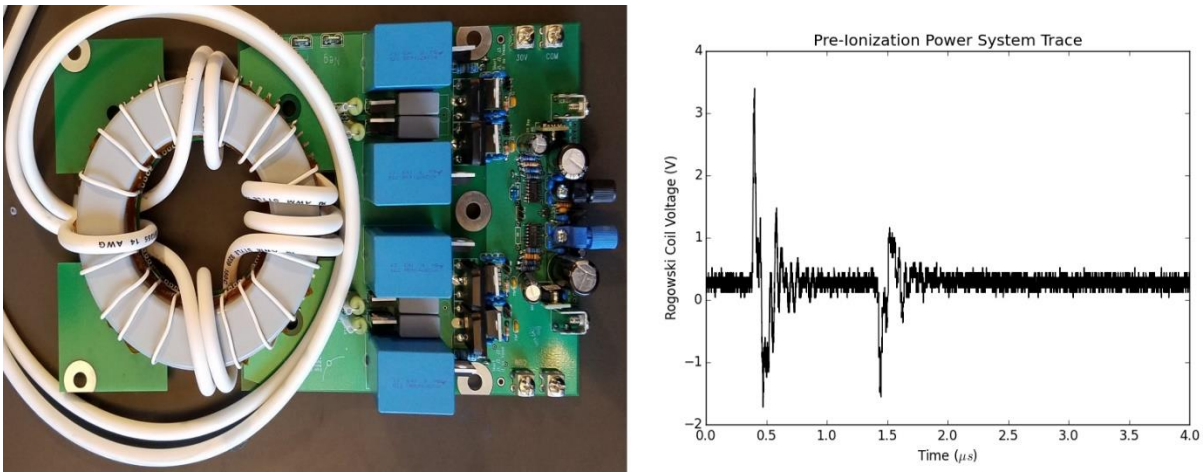

Figure 3.8: Pre-Ionization Power Circuit (Left) and Typical Operational Trace (Right)

3.5 RF Antenna Design, Development, and Electrical Characterization

In previous experiment campaigns, a left-handed helical Nagoya Type III antenna was used to excite the helicon ($m = +1$) wave (Refs. 55-56). For the HPH cluster experiment, a left-handed Nagoya Type III helical antenna was also chosen for its ability to maintain a high plasma density throughout the source region. Figure 3.9 (left) shows the design of a left helical antenna wrapped around the source tube. Figure 3.9 (right) shows the constructed left helical antenna wrapped around the source tube. Kapton tape is used to insulate the copper braids from each other and prevent arcing.

Figure 3.9: Left-handed Nagoya Type III helical antenna, (Left) design and (Right) actual

During experimental operation, the clustered system is operated in a pulsed manner, turning on the helical antennas for a 200 μs duration to minimize facility effects and simulate space-like conditions. Neutral gas is injected into the system using an IGBT gas puff circuit to allow ≤12 milliseconds of Argon gas per shot. Figure 3.10 shows a typical current trace for left HPH and right HPH thrusters firing simultaneously at a charge voltage of 262.5 V. For both current traces, the antenna current builds up to ~ 1.5 kA peak to peak until there is sufficient neutral gas density in the source region to load the RLC circuit i.e. plasma loading.

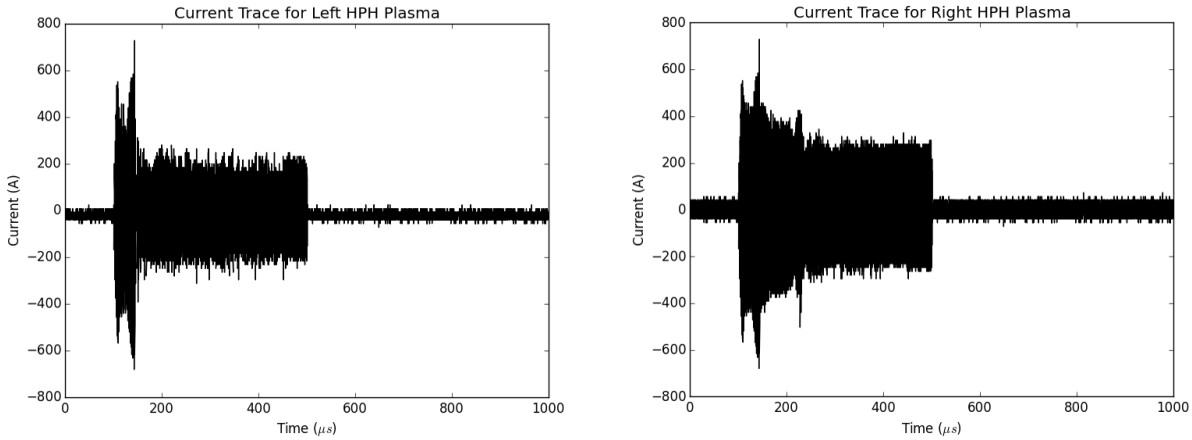

Figure 3.10: Electrical discharge characteristics of Left HPH (Left) and Right HPH (Right) thrusters

3.6 Magnet Power Systems

There are three sets of electromagnets in the clustered system. The 1st set is the base magnets that provide ionization in the source region, producing operational field strengths ranging from 0 – 200 G. The 2nd and 3rd sets are the medium and large downstream magnetic nozzles respectively, used to shape the plasma a distance away from the source region. The downstream magnetic nozzles produce field strengths ranging from 0 – 100 G. The first two sets are powered by laboratory direct-current power supplies. The third set is powered by a high current IGBT pulse power supply. Table 3.1 lists the physical dimensions and attributes for base, medium, and large magnets while a side-view illustration is shown in Figure 3.11.

Table 3.1: Base Magnet and Downstream Magnetic Nozzle Attributes

	Base Magnets	Medium Magnetic Nozzle	Large Magnetic Nozzle
Radius [cm]	7.3	9.5	23
Width [cm]	17.2	11	11
Number of Turns of Wire	43	26	60
Current [A]	Variable	Variable	Variable
Operational Magnetic Field Strength [G]	0 – 200 G	0 – 100 G	0 – 100 G
Power Supply	10 kW DC Power Supply (Functional)	DC Power Supply (Functional)	IGBT Pulsed Power Supply (Functional)

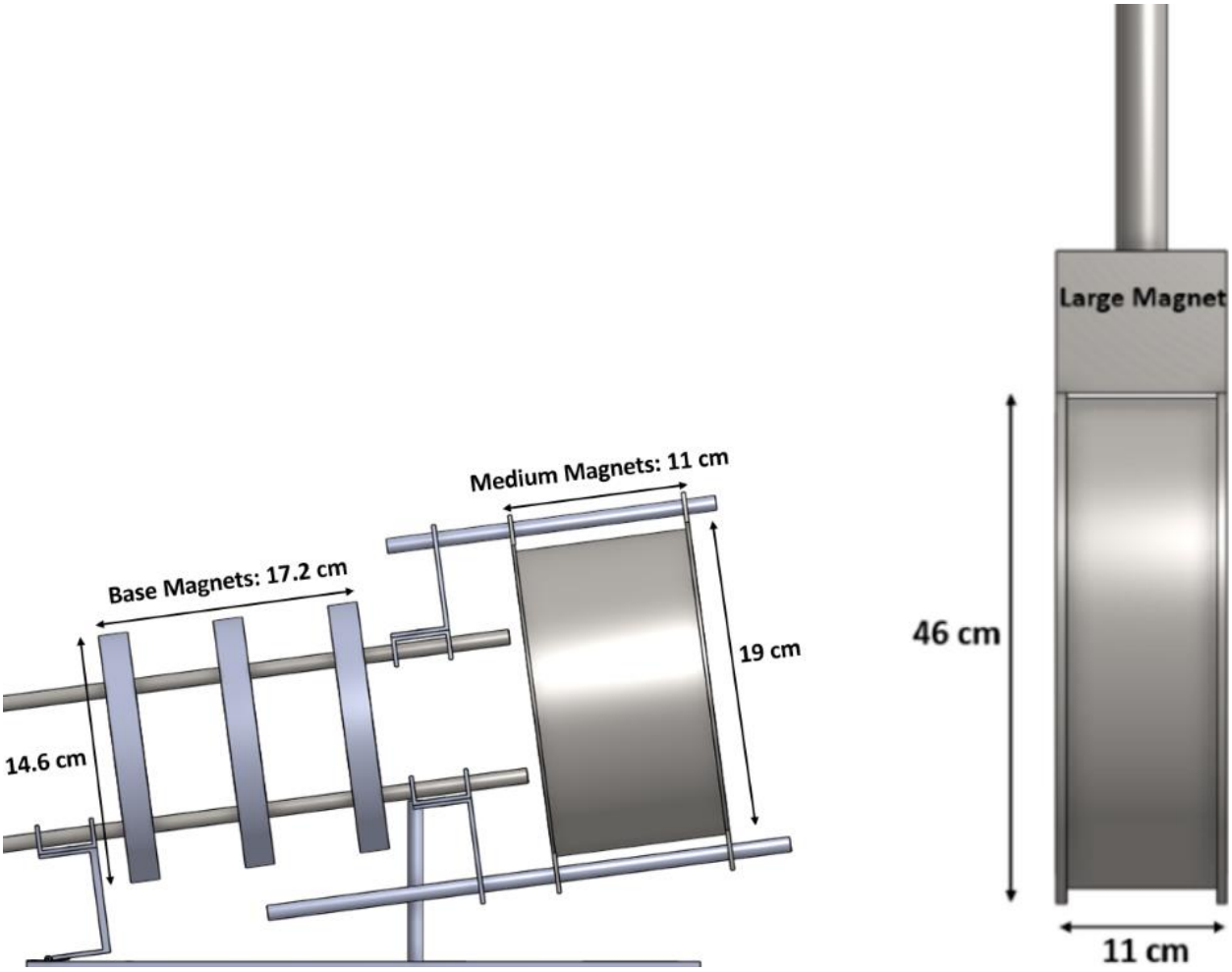

Figure 3.11: Side-view illustration of the base, medium, and large magnets

3.7 Magnetic Field Optimization

Prior to turning on the electromagnets, a magnetic-static simulation of the HPH cluster system is provided by the finite element method magnetics (FEMM) software. FEMM software provides flexibility in solving two-dimensional planar electromagnetic problems to better predict system performance. During this experimental campaign, there are three cases of interest. The base electromagnets are turned on for the first case. Base and medium electromagnets are turned on for the second case. Base, medium, and large electromagnets are turned on for the third case. Figure 3.12 illustrates the experimental setup, with the helicon source and the base magnets upstream of the Z = 0 line. The 1st and 2nd magnetic nozzles are located downstream of the source region. For this research, there is interest in understanding how the plume properties change as adjustments in field strength and axial location are made to the magnetic nozzles, i.e. medium magnet (1st nozzle) and large magnet (2nd nozzle). Two magnetic nozzle configurations have been initially implemented to determine the variations in thruster performance. For both configurations, the current values for the base magnetic field, 1st magnetic nozzle, and 2nd magnetic nozzle are 45 A, 25 A, and 20 A respectively, unless stated otherwise.

The first magnetic nozzle configuration has the 1st nozzle and 2nd nozzle located 9.8 cm and 45.8 cm downstream of the source region. Figure 3.13 illustrates the change in magnetic topology as the 1st, 2nd, and 3rd cases are activated. As the downstream magnetic nozzles are turned on, the field lines begin to extend further from the source region. In case three (Figure 3.13 bottom), there are more magnetic flux lines originating from the source region passing through the large magnetic nozzle. This would suggest increasing the current in the downstream magnetic nozzles would create a flux conserving configuration. A flux conserving configuration would

allow for more thermal energy to be converted into kinetic energy, enhancing ion beam collimation on thruster axis.

The second magnetic nozzle configuration has repositioned the 2nd magnetic nozzle while maintaining the axial location of the 1st magnetic nozzle. The 1st and 2nd nozzle axial locations are 9.8 cm and 33.8 cm downstream of the source region. Figure 3.14 illustrates the magnetic topology with all magnet systems active (case three). With the 2nd nozzle closer to the source region, there is an increase in the magnetic field strength in the source, while more magnetic flux lines pass through the large magnetic nozzle than in Figure 3.13 bottom, suggesting enhanced beam collimation and ion velocities downstream of the source. An axial magnetic field profile of the second magnetic nozzle configuration is shown in Figure 3.15. The axial magnetic field is peaked at $3.87\ x\ 10^{-2}\ T$ (387 G) at Z = 0 and has a $B_z \sim 1/r^3$ decay into a weaker magnetic field far from the source.

For the purposes of this research, the two magnetic nozzle variants will be referred in the analysis section as far flux conserving (variant 1) and close flux conserving (variant 2) configurations. A combination of plasma diagnostics was used to characterize the thruster plume properties as adjustments are made to thruster architecture toward a compact form factor.

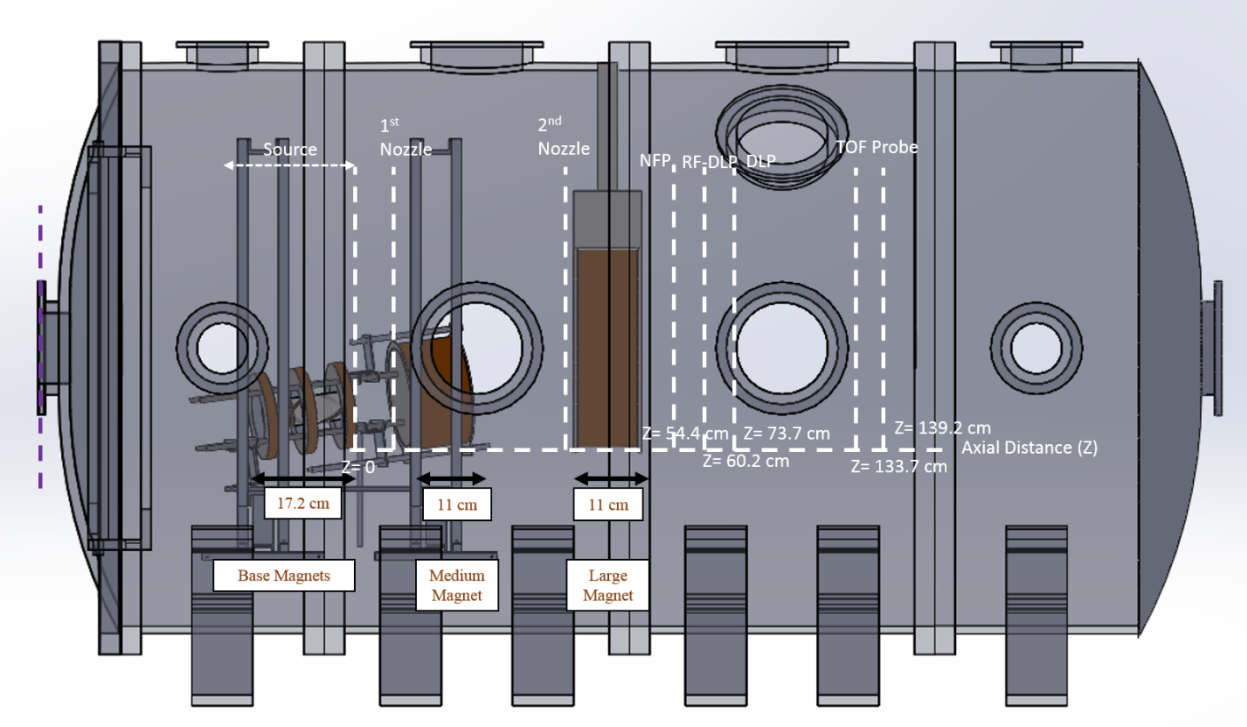

Figure 3.12: Side-view illustration of the experimental setup, with labels for the Z=0 zeroth line, the 1st magnetic nozzle, 2nd magnetic nozzle, and probe diagnostics.

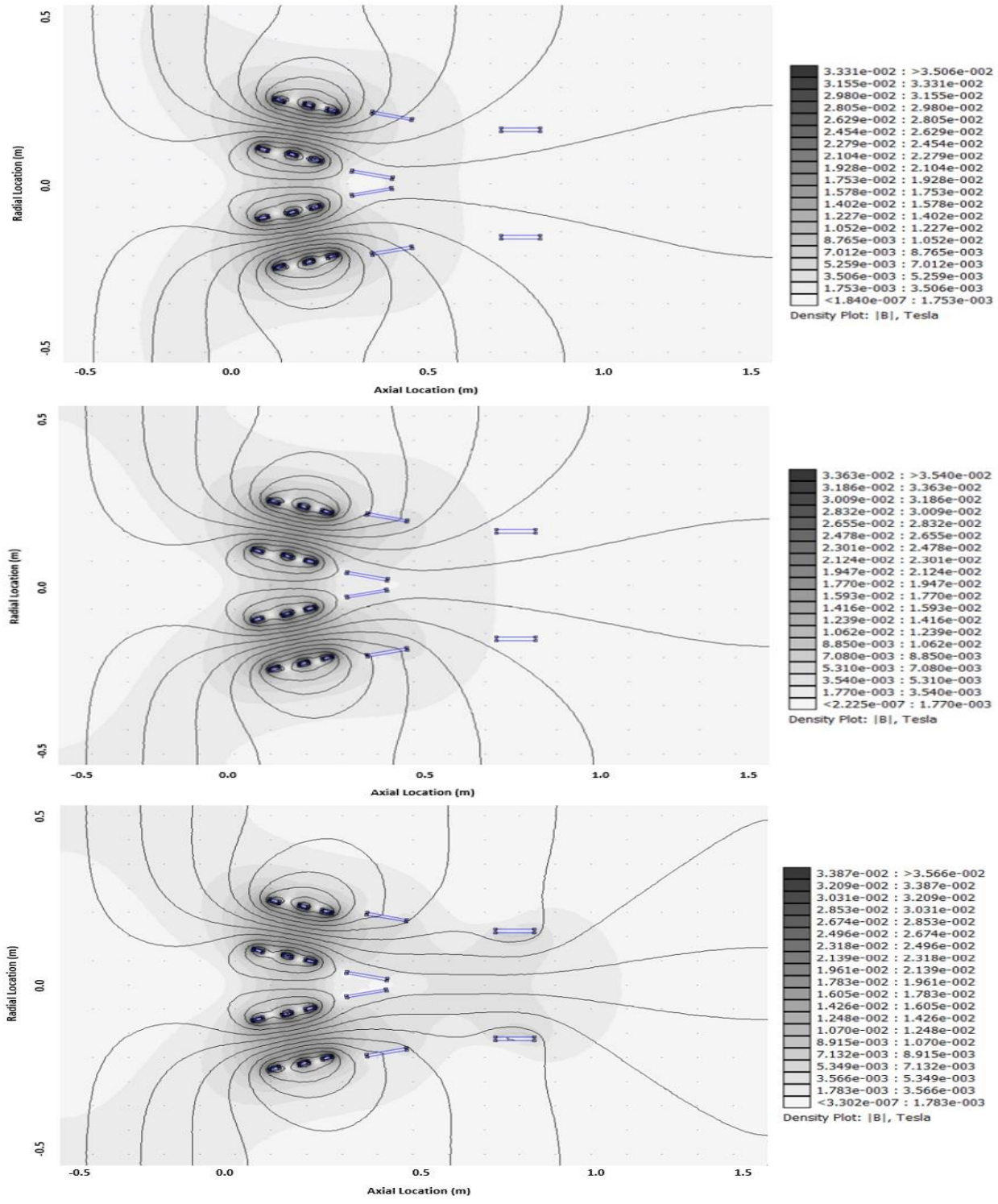

Figure 3.13: FEMM magneto-static simulation (variant 1) for three cases of investigation: (Case 1) 1st set of electromagnets (base) active – Top, (Case 2) 1st and 2nd set of electromagnets active (base and medium) – Middle, (Case 3) All electromagnets active (base, medium, large) – Bottom.

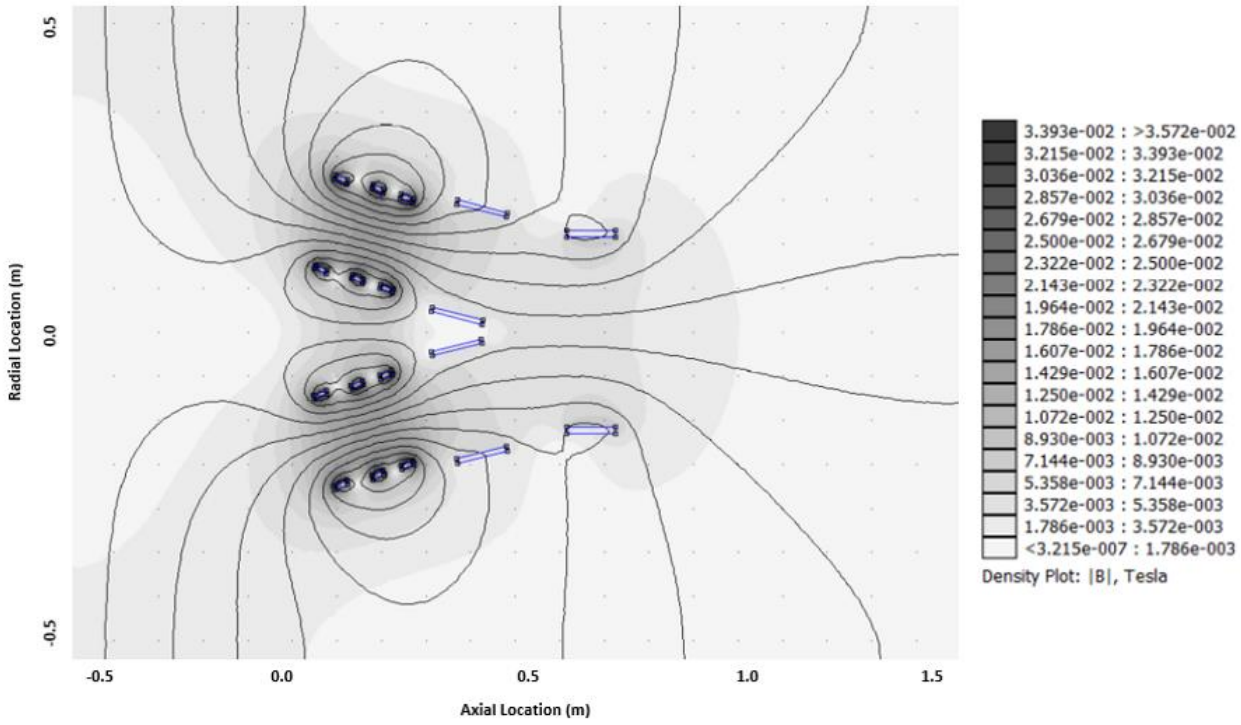

Figure 3.14: FEMM magneto-static simulation (variant 2): case three investigation with all electromagnets active.

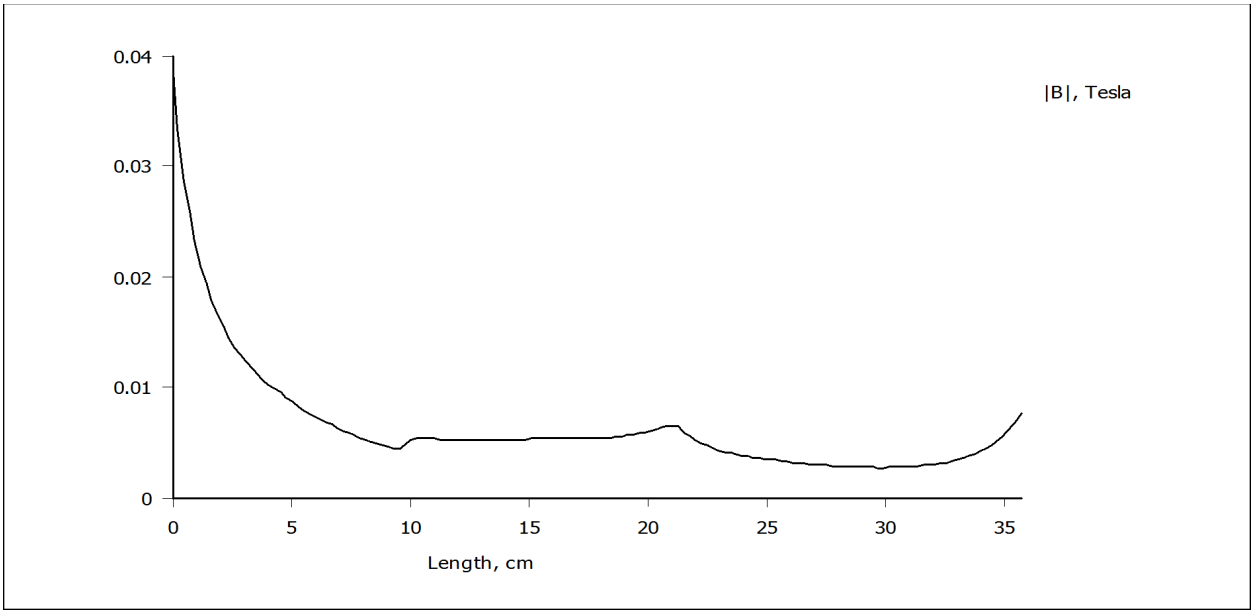

Figure 3.15: Axial magnetic field profile away from the Z = 0 source region (variant 2 – close flux conserving configuration)

Chapter 4. Plasma Diagnostics

The goal of the HPH cluster system is to characterize the helicon source over a wide variety of operating conditions, tuning the system to obtain a desirable thruster performance. With all the upgrades to the vacuum facility, optical emission spectroscopy (OES) and high-speed imaging are initially used to streamline the tuning process. Spectral measurements allowed for the determination of plasma ionization fraction in the source region. The high-speed imaging system provided physical insights about the plume dynamics.

Once system settings have been optimized, a suite of intrusive plasma diagnostics is used to characterize the downstream plume properties. Double Langmuir probes are used to determine electron density and temperature. A time-of-flight probe, consisting of two adjacent double Langmuir probes at axial locations, is used to determine the bulk ion velocity of the plasma plumes. The RF-compensated double Langmuir probe (RF-DLP) can better account for plasma potential fluctuations and provide a better prediction of the electron temperature. The retarding potential analyzer (RPA), also commonly referred in literature as the retarding field energy analyzer (RFEA), is used to measure the ion velocity distribution function (IVDF). A nude Faraday probe is used to determine the ion current density and estimate the beam divergence angle of the plasma plume. In each sub-section, the details of each diagnostic are further explained.

4.1 Optical Emission Spectroscopy

Optical emission measurements are gathered using an Ocean Optics HR 2000 spectrometer with a spectral bandwidth of 375 – 815 nm and resolution of 0.54 nm. The spectrometer is connected to a fiber-lens collection system to characterize the plasma ionization fraction. An

Ocean Optics HG-1 calibration source is used to calibrate the instrument. Figure 4.1 shows the general setup of the emission measurement system. It consisted of a 400-micron optical fiber, a collimator lens, and a gimbal mount system to tilt the collection system toward the optimum field of view. An optical enclosure box is placed over the fiber-lens system prior to data collection. Figure 4.2 shows a fiber-lens collection system mounted onto a platform centered along the front viewing window. The platform is portable, allowing users to view emissions from either front, side, or back viewing ports.

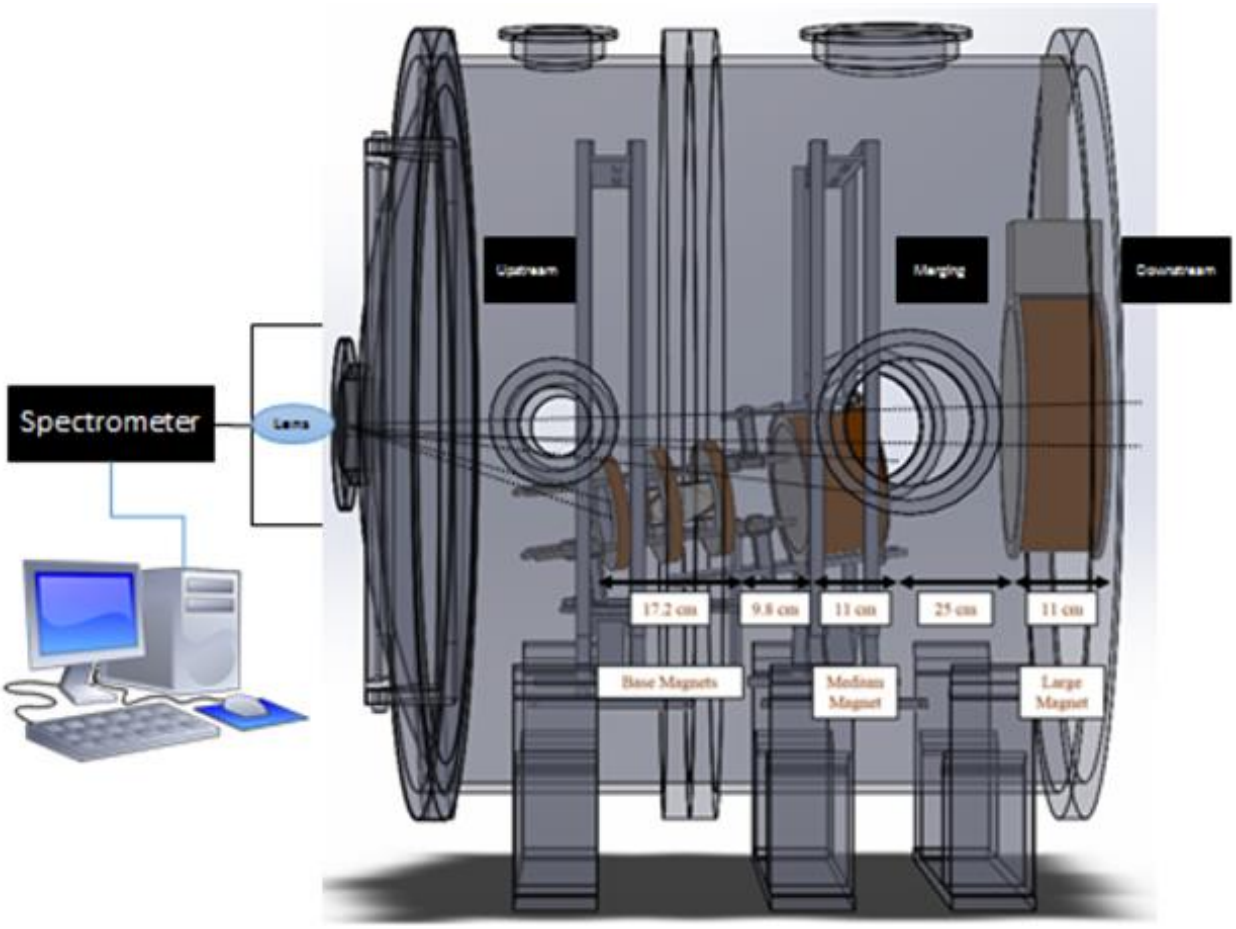

Figure 4.1: General setup of spectroscopic data acquisition system

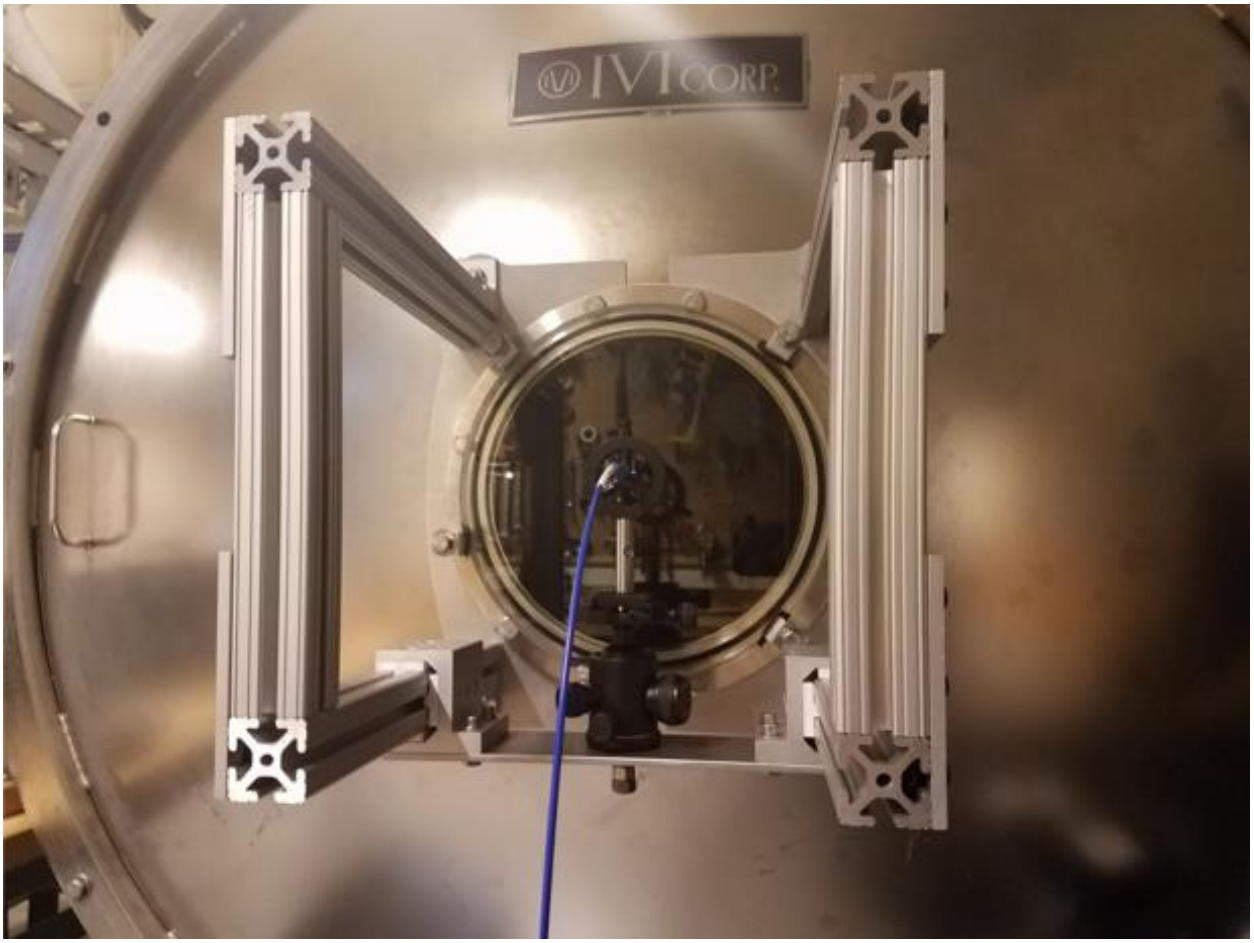

Figure 4.2: Fiber-lens collection system mounted onto the spectroscopy platform

4.2 High Speed Visualization Camera

An Edgertronic high speed imaging camera is used to visualize the plume dynamics for a variety of operational parameters. The camera can capture features up to 18,000 frames per second at reduced resolution. Figure 4.3 shows the imaging camera setup. The camera is mounted on a gimbal mount system, allowing users to tilt the system to observe features at various locations in the vacuum facility. The entire setup is enclosed by an optical enclosure box when running the experiment. The camera is run at 1,500 frames per second for most shots.

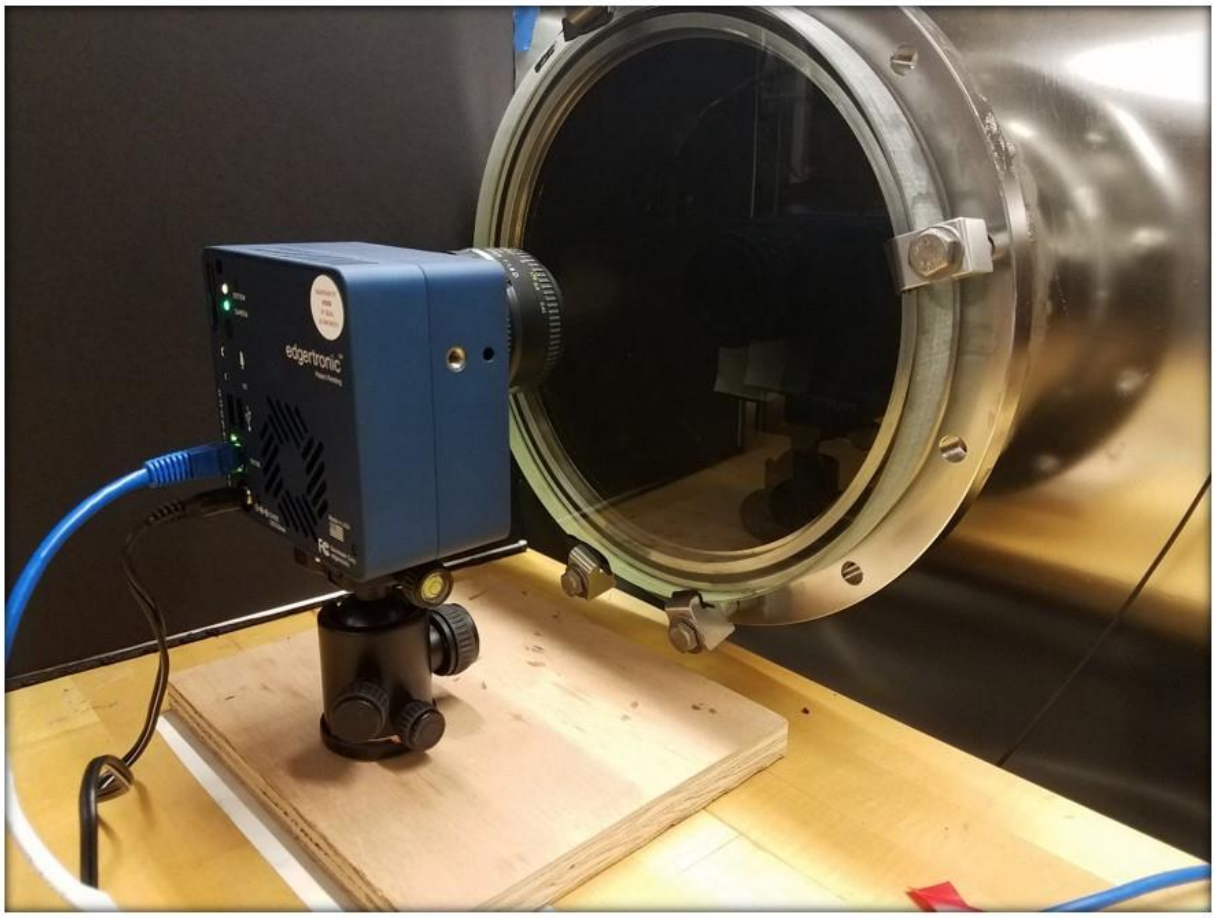

Figure 4.3: High speed imaging setup

4.3 Symmetric Double Langmuir Probe

Symmetric double Langmuir probes (DLPs) are used to measure the electron density downstream of the helicon plasma source and estimate the ion velocity using a time-of-flight technique. The design of these double Langmuir probes is similar in design methodology as previous HPH experiments [Refs. 20, 24, 41, 48]. The Langmuir probe tips are made from tungsten with filleted corners to remove sharp points that could inadvertently influence the electric field. For these probes, the tip diameter, tip length, tip separation, and probe area are 1.05 mm, 5.04 mm, 2.10 mm, and $1.75x10^{-5}\ m^2$ respectively. The tungsten probe tips are epoxied into an alumina

ceramic tube and electrically connected via crimps to magnet wire that is fed through a 6.35 mm stainless steel tube to a quick disconnect outside the vacuum chamber. The end leads of the magnet wire are connected to a BNC connector that attaches to the Langmuir probe circuitry.

A typical image of a radial downstream probe can be seen in Figure 4.4. The double Langmuir probe is electrically floating with respect to chamber ground but maintains a constant potential across the probe tips. A typical Langmuir probe circuit is shown in Figure 4.5. The potential across the probe tips is supplied by a bank of batteries to isolate the probe circuitry from RF and electrical noise from external equipment. The plasma typically interacts with the probe for a few hundred microseconds. As such, the battery is slow to give up current during this period; thus, a fast-acting capacitor is included to alleviate the issue. The probe is electrically isolated from the oscilloscope via a Stangenes 1:1 isolation current transformer. The current from the probe is passed through the isolation transformer 25 times, making it a 25:1 transformer. The 25:1 transformer increases the signal to noise ratio, allowing for the signal to be measurable on the oscilloscope. The signal is then passed through a low-pass RC filter to minimize RF noise. The data is saved via a LabVIEW program and later exported into an external Python code to perform post-processing analysis.

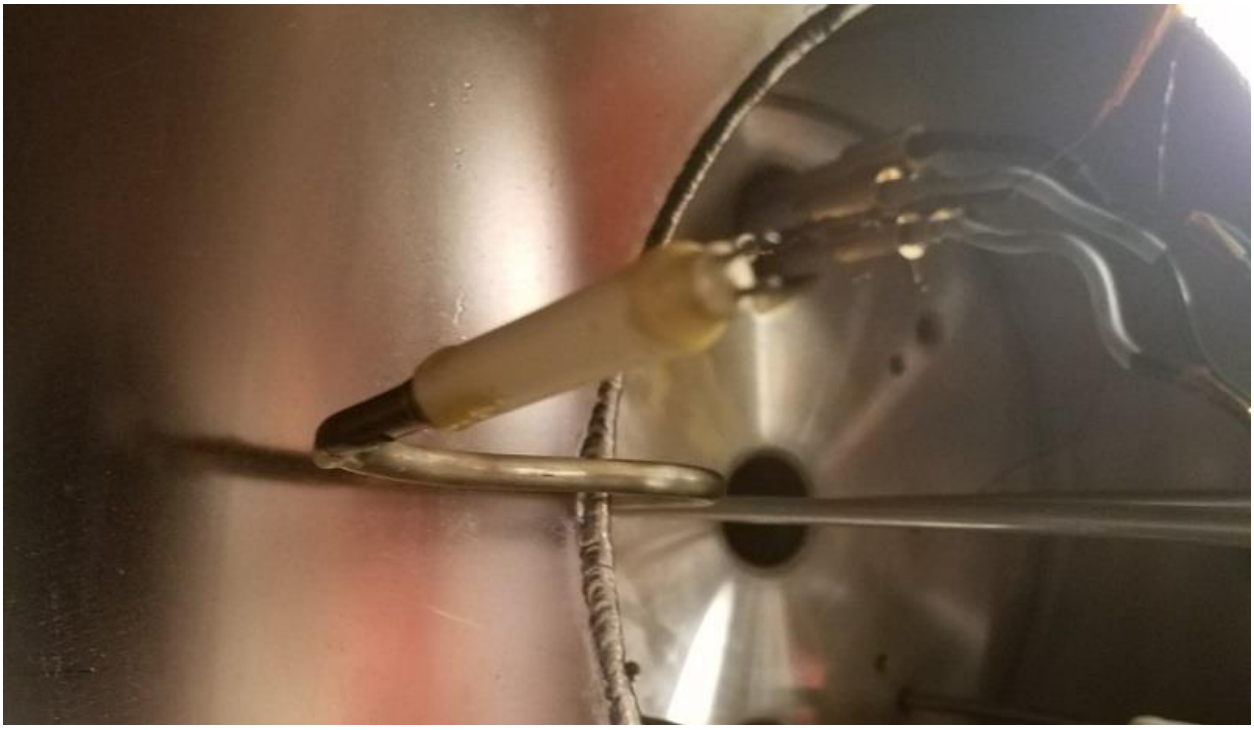

Figure 4.4: Radial downstream double Langmuir probe

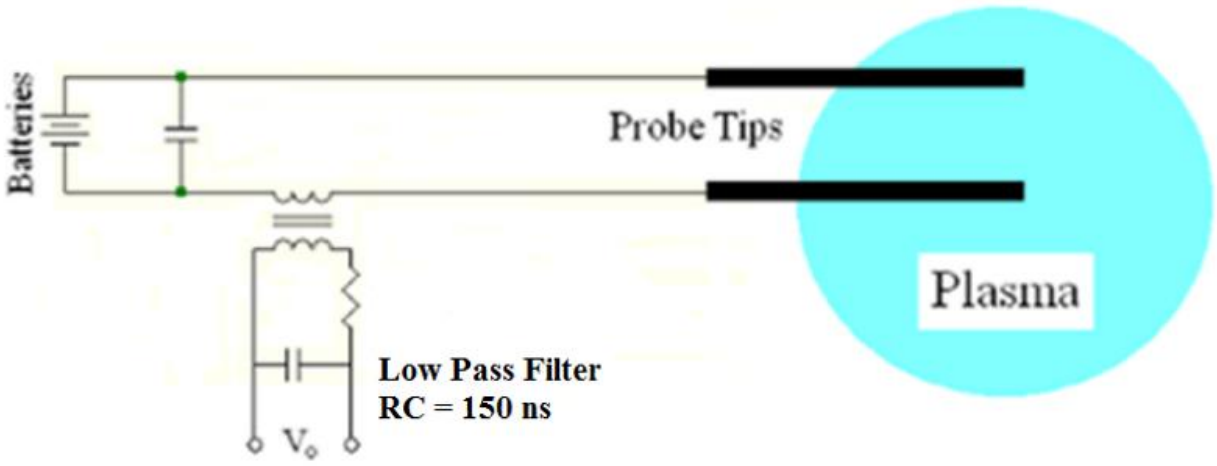

Figure 4.5: Electrical circuit for the double Langmuir probe

For this research, the electron temperature is assumed to be 10 eV based on prior work by Ziemba et al. [Ref. 20] in the testing of the HPH prototype. This is satisfactory since the

downstream radial probes are used to predict the relative changes in electron densities as operational control parameters, i.e. RF power, magnetic field intensity, gas injection rate, are adjusted. For all double Langmuir probe measurements, the probe is operated in ion saturation regime, whereby a high negative bias potential allows only ion current to be detected by one probe tip. For HPH cluster sources, Equation 4.1 provides a relationship between the ion saturation current and the electron density using a thin-sheath approximation. Using a thin-sheath assumption, the sheath area A_s is proportional to the probe area.

$$I_{i,sat} = -\exp\left(-\frac{1}{2}\right) en_0 A_s \sqrt{\frac{k_B T_e}{m_i}} \tag{4.1}$$

The time-of-flight (TOF) probe technique uses two double Langmuir probes, separated an axial distance of 5.5 cm, 13.5 cm, or 73.5 cm apart from one another, to estimate the average ion velocity of the thruster plumes. The TOF probe is oriented perpendicular to the flowing plasma and located at the thruster centerline. Using the 5.5 cm probes illustrated in Figure 4.6, the time of flight of the plasma from the upstream probe toward the downstream probe can be determined using the time at peak current for each respective probe.

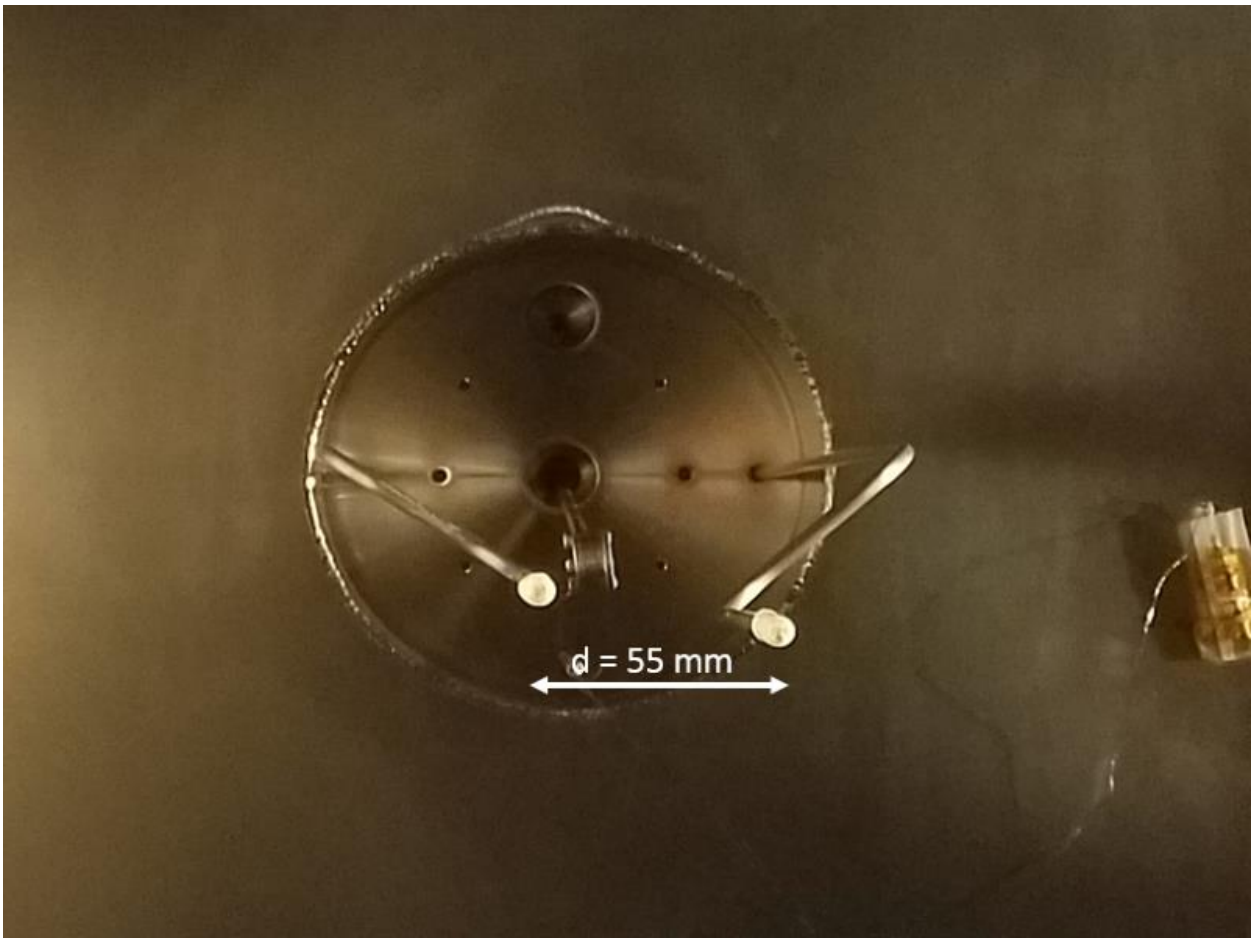

Figure 4.6: Time-of-flight probe consists of two double Langmuir probes separated an axial distance of 55 mm.

Traditionally, double Langmuir probes are used in non-flowing plasma experiments where the chamber walls and probes can reach equilibrium conditions. For the HPH cluster experiment, all conditions downstream of the source region must be treated as transient phenomenon. To address the transient phenomenon and better estimate the electron temperature downstream of the source, an RF-compensated double Langmuir probe is built to minimize the plasma fluctuations and distortions to the characteristic I – V Langmuir curves. The next section provides further details about the development of a RF-compensating double Langmuir probe.

4.4 RF-Compensated Double Langmuir Probe

An RF-compensated double Langmuir probe (RF-DLP) is constructed to compensate for oscillating plasma potential typically observed in helicon plasma sources and better predict the electron temperature. The RF-DLP uses a series of self-resonating inductors, tuned at the first and second harmonic frequencies i.e. 600 kHz and 1.2 MHz, coupled with an auxiliary electrode to compensate for the high frequency noise on the probe tips. An auxiliary electrode, connected to each probe tip, is used to capacitively couple local plasma oscillations with a capacitor of value 1 nF to lower the high frequency loading on the probe tips. An electrical schematic for the RF-DLP is shown in Figure 4.7. A constructed RF-DLP can be seen in Figure 4.8.

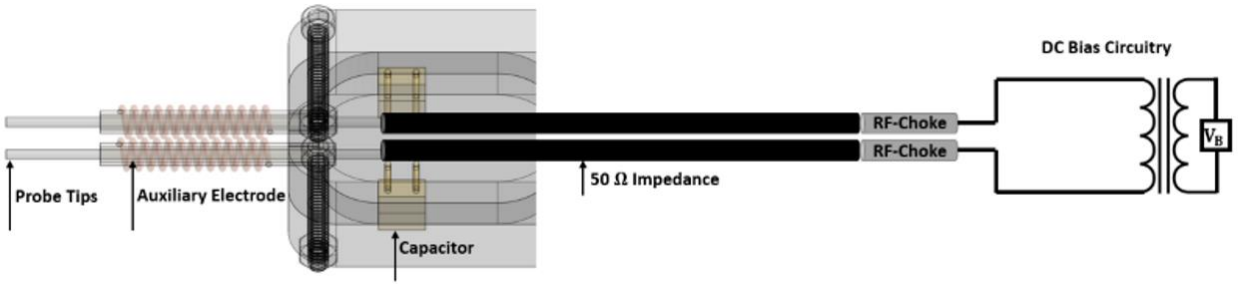

Figure 4.7: Electrical schematic for the RF compensated double Langmuir probe

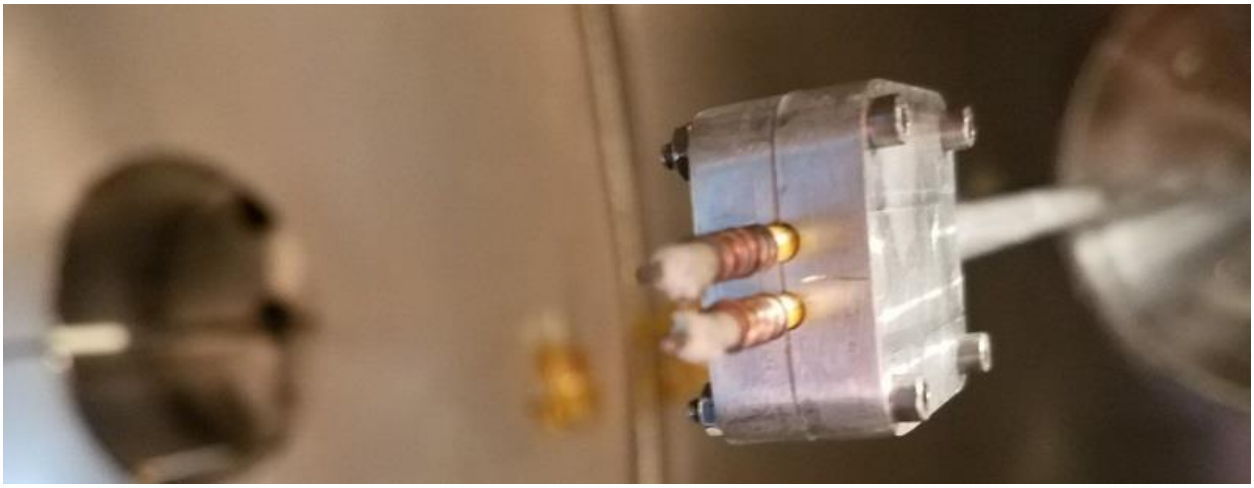

Figure 4.8: Fully assembled RF-DLP in the main vacuum facility

4.5 Retarding Potential Analyzer Probe

A retarding potential analyzer (RPA) probe uses a set of biased grids to selectively repel and/or attract plasma particles to measure the one-dimensional ion energy distribution. The RPA probe essentially acts as a high-pass energy filter, only allowing high-energy ions to pass through the grids while repelling electrons and low energy ions. The HPH cluster experiment uses a four-grid RPA design based off the work of Prager et al. [Ref. 41], where all grids are placed in alignment inside a metal housing with the collector plate detecting the current signal. The four-grid RPA electrical schematic shown in Figure 4.9. The first grid is grounded and acts as a reference to even perturbations in the plasma. The second grid is held at high negative bias potential to allow only ions to pass through while screening out electrons. The third grid has a sweeping voltage supply that discriminates against ions of different energy levels. The fourth grid is the suppressor and acts to repel secondary electrons from reaching the collector plate, improving the accuracy of the current response.

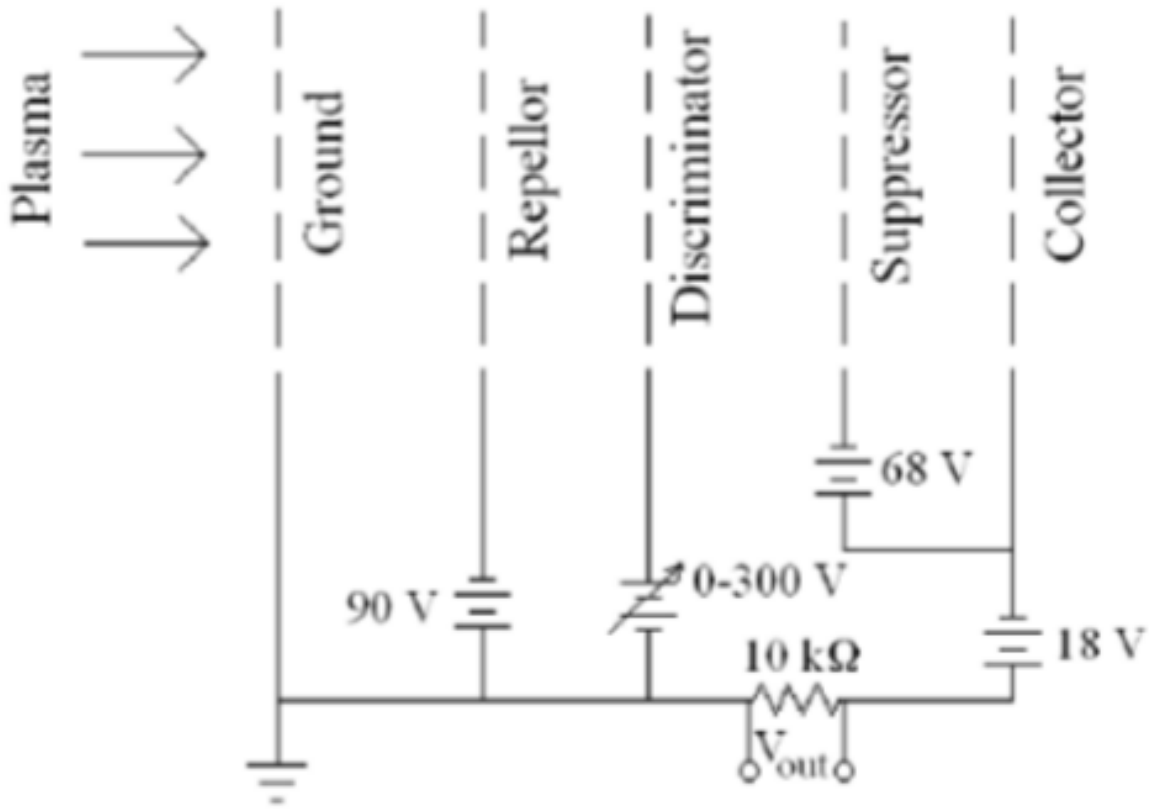

Figure 4.9: Electrical schematic of the four-grid RPA design

As the ions hit the nickel collector plate, electrons are stripped away from the collector allowing for a measurable current. The measurable current can be defined as:

$$I_C(V_d) = Ae < nv > \tag{4.2}$$

where A is the probe area, e is the ion charge, n is the ion density at the collector, and v is the ion velocity. The <nv> term represents the ion flux, which is also given by the second moment of the velocity space distribution function, f(v). The current from the RPA probe can be directly related to the IVDF using the following expression:

$$I_C(V_d) = Ae \int_{v_i}^{\infty} v f_v(v) dv \tag{4.3}$$

where v_i, the ion velocity, can be found by relating the electrostatic potential energy, based on the discriminator voltage, to the kinetic energy:

$$v_i = \sqrt{\frac{2eV_d}{m_i}} \tag{4.4}$$

where V_d is the third grid's discriminator voltage. By differentiating Equation 4.3 with respect to the discriminator voltage, the IVDF can be determined as follows:

$$\frac{dI_c}{dV_d} = -\frac{Ae^2}{m_i} f_v\left(\sqrt{\frac{2eV_d}{m_i}}\right) \tag{4.5}$$

Since Equation 4.5 does not accurately account for non-ideal scenarios, it typically is best practice to estimate the ion velocity distribution function based on the following relationship:

$$\frac{dI_c}{dV_d} \propto -f_v\left(\sqrt{\frac{2eV_d}{m_i}}\right) \tag{4.6}$$

Since the shape of the ion velocity distribution is a key factor, Equation 4.6 will be used to analyze RPA data for the HPH cluster experiment.

Key design attributes are based on the design by Prager et al. [Ref. 41], similar in design to previous helicon experiments [Ref. 60]. The probe dimensions can be shown in Table 4.1. A constructed RPA probe and its power electronics can be seen in Figure 4.10. The power electronics is housed in an aluminum box outside the vacuum chamber, including the batteries, discriminator power supply, and auxiliary components. For measurement of probe current, a Stangenes isolation current transformer is used. The output for the collector plate passes through a wire which is wrapped around the Stangenes transformer 55 times to boost the measurable current on the oscilloscope. During experiments, the discriminator voltage is maintained at a constant potential during a single plasma shot but vary the discriminator voltage on a shot-to-shot basis. Since HPH sources have good shot-to-shot repeatability, a plot of collector current as a function of discriminator voltage can be obtained as the discriminator voltage is varied from 0 V up to 80 V,

in increments of 2V or 5V. A sample characteristic IVDF curve for the RPA probe can be depicted in Figure 4.11.

Table 4.1: RPA probe dimensions

Component Name	Dimensions (mm)	Bias Voltage (V)
Rectangular Housing	24.9 mm x 19.5 mm x 12 mm	
Circular Entrance Orifice	1.0 mm diameter	
Grid Components:	Nickel Mesh Grid: 55% transparency Copper Washers: 0.3 mm thick Mylar Insulating Washers: 0.1 mm thick	
Ground Grid		0
Gap Spacing	0.4 mm (0.3 mm Copper & 0.1 mm Mylar)	
Repellor Grid		-90
Gap Spacing	0.9 mm (0.3 mm Copper & 0.6 mm Mylar)	
Discriminator Grid		0 – 300
Gap Spacing	0.4 mm (0.3 mm Copper & 0.1 mm Mylar)	
Suppressor Grid		-68
Gap Spacing	0.4 mm (0.3 mm Copper & 0.1 mm Mylar)	
Nickel Collector		-18
Gap Spacing	0.4 mm (0.3 mm Copper & 0.1 mm Mylar)	

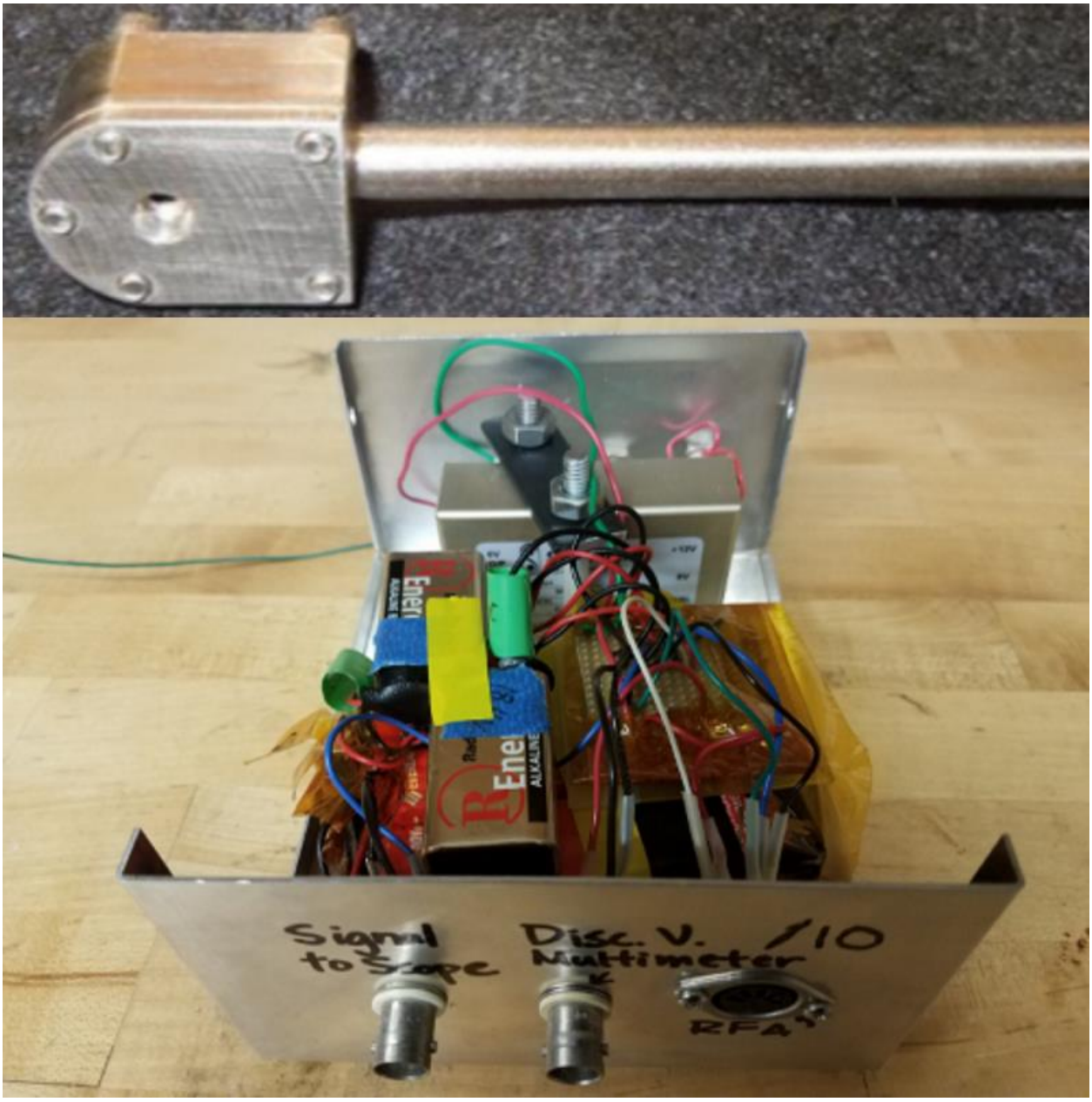

Figure 4.10: Constructed RPA probe (Top) with its accompanying power electronics (Bottom)

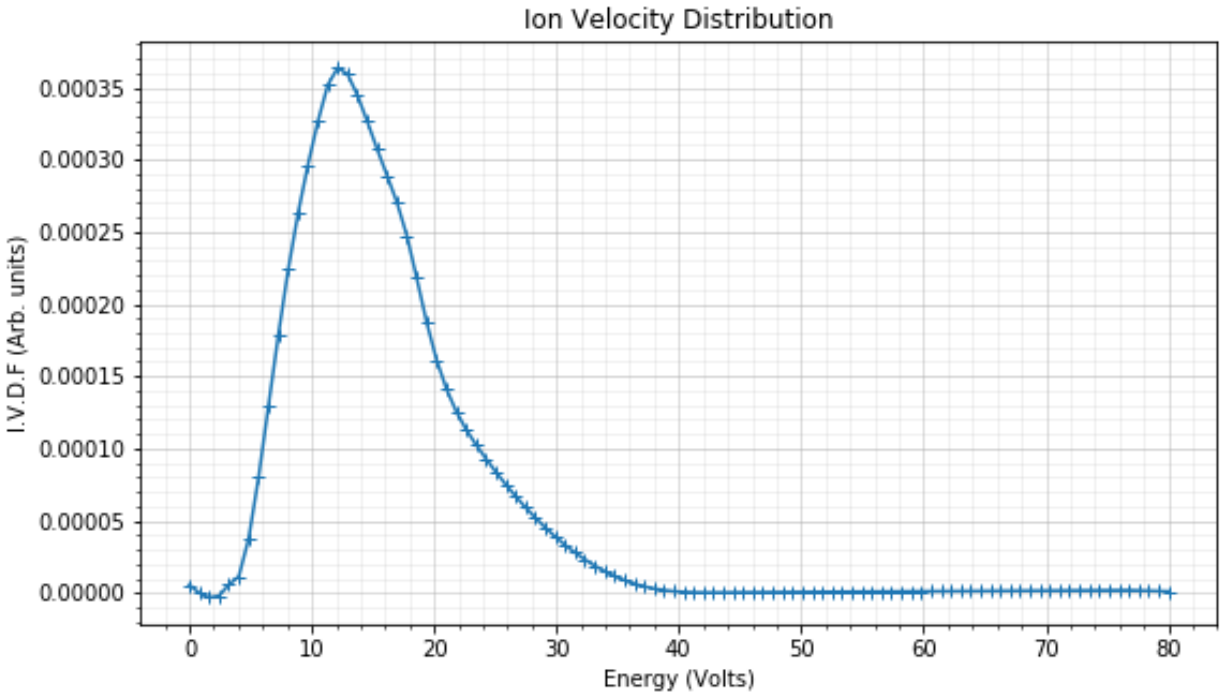

Figure 4.11: A sample characteristic IVDF curve

4.6 Nude Faraday Probe

The nude Faraday probe is designed to measure the ion current density in the downstream region of thruster plumes [Refs. 9, 35, 44, 61]. Nude refers to the fact that the probe does not have a filter upstream of the collector surface. The main function of the Faraday probe is to quantify the beam divergence angle θ by sweeping the probe radially inward and outward from the thruster centerline, that captures 90% of the total ion beam current. In ideal conditions, the beam divergence angle should be as small as possible, indicating that the ion velocity is mostly in the axial direction with minimal radial velocity motion. With a very low beam divergence angle, the thrust and specific impulse of an EP device can be optimized.

The nude Faraday probe consists of three components: (1) the collector, (2) the guard ring, and (3) the ceramic insulator. The collector is isolated from the guard ring using the ceramic

insulator. The collector is negatively biased to repel electrons while only allowing ions to impinge onto its surface, ensuring that the current collected is solely due to ion contribution, i.e. the probe operates in ion saturation mode. As the collector is sufficiently biased, a sheath will form around the collector surface. One of the major concerns with sheath formation is that it typically expands which can increase the effective collection area, leading to errors in the ion current density measurements. By biasing the guard ring at the same negative potential as the collector, a uniform flat sheath will form around the collector surface, minimizing sheath growth and reducing a source of error. In addition to having the same negatively biased potential as the collector, the guard ring must have an appropriate gap spacing, the gap between the guard ring and collector, of 5 – 10 Debye lengths to ensure that a uniform, flat sheath forms across the surface and not a bumpy one [Ref. 62]. A bumpy sheath would increase the effective collection area, thereby allowing low-energy ions to be collected by the probe, i.e. anomalous ion current measurement. With a guard ring spacing less than the estimated sheath thickness, the sheath edge effects are expected to be minimal. Since the collector and guard ring are isolated by a ceramic insulator, the effective collection area is equal to the area of the collector surface. The ion current density can be determined by dividing the current over the collector surface area.

The source of errors must be fully evaluated prior to the collection of ion current density measurements. Common error sources include: (1) secondary electron emission, (2) sheath edge effects, (3) probe misalignment, and (4) measurement circuit [Refs. 9, 44]. For the first source of error, secondary electron emission (SEE) from the probe surface will cause an anomalous effect on the measured ion current. The material for the collector surface should have a low SEE yield to minimize this source of error. For the second source of error, sheath edge effects can be minimized using a negatively biased guard ring and appropriate guard ring spacing. For the third source of

error, probe misalignment can lead to a reduction in the collection area. As the probe is swept radially inward or outward, operators must check the alignment of the collector face, ensuring that incident ions are impinging on the collector surface and not the gap in between the collector and guard ring. For the fourth source of error, the uncertainty of the measurement circuit is solely dependent on the uncertainty of the shunt resistance and the voltage measurement device.

For the HPH cluster experiment, the nude Faraday probe is constructed using three types of materials: (1) aluminum 6061, (2) 304 stainless steel, and (3) a machinable glass ceramic – Macor. A rod of aluminum 6061 is used to construct the structural housing for the Faraday probe. The structural housing holds the insulator, guard ring, and collector with an outer diameter of 22.900 mm. The insulator is constructed out of Macor with a diameter of 22.860 mm. The guard ring is constructed out of 304 stainless steel with an inner and outer diameter of 12.930 mm and 18.288 mm respectively. The guard ring spacing is set at 0.230 mm, which is 10 Debye lengths, and expected to provide a uniform flat sheath across the collector surface. The collector is constructed out of 304 stainless steel with a diameter of 12.700 mm. An exploded view of the HPH cluster nude Faraday probe is shown in Figure 4.12. The nude Faraday probe mounted into the vacuum facility is shown in Figure 4.13. Table 4.2 summarizes the relevant dimensions and component bias voltage. The electrical schematic of the probe can be depicted in Figure 4.14.

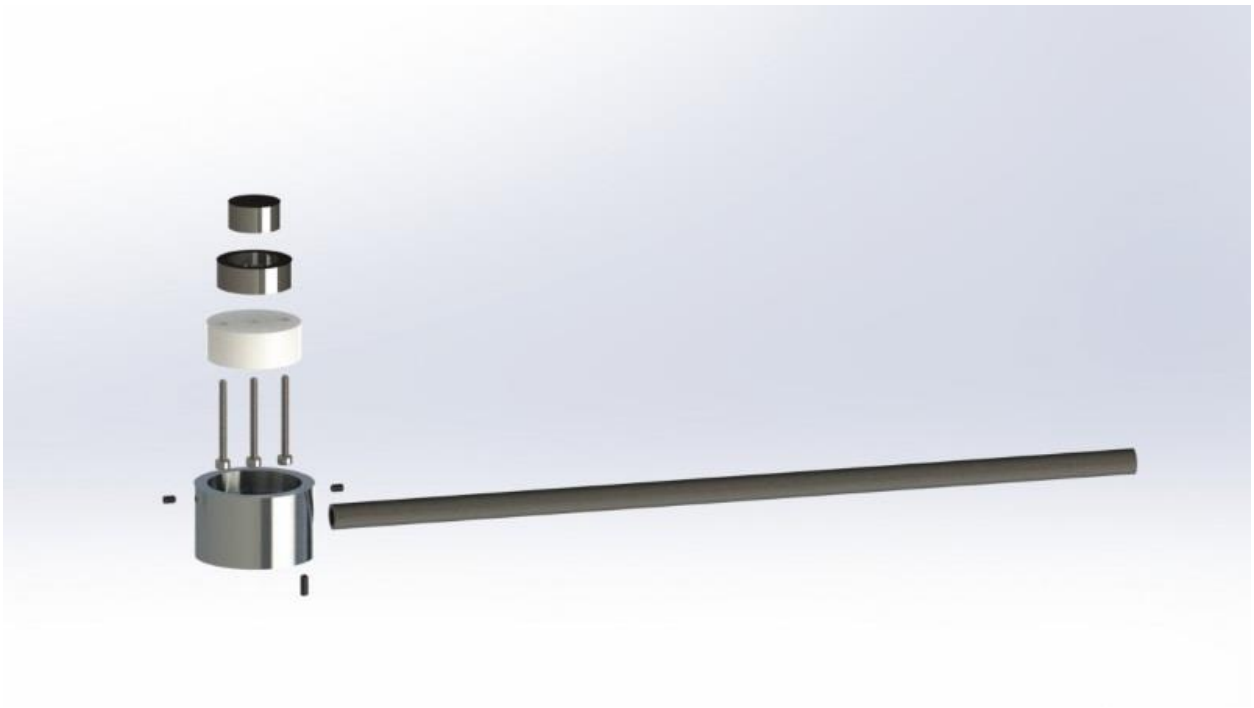

Figure 4.12: Exploded view of the internal components of the nude Faraday probe

Figure 4.13: Constructed nude Faraday probe

Table 4.2: nude Faraday probe dimensions

Component Name	Dimensions (mm)	Bias Voltage (V)
Probe Collector		-30.0
Outer Diameter	12.700	
Gap Spacing	0.230	
Probe Guard Ring		-30.0
Outer Diameter	18.288	
Macor Insulator		
Outer Diameter	22.860	
Probe Housing		
Outer Diameter	22.900	

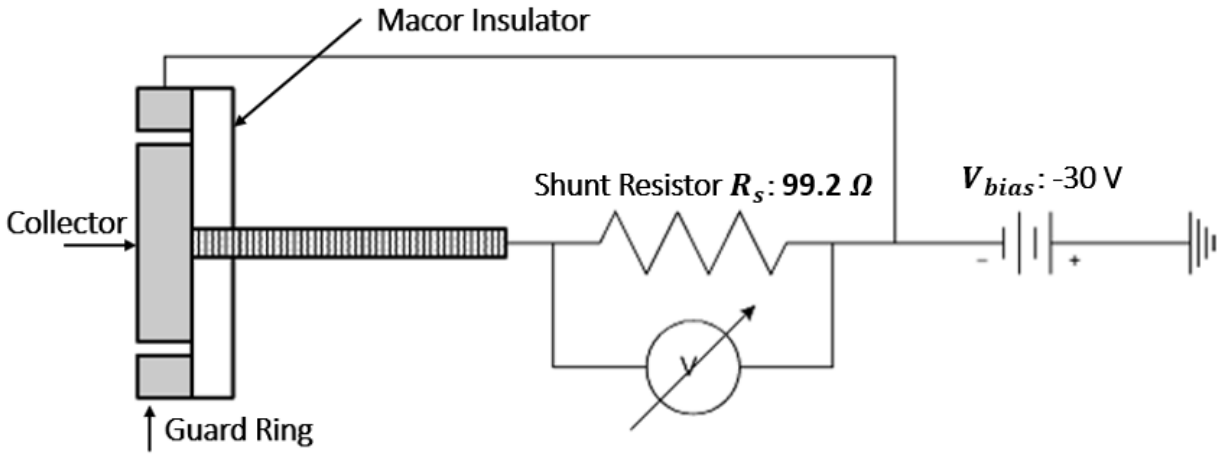

Figure 4.14: Electrical schematic of the nude Faraday probe

Chapter 5. Single Thruster and Double Thruster Characterization

For both single and double thruster characterization, the thrusters will operate in a pulsed manner. The duration of the helicon antenna, pre-ionization igniter source and gas injection are $200\ \mu s$, $1\ \mu s$, and 12 ms respectively. The current values for base magnet, 1st magnetic nozzle, and 2nd magnetic nozzle are 45 A, 25 A, and 20 A respectively. Table 5.1 provides a list of key operating parameters used during the HPH cluster experiment. For investigating the downstream plume properties, the HPH cluster experiment can be operated in three nozzle modes: (1) no nozzle, (2) 1st magnetic nozzle, and (3) 1st and 2nd magnetic nozzles.

Due to the pulsed nature of the clustered HPH experiment, a control probe diagnostic, typically DLP, is used to ensure shot-to-shot repeatability prior to collecting experimental data on the specifiic diagnostic for the day. An average of 10 shots are typically taken for each diagnostic to determining the temporal variation of the plume properties. An average of 3 shots are typically taken to account for spatial variations in the plume properties. Once the data is collected, it is exported as a text file and post-processed in an in-house multiplotting Python interface by averaging the data sets and applying a low-pass Buttersworth filtering scheme to smooth out data sets and remove noise. Although there is a small sampling size for the collected data, a 4% standard error was determined for all diagnostic measurements in this chapter and subsequent chapters.

Table 5.1: Key Operating Parameters – HPH Cluster Experiment

Key Sub-Systems	Operational Settings
Helicon Antenna Source	----------
RF Charge Voltage	262.5 V
Operational Frequency	625 kHz
Pulse Width	200 μs
Gas Injection Valves: Pulse Width	12 ms
Pre-Ionization Igniter Sources	----------
L. HPH Igniter Pulse Width	1 μs
R. HPH Igniter Pulse Width	1 μs
No Nozzle: Base Magnetic Field	Base magnet current at 45 A
1st Nozzle: Base Magnetic Field and 1st Magnetic Nozzle	Base magnet current at 45 A; 1st magnetic nozzle current at 25 A
1st and 2nd Nozzles: Base Magnetic Field, 1st Magnetic Nozzle, and 2nd Magnetic Nozzle	Base magnet current at 45 A; 1st magnetic nozzle current at 25 A; 2nd magnetic nozzle current at 20 A

Prior to the usage of the intrusive plasma diagnostics, optical emission spectroscopy and high speed imaging were used to provide a qualitative assessment of thruster performance. The spectroscopy platform can be tilted to determine the ionization fraction in either the left HPH or the right HPH source region. Figure 5.1 shows a comparison of Argon plasma spectra for the inductively coupled plasma (ICP) case, where there is no magnetic field, and the Helicon case, where a current of 45 A generates the base magnetic field. As can be seen in the figure, there are more ion emission lines (Ar II) in the 480 – 620 nm spectral range for the Helicon case suggesting improved ionization fraction. For a wavelength of 656.4 nm, the Helicon case has a relative intensity 2.7 times greater than the ICP case. As more Ar II lines become visible in the 400 – 500 nm range, a transition from a pinkish-reddish discharge to a bright blue discharge is a defining feature of all helicon systems [Ref. 63]. Figure 5.2 shows the initial plume dynamics for a clustered

HPH discharge. In the image, there are slight hue variations, with the left HPH exhibiting a characteristic blue while the right HPH exhibited a purplish-red. In the subsequent sub-sections, the downstream plume properties are characterized using the probe diagnostics for (1) the far flux conserving configuration and (2) the close flux conserving configuration.

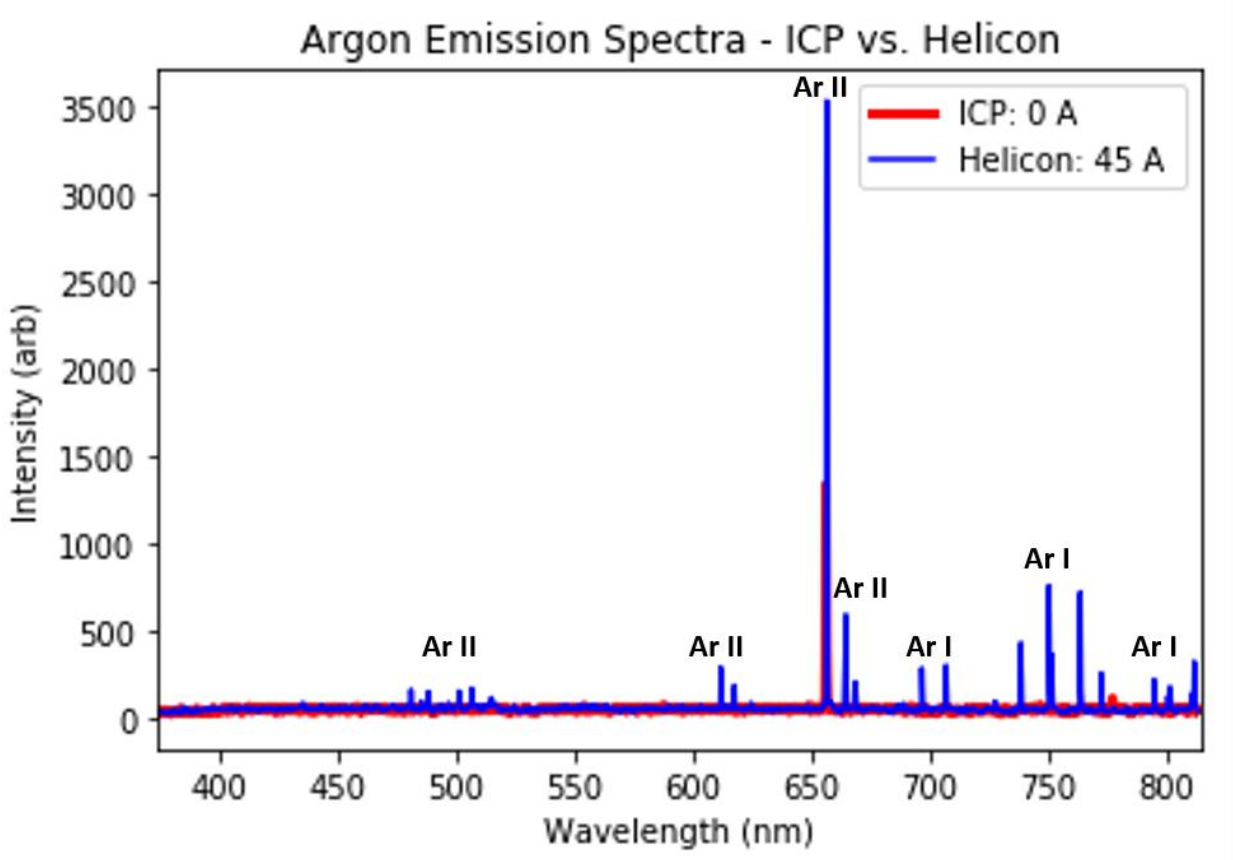

Figure 5.1: Comparison of Argon emission spectra for ICP and Helicon cases in the spectral range of 375 – 815 nm.

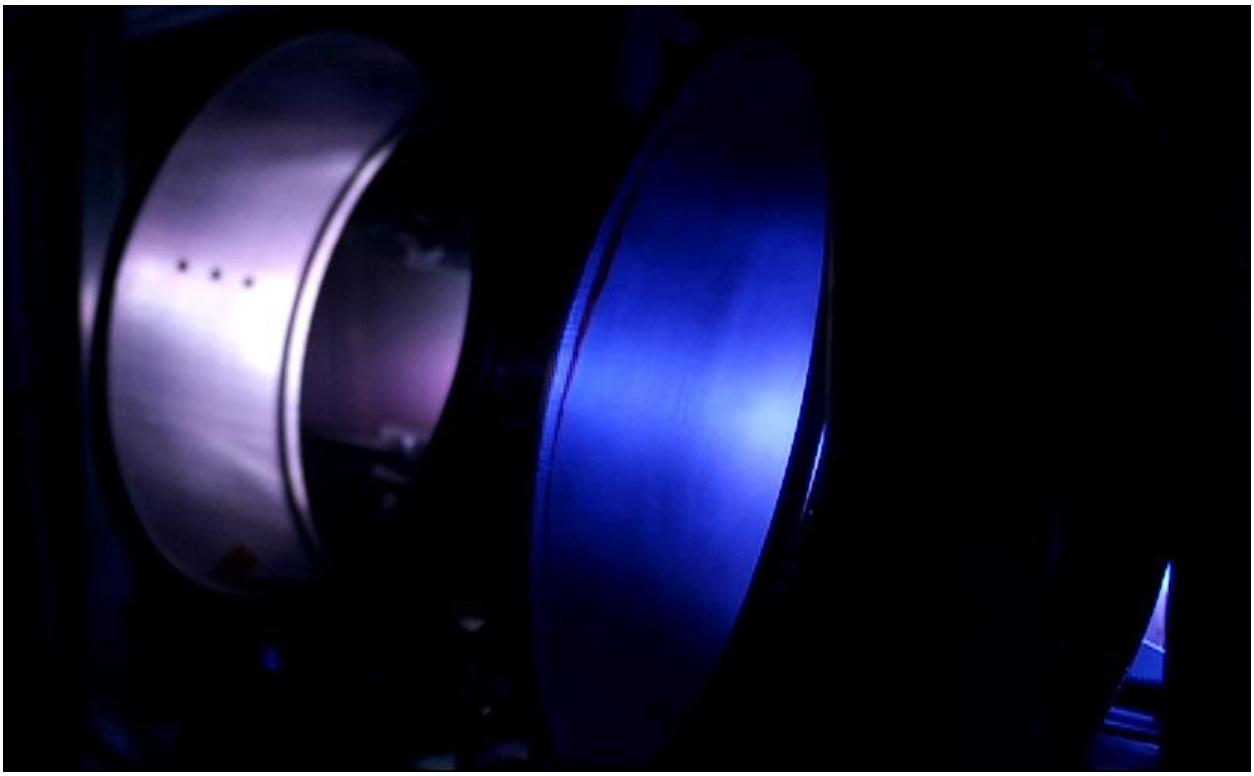

Figure 5.2: Initial plume visualization of the HPH cluster in the far flux conserving configuration

5.1 Variant 1: Far Flux Conserving Configuration

In a far flux conserving configuration (variant 1), the downstream 1st and 2nd magnetic nozzles were located at 9.8 cm and 45.8 cm respectively, from the Z = 0 source region. For this variant, density measurements were obtaining for left HPH, right HPH, and double HPH (clustered configuration) using the double Langmuir probe at an axial location of Z = 73.7 cm from the source region. Figure 5.3 shows the density trace for the left HPH thruster with base magnetic field and 1st magnetic nozzle active. The left HPH plasma density reaches a value close to $0.4\ x\ 10^{18}\ m^{-3}$ at $200\ \mu s$ before spiking to a secondary plasma density peak at $0.7\ x\ 10^{18}\ m^{-3}$ around $425\ \mu s$. Figure 5.4 shows the density trace for the right HPH thruster with base magnetic field and 1st magnetic nozzle active. The right HPH plasma density reaches a value close to $1.1\ x\ 10^{18}\ m^{-3}$ at

$200\ \mu s$ and sustains a flat-top density until $500\ \mu s$, where the density rapidly decays. The right HPH trace has a better signal-to-noise-ratio (SNR) and exhibited a uniform particle flux across probe tips for the $400\ \mu s$ interaction period; however, the left HPH has slightly more particle flux for the same interaction period. Figure 5.5 shows the density trace for double HPH thrusters with base magnetic field and 1st magnetic nozzle active. The double HPH plasma density peaked at a value of $2.7\ x\ 10^{18}\ m^{-3}$ around $350\ \mu s$, whereas the left HPH and right HPH peak plasma densities occurred around $400\ \mu s$, which could suggest acceleration of double HPH plasma particles downstream from the source for the same interaction period with the probe. Based on the peak density measurements for left HPH, right HPH, and double HPH, the double HPH contribution outperforms the sum of individual thruster contributions. The double HPH thruster has a peaked plasma density 50% higher than the sum of the left and right HPH peaked plasma densities. A time-of-flight probe is needed to estimate exit velocities and determine the peak ion flux when operating double HPH thrusters simultaneously.

Furthermore, there were significant issues with electromagnetic interference which led to the deterioration of key thruster sub-systems, limiting the number of diagnostics incorporated into this 1st data collection campaign. Even without additional diagnostics, the double Langmuir probe data provided enough quantitative information on the thruster plasma density to continually improve the HPH cluster experiment.

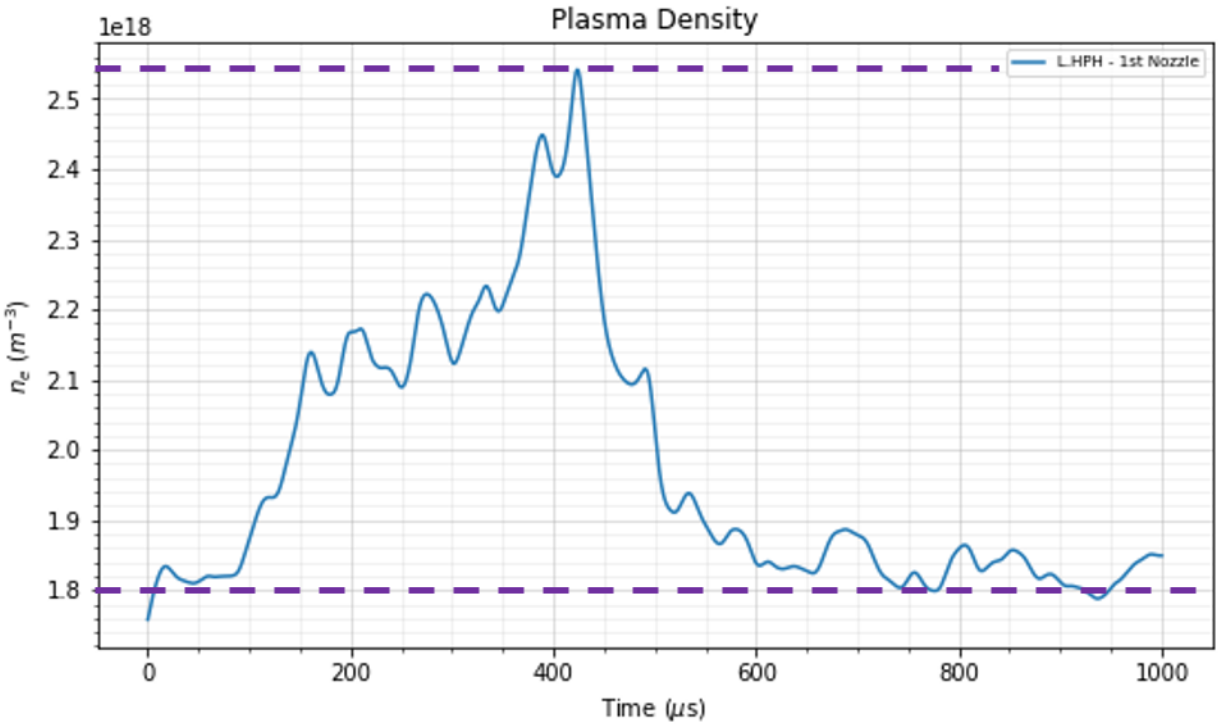

Figure 5.3: Density measurement of left HPH thruster with the base magnetic field and 1st magnetic nozzle active. Adjusting for a floor of $1.8\ x\ 10^{18}\ m^{-3}$, the peak plasma density for the left HPH thruster is $0.7\ x\ 10^{18}\ m^{-3}$.

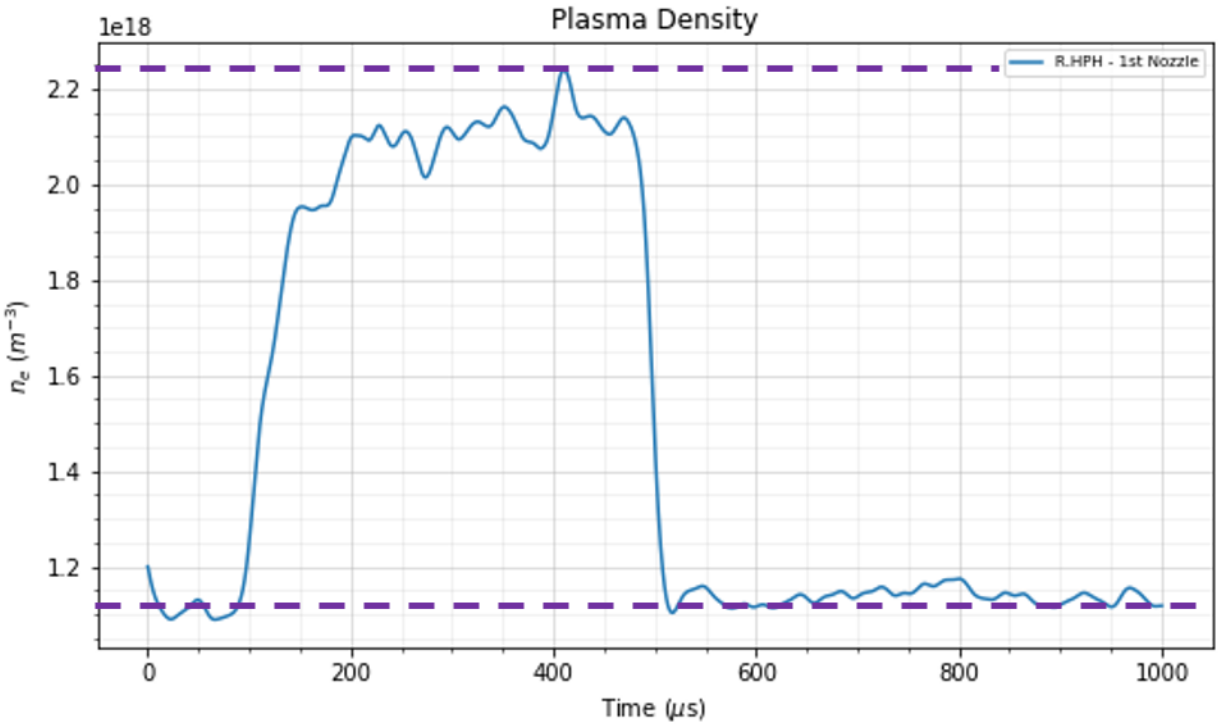

Figure 5.4: Density measurement of right HPH thruster with the base magnetic field and 1st magnetic nozzle active. Adjusting for a floor of $1.1\ x\ 10^{18}\ m^{-3}$, the peak plasma density for the right HPH thruster is $1.1\ x\ 10^{18}\ m^{-3}$.

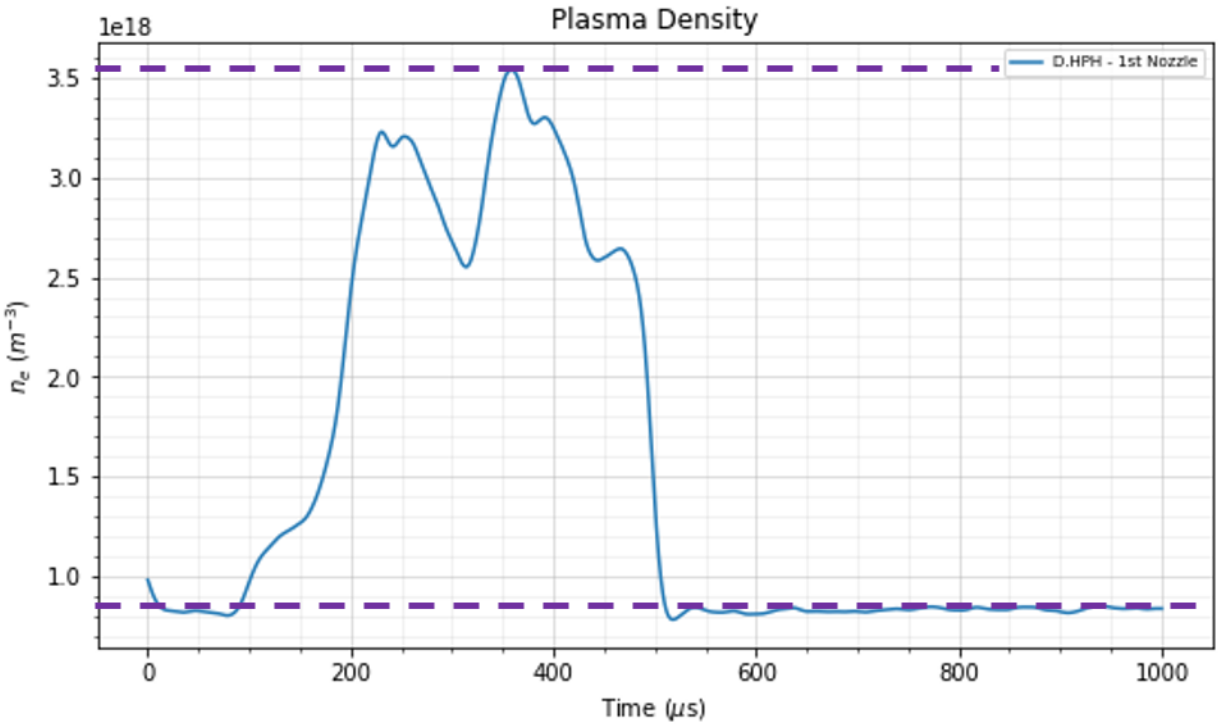

Figure 5.5: Density measurement of double HPH thrusters with the base magnetic field and 1st magnetic nozzle active. Adjusting for a floor of $0.8\ x\ 10^{18}\ m^{-3}$, the peak plasma density for the left HPH thruster is $2.7\ x\ 10^{18}\ m^{-3}$.

5.2 Variant 2: Close Flux Conserving Configuration

Since there was a increase in plasma density when operating both thrusters in the far flux conserving configuration, a close flux conserving configuration was chosen as the next logical step to potentially enhance thruster performance. A suite of additional diagnostics, i.e. RF-DLP, RPA, nude Faraday probe, were integrated into the vacuum facility to complement DLP and TOF diagnostics in better predicting downstream plume properties. In the close flux conserving configuration (variant 2), the downstream 1st and 2nd magnetic nozzles were located at 9.8 cm and 33.8 cm respectively, from the Z = 0 source region. Table 5.2 includes a list of probe diagnostics

and their respective axial locations from the Z = 0 source region. All diagnostic measurements are taken at the thruster centerline, R = 0, unless stated otherwise.

Table 5.2: Probe diagnostics at their respective axial locations from the Z = 0 source region in the variant 2-close flux conserving configuration

Probe Diagnostic	Downstream Axial Location from Z = 0 Source Region
Nude Faraday Probe (NFP)	Z = 54.4 cm
RF-compensated Double Langmuir Probe (RF-DLP)	Z = 60.2 cm
Double Langmuir Probe, DLP #1	Z = 73.7 cm
Double Langmuir Probe, DLP #2	Z = 133.7 cm
Retarding Potential Analyzer (RPA)	Z = 136.5 cm
Double Langmuir Probe, DLP #3	Z = 139.2 cm
Time-of-Flight (TOF) Probe	DLP#2 @ Z = 133.7 cm; DLP#3 @ Z = 139.2 cm; $\Delta z = 5.5\ cm$

The first set of diagnostic measurements in the close flux conserving configuration were the double Langmuir probe, DLP#1, at an axial location of Z = 73.7 cm away from the source region. Figure 5.6 shows plasma density traces of the left HPH thruster in its three operation modes. As more magnetic nozzles are activated, there is a noticeable increase in the peak plasma density but also the total particle flux, suggesting improvement of beam collimation. Moreover, the peak of the emissions seems to occur earlier in time, suggesting a faster flowing plasma as beam collimation improves. The peak plasma density for the left HPH thruster with all magnetic nozzles active corresponded to $0.8\ x\ 10^{18}\ m^{-3}$. Figure 5.7 shows plasma density traces of the right HPH thruster in its three operation modes. The right HPH thruster exhibits a similar increase in plasma density, with a faster rise time, as additional magnetic nozzles are activated. For each operation mode of the right HPH thruster, the plasma density reached a peak value and sustained

a flat-top density for the total interaction period with DLP#1. The peak plasma density for the right HPH thruster with all magnetic nozzles active corresponded to $1.5\ x\ 10^{18}\ m^{-3}$, a 29% increase in plasma density in comparison to the left HPH thruster with similar magnet settings. Figure 5.8 shows plasma density traces of double HPH thrusters in its three operation modes. Initially, the density trace with the base magnetic field exhibited a flat-top profile, with a slight increase in plasma density at $450\ \mu s$. As additional magnetic nozzles are activated, the plasma density increase at $450\ \mu s$ becomes more pronounced, with a maximum of $5.0\ x\ 10^{18}\ m^{-3}$ when all magnetic nozzles are activated. Similarly, double HPH exhibited a faster rise time of the density trace as additional magnetic nozzles are activated, suggesting a better conversion of thermal energy to directed ion energy, which could suggest higher exit velocities. Based on the peak density measurements for left HPH, right HPH, and double HPH, the double HPH contribution outperforms the sum of individual thruster contributions. The double HPH thruster has a peaked plasma density 117% higher than the sum of the left and right HPH peaked plasma densities. It should also be noted that there is a 22% increase in double HPH plasma density from variant 1 condition to variant 2 condition with the 1st magnetic nozzles active. Overall, variant 2-close flux condition has a ~85% increase in the double HPH peak plasma density in comparison to the results in the variant 1-far flux condition.

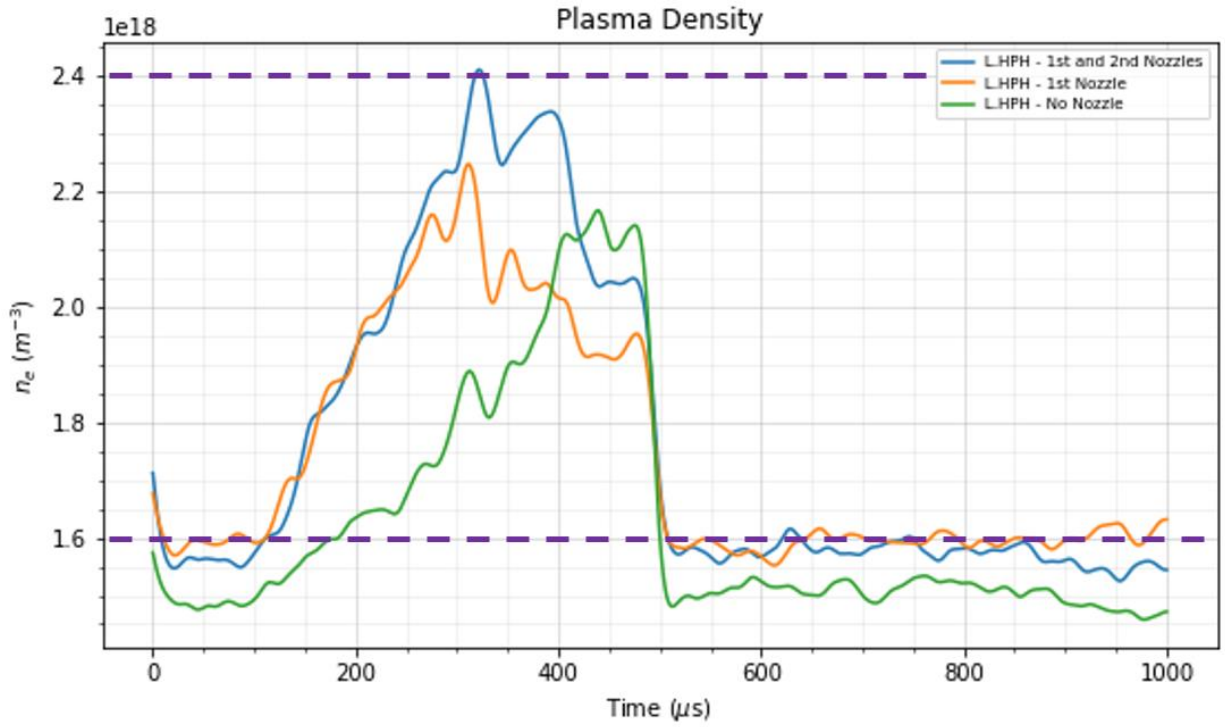

Figure 5.6: Density measurements of left HPH with the activation of the base magnetic field, 1st magnetic nozzle, and the 2nd magnetic nozzle. Adjusting for a floor of 1.6×10^{18} m^{-3}, the peak plasma density for the left HPH thruster with all magnetic nozzles active is 0.8×10^{18} m^{-3}.

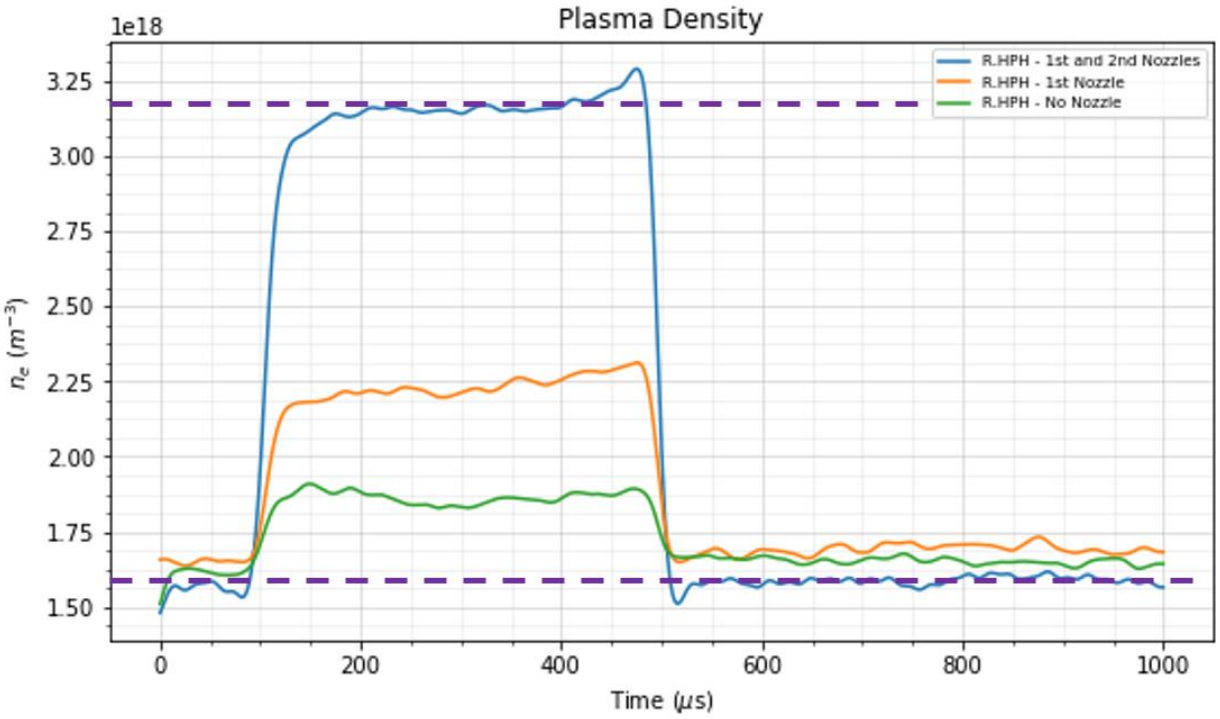

Figure 5.7: Density measurements of the right HPH with the activation of the base magnetic field, 1st magnetic nozzle, and the 2nd magnetic nozzle. Adjusting for a floor of 1.6 x 10^{18} m^{-3}, the peak plasma density for the right HPH thruster with all magnetic nozzles active is 1.5 x 10^{18} m^{-3}.

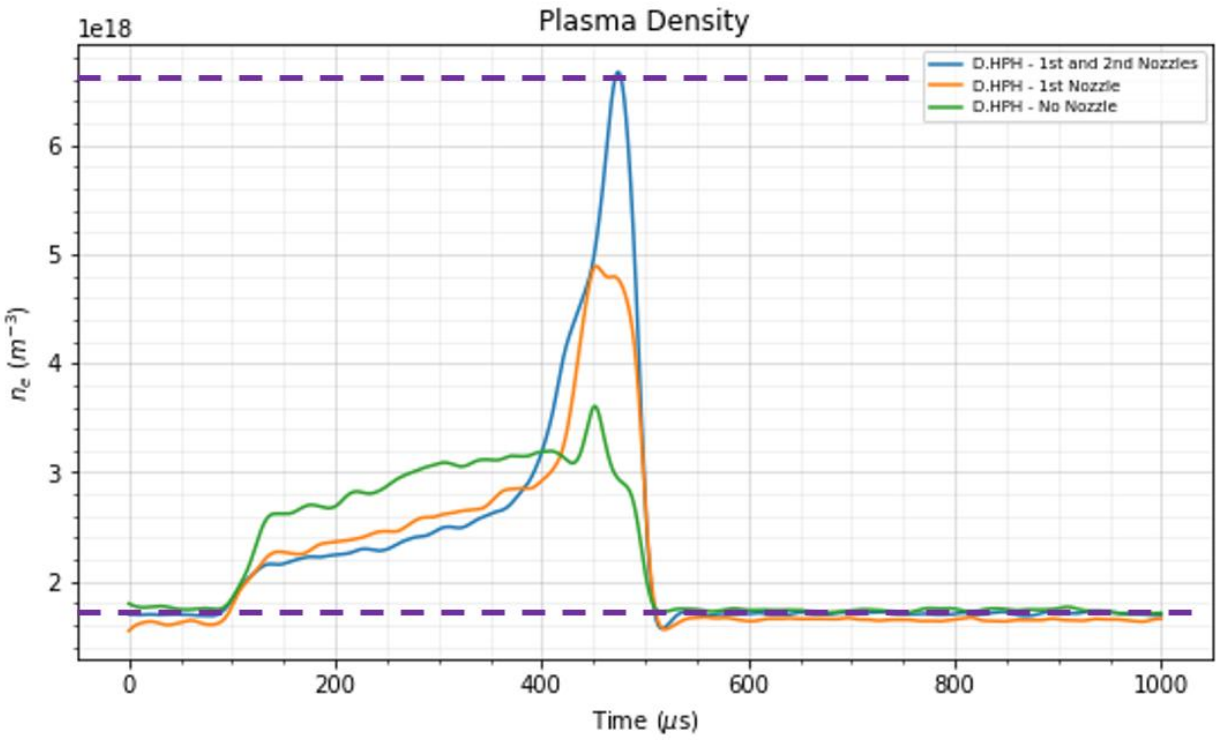

Figure 5.8: Density measurements of double HPH thrusters with the activation of the base magnetic field, 1st magnetic nozzle, and the 2nd magnetic nozzle. Adjusting for a floor of 1.6 x 10^{18} m^{-3}, the peak plasma density for the double HPH thruster with all magnetic nozzles active is 5.0 x 10^{18} m^{-3}.

The second set of diagnostic measurements used in the close flux conserving configuration were the time-of-flight (TOF) probe. The TOF probe used two adjacent DLPs far from the source region, DLP#2 at an axial location of Z = 133.7 cm and DLP#3 at an axial location of Z = 139.2 cm, to estimate the average ion velocity of thruster plumes. The two DLPs have a separation distance of 5.5 cm, 13.6 cm, 60 cm, or 73.5 cm between the probe tips and are biased at -65 V. The estimated average ion velocity can be determined as:

$$v_i = \frac{\Delta z}{\Delta t} \tag{5.1}$$

where Δz is the axial separation distance and Δt is the plasma time of flight between adjacent probe tips. For time-of-flight measurements, the left HPH, right HPH, and double HPH thrusters are operated with all magnetic nozzles activated. Table 5.3 provides the time of flight and estimated ion velocities for left HPH, right HPH, and double HPH. The estimated ion velocities for left HPH and right HPH are close to 11 km/s. Based on the estimated ion velocities for the left HPH and double HPH, there is almost a 50% increase in exit velocity when operating a cluster of HPH thrusters instead of a single thruster. Figure 5.9 shows characteristic double HPH density traces for probes 1 and 2 to determine the time of flight. The density for the 1st Langmuir probe in the time of flight should be higher than the 2nd Langmuir probe as it is closer to the Z = 0 source region, although probe alignment inaccuracies has been shown to influence the measured signal. By using the peak-to-peak current technique, the time of flight is found as $3\ \mu s$. As a result, the estimated average ion velocity is 18.3 km/s for the double HPH thruster. By determining the plasma density and ion velocity at thruster centerline, the peak ion flux can be calculated. The ion flux is defined as the product of the plasma density multiplied by the ion velocity. Table 5.4 provides the peak ion flux calculations. Based on the estimated ion flux values for left HPH, right HPH, and double HPH, the double HPH contribution outperforms the sum of individual thruster contributions. The double HPH thruster has a peak ion flux 256% higher than the sum of the left and right HPH peak ion fluxes.

Table 5.3: Time of flight probe measurements for the close flux conserving configuration

Time of Flight Probe Measurements		
Thruster Mode	**Time of Flight, Δt**	**Estimated Ion Velocity, v_i**
Left HPH	$4.8\mu s$	11.5 ± 0.8 km/s
Right HPH	$5.0\mu s$	11.0 ± 0.7 km/s
Double HPH	$3.0\mu s$	18.3 ± 1.3 km/s

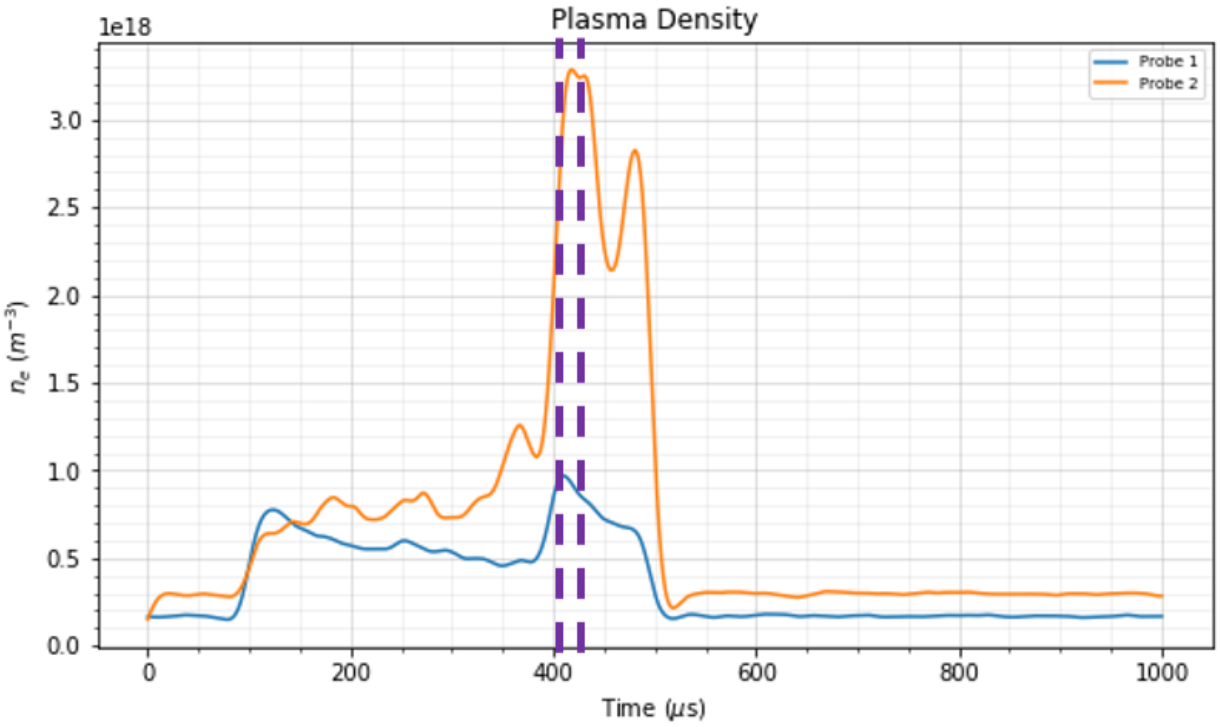

Figure 5.9: Using a peak-to-peak current technique between probe traces, a time of flight of 3 μs is determined, corresponding to an estimated ion velocity of 18.3 km/s for double HPH thruster.

Table 5.4: Peak Ion Flux Calculations for the Variant 2 Close Flux Conserving Configuration

Ion Fluxes Calculations			
Thruster Mode	**Plasma Density, n_i**	**Estimated Ion Velocity, v_i**	**Peak Ion Flux, <nv>**
Left HPH	$0.8\ x\ 10^{18}\ m^{-3}$	11.5±0.8 km/s	$0.92\ x\ 10^{22}\ m^{-2}s^{-1}$
Right HPH	$1.5\ x\ 10^{18}\ m^{-3}$	11.0±0.7 km/s	$1.65\ x\ 10^{22}\ m^{-2}\ s^{-1}$
Double HPH	$5.0\ x\ 10^{18}\ m^{-3}$	18.3±1.3 km/s	$\mathbf{9.15\ x\ 10^{22}\ m^{-2}s^{-1}}$

With left HPH and right HPH thrusters yielding similar plasma densities and exit velocities, additional test measurements in the close flux conserving configuration focused on single thruster operation and double thruster operation with all magnetic nozzles active. Radial density profiles were determined using DLPs located at an axial location of Z = 60.2 cm from the Z = 0 source region. Radial sweeps of ±20 cm away from the thruster centerline were performed for single and double thruster operations. Figure 5.10 shows the radial density profile of the single thruster (left HPH) operation. The plasma density of 0.5 x 10^{18} m^{-3}, is peaked at the thruster centerline (R = 0) and monotonically decreases 5 cm away from the centerline; however, the profile exhibited an inconsistent trend in density decay as the probe is translated further away from the centerline. A non-linear fit is applied to fit the experimental data. Based on the fit, the full-width at half maximum (FWHM) can be considered as an approximation of the beam width. The FWHM is determined to be 25 cm or 1.09 large magnet radii. Figure 5.11 shows the radial density profile of the double HPH thruster operation. The plasma density of 6.2 x 10^{18} m^{-3} is peaked on-axis and exhibited a monotonically decrease in density as the probe translates toward -20 cm i.e. left radial extent. As the probe translates toward +20 cm i.e. right radial extent, the density seems to follow a monotonically decreasing density except for the +15 cm radial position where the density is higher than the on-axis density. The +15 cm radial position could be an outlier in the experimental

data due to anomalous edge effects that introduce electromagnetic interference which adversely affects the signal response. A non-linear fit is applied to the experimental data. The FWHM is determined to be ~35 cm or 1.52 large magnet radii. The double HPH operation has a 39.4% increase in the approximate beam width in comparison to the single HPH operation.

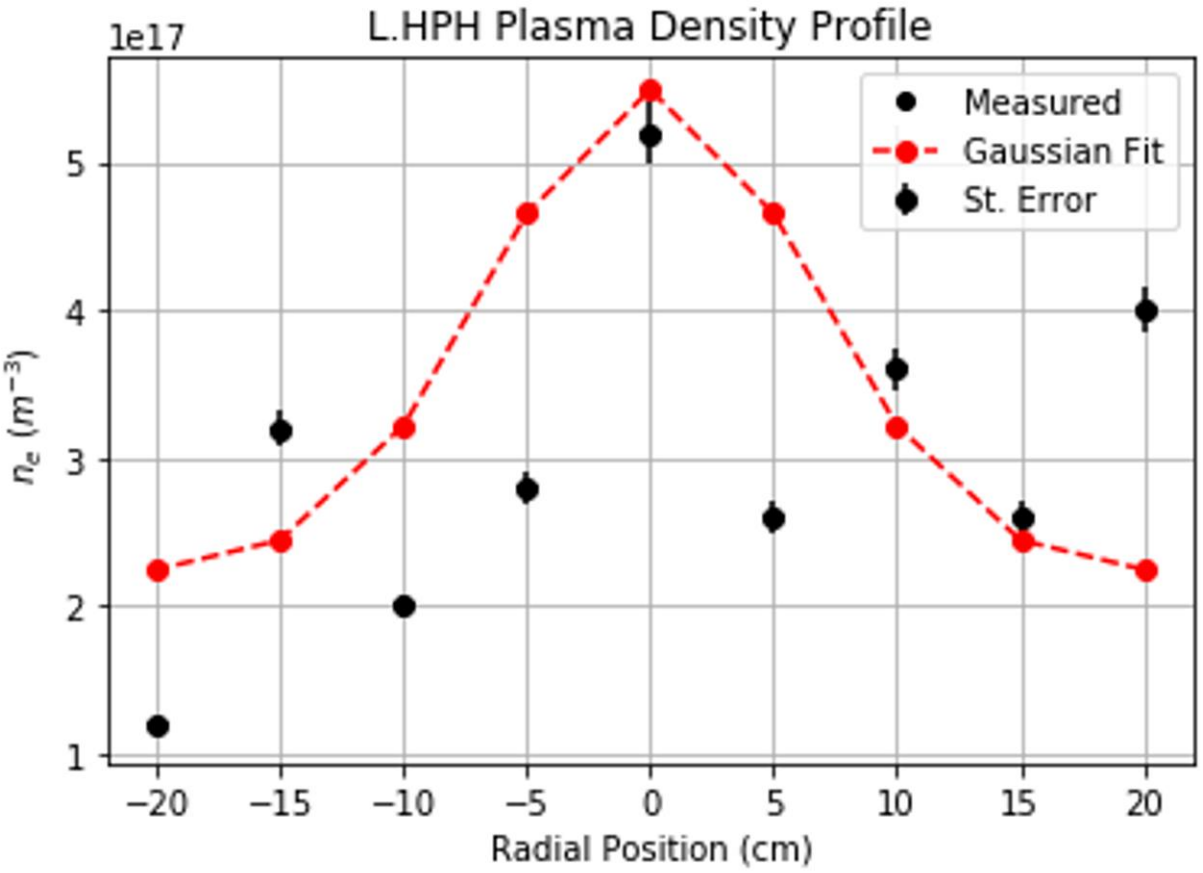

Figure 5.10: Radial density profile of the single thruster (left HPH) operation, with all magnetic nozzles active. The FWHM is determined to be ~25 cm or 1.09 large magnet radii.

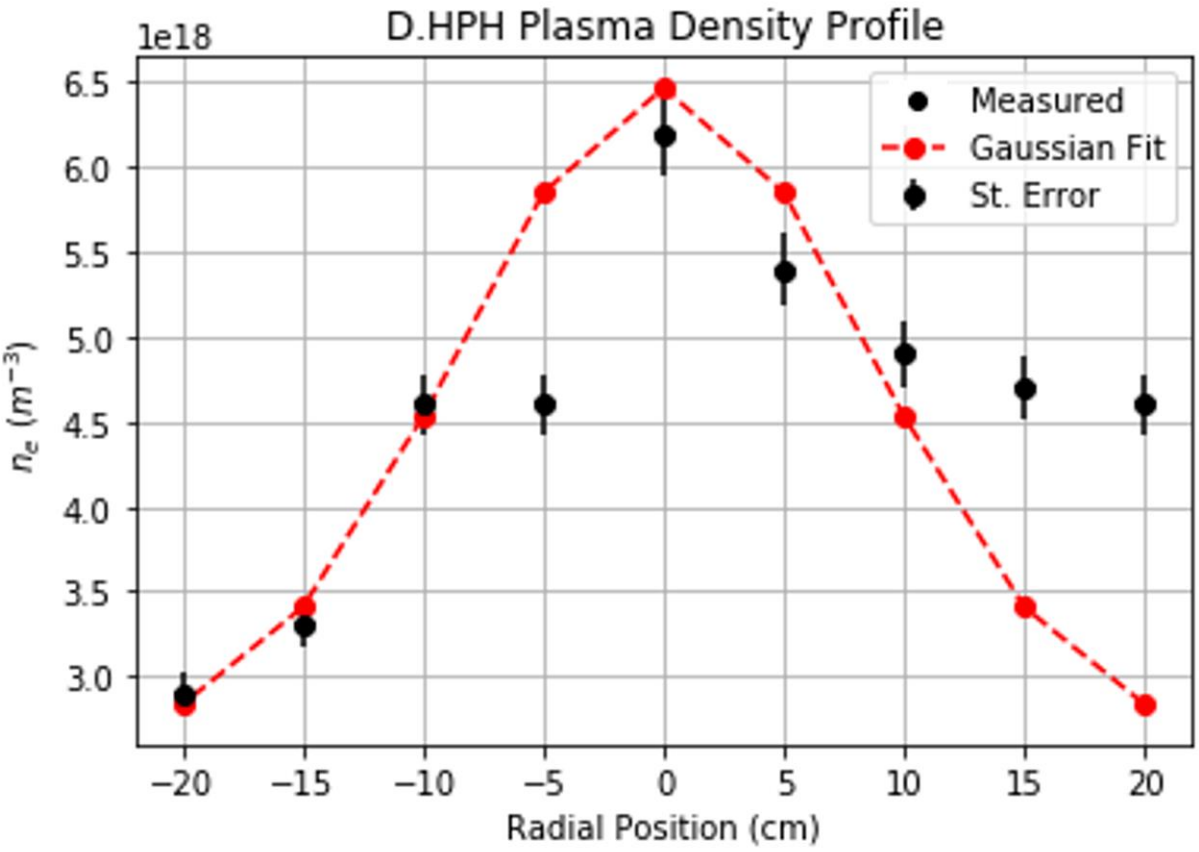

Figure 5.11: Radial density profile of the double thruster operation, with all magnetic nozzles active. The FWHM is determined to be ~35 cm or 1.52 large magnet radii.

The third set of diagnostic measurements used in the close flux conserving configuration was the nude Faraday probe (NFP). The NFP is an ion beam diagnostic useful in providing the ion current density of the clustered HPH plumes at Z = 54.4 cm from the source region. The NFP is biased at -30 V potential to operate in ion saturation regime. Figure 5.12 provides the on-axis ion current density for a single (left HPH) thruster operation. In the figure below, there is an initial spike up to 266 A/m^2, followed by a rapid decay down to a sustained 200 A/m^2 current density for the bulk of the 200 μs plasma interaction period with the NFP. For double thruster operation, a typical ion current density trace on-axis is displayed in Figure 5.13. There is an initial spike up

to a current density of 555 A/m^2 for about 25 μs followed by a steep drop off down to 200 A/m^2 for about 50 μs before a secondary peak back up to 325 A/m^2. Performing several shot-to-shot repeatability studies and averaging the data sets, there seems to be a two-fold increase in the ion current density for the double thruster operation in comparison to the single thruster operation. Based on the measured double thruster data, there seems to be a factor of two reduction in double thruster plume interactions with the NFP, while exhibiting a two-fold increase in the ion current density. The shorter interaction period suggests higher exit velocity plasma plumes, while higher current density suggest improved coupling of independent plasma streams. A radial current density profile can better account for the beam diameter and divergence. A $\pm$20 cm radial current density profile for double thruster operation is shown in Figure 5.14. The ion current density is peaked on-axis but has a very gradual drop off. A full-width at half maximum (FWHM) can be used to approximate the beam width for variant 2-close flux configuration. Based on the variant 2 double HPH current density profile, the FWHM is approximately 37.5 cm or 1.6 large magnet radii.

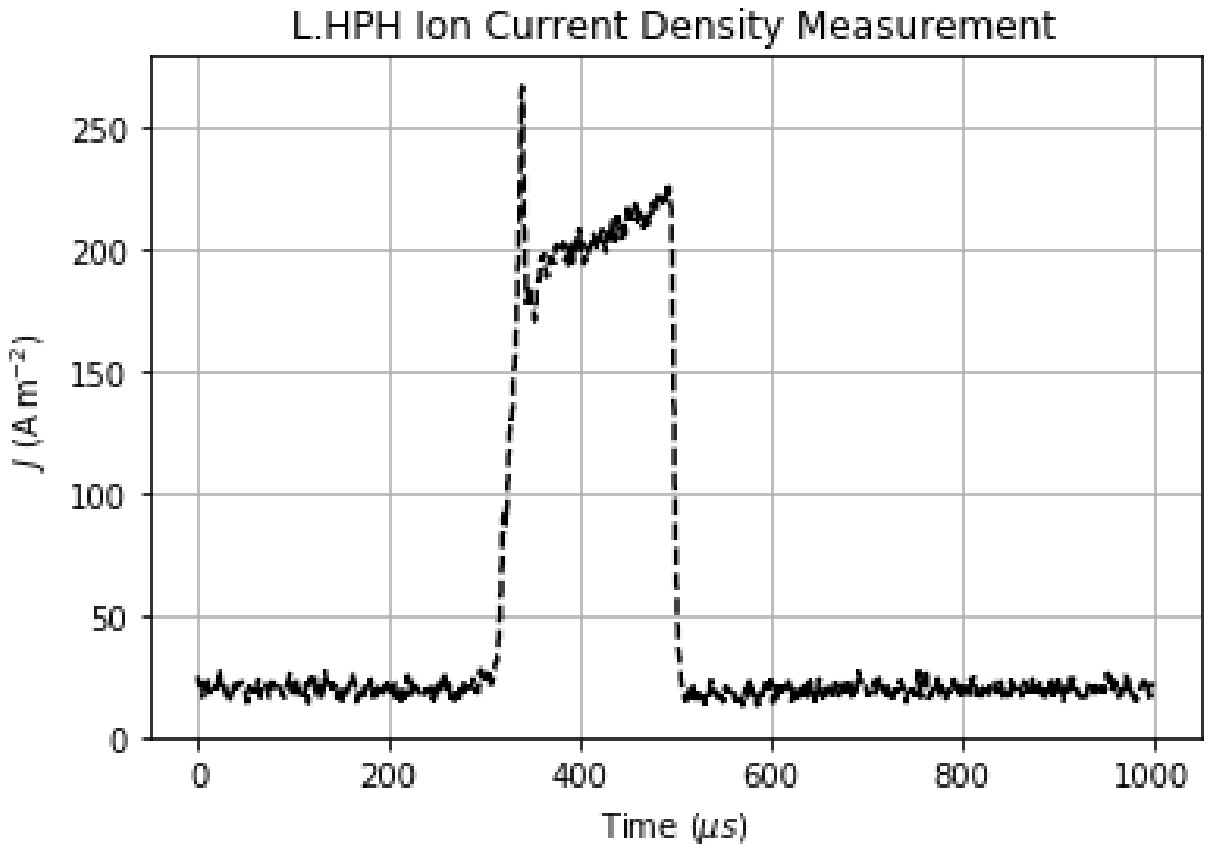

Figure 5.12: On-axis ion current density of the single (left HPH) thruster operation, with the activation of the base magnetic field, 1st magnetic nozzle, and 2nd magnetic nozzle.

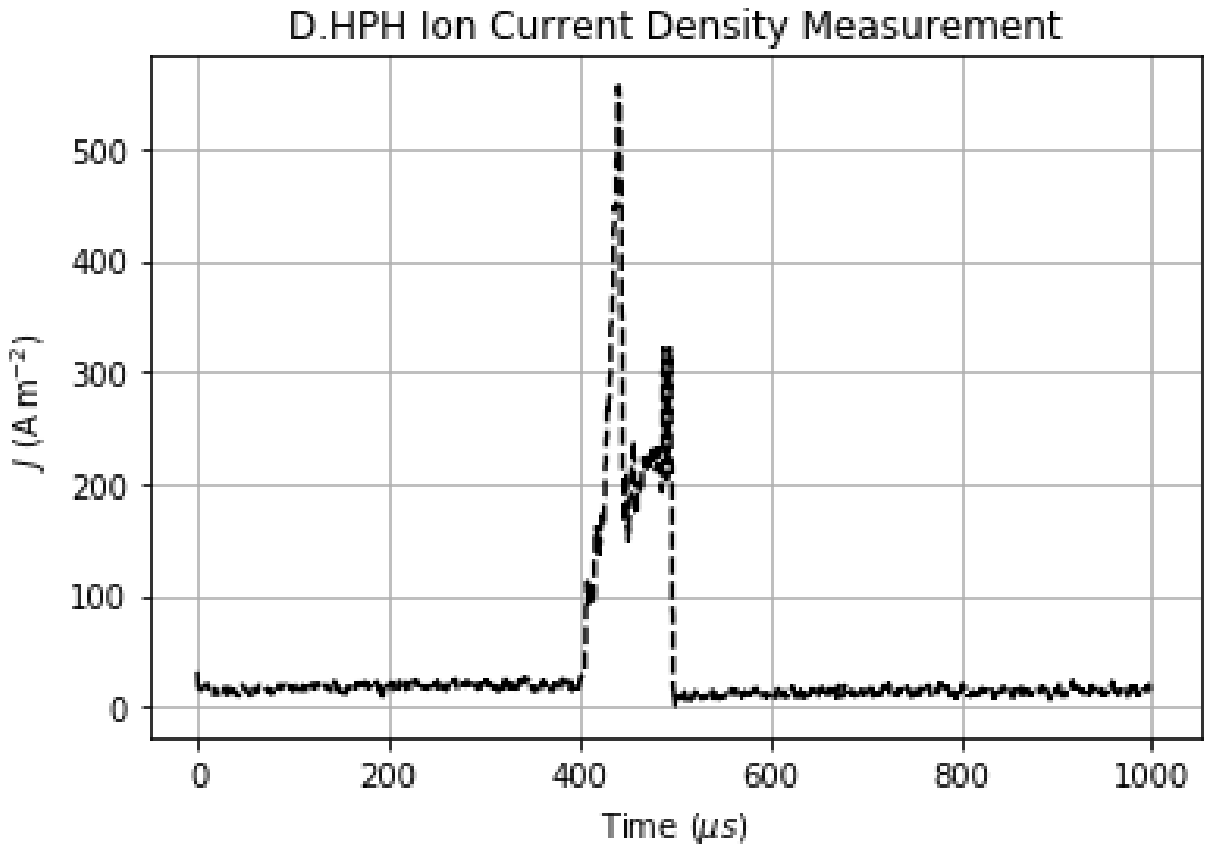

Figure 5.13: On-axis ion current density of the double thruster operation, with the activation of the base magnetic field, 1st magnetic nozzle, and 2nd magnetic nozzle.

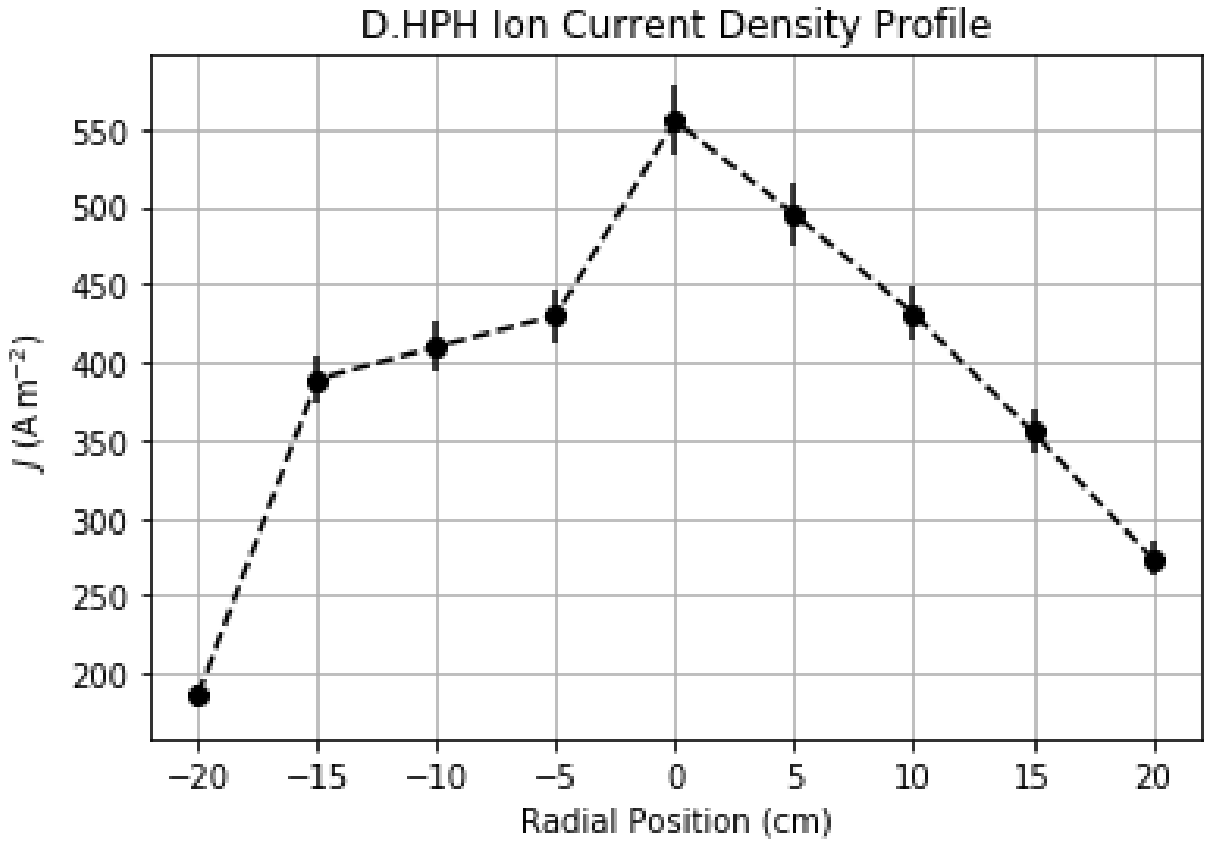

Figure 5.14: Radial ion current density profile of the double thruster operation, with all magnetic nozzles active. Current density is peaked on-axis at 550 A/m^2.

The fourth set of diagnostic measurements used in the close flux conserving configuration was the RF-DLP. The RF-compensated double Langmuir probes are commonly used in helicon plasma sources to compensate for the oscillating plasma potential oscillations and better predict the electron temperature. A current-voltage (I-V) curve has been created to estimate the electron temperature for clustered (double) HPH plumes as seen in Figure 5.15. A double probe recipe is used to identify the ion saturation current, saturation voltage, and estimate the electron temperature [Ref. 63-66]. Based on the regression fits at ion saturation, electron retarding, and electron

saturation regimes, the ion saturation current is 8 mA, saturation voltage is 20 V, and the electron temperature is determined to be ~10 eV.

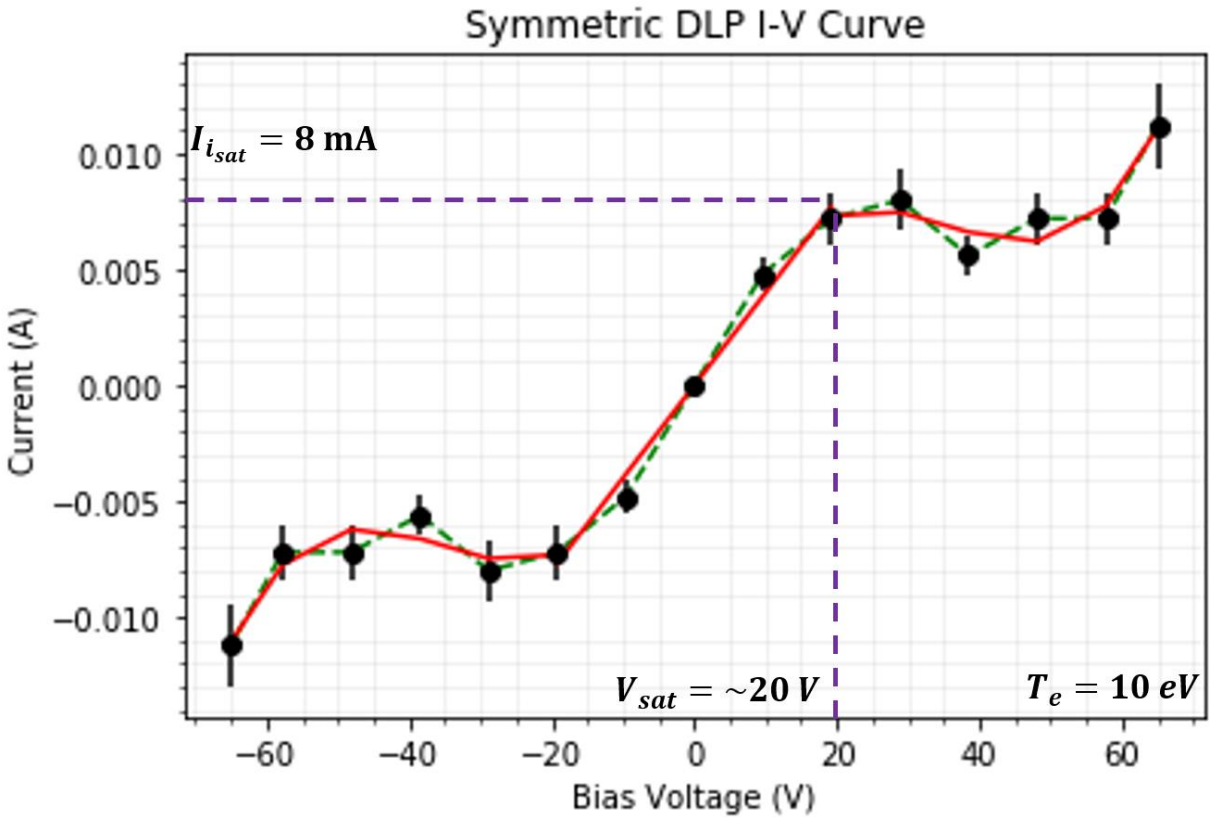

Figure 5.15: Estimation of electron temperature of the clustered HPH plumes using the RF-DLP diagnostic at thruster centerline (R = 0). Standard double HPH operational settings with all magnetic nozzles active.

The fifth set of diagnostic measurements used in the close flux conserving configuration was the retarding potential analyzer (RPA). The RPA is an ion beam diagnostic used to determine the ion velocity distribution function of the clustered HPH plumes at Z = 136.5 cm from the source region. For this research, several attempts were made to reliably determine the most probable ion

energies and ion velocities using the RPA diagnostic at these far axial locations. A typical RPA current trace is shown in Figure 5.16. As can be seen, the data has small current signals. With low signal to noise ratio, an additional amplifier circuit is needed or re-location to diagnostic ports closer to the source region. As such, the RPA will not be included further in the analysis of this current research but will be discussed in the future recommendations section.

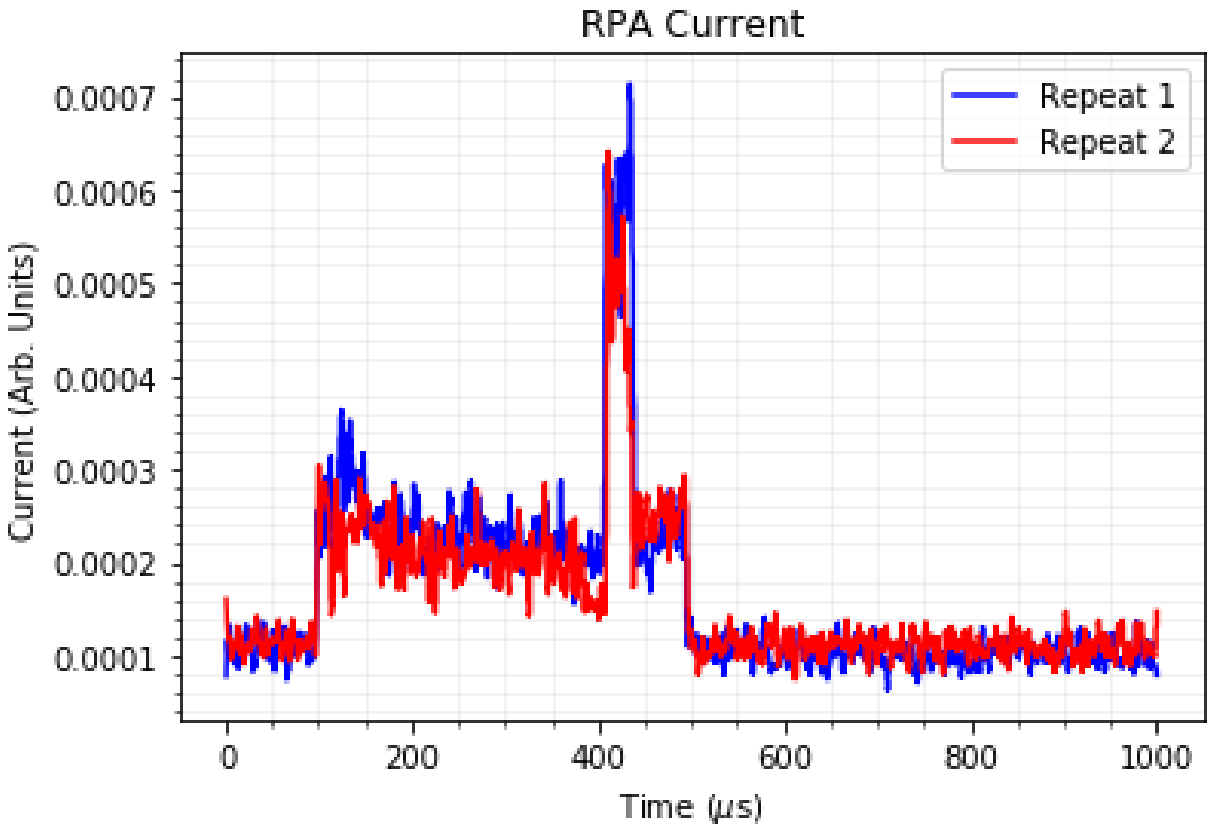

Figure 5.16: Typical RPA current trace for the double thruster operation, with the activation of the base magnetic field, 1st magnetic nozzle, and 2nd magnetic nozzle. The RPA diagnostic is located at Z = 136.5 cm away from the source region.

In the 2nd data collection campaign, the variant 2-close flux conditions were implemented with additional diagnostics measuring plume properties of the cluster of HPH thrusters. Many of

the diagnostics in variant 2-close flux condition were taken at the thruster centerline (R = 0). As such, key plasma parameters of plasma density, electron temperature, exit velocity, and ion current density have been measured for clustered HPH plumes. Radial profiles of plasma density and ion current density in the $\pm$20 cm radial extent exhibited non-Maxwellian features. Due to the orientation and pitch of the helicon thrusters, there could be asymmetrical plasma plume evolution to account for very large beam angles. Several attempts were made to determine the time-of-flight (v_i) and ion flux $< nv >$ profiles but was unable to obtain reliable measurements due to low signal to noise ratio in the downstream axial DLP locations. Figure 5.17 shows the signal response for two DLPs, a close DLP and a far DLP, separated 73.5 cm axially. The shot-to-shot repeatability studies highlights that it is straightforward to perform radial sweeps of close DLP datasets. As you move further away from the source, constrained in part by the availability of wall-mounted probes, performing radial sweeps on far DLPs become difficult as low signal-to-noise ratio influences the Langmuir signal response. With stated research goals of high beam collimation and exit velocities, further optimization efforts are needed to minimize beam spreading. The 3rd data collection campaign attempted to further optimize thruster performance in terms of beam collimation and high exit velocities while achieving a low divergence angle. The details are discussed in the next section.

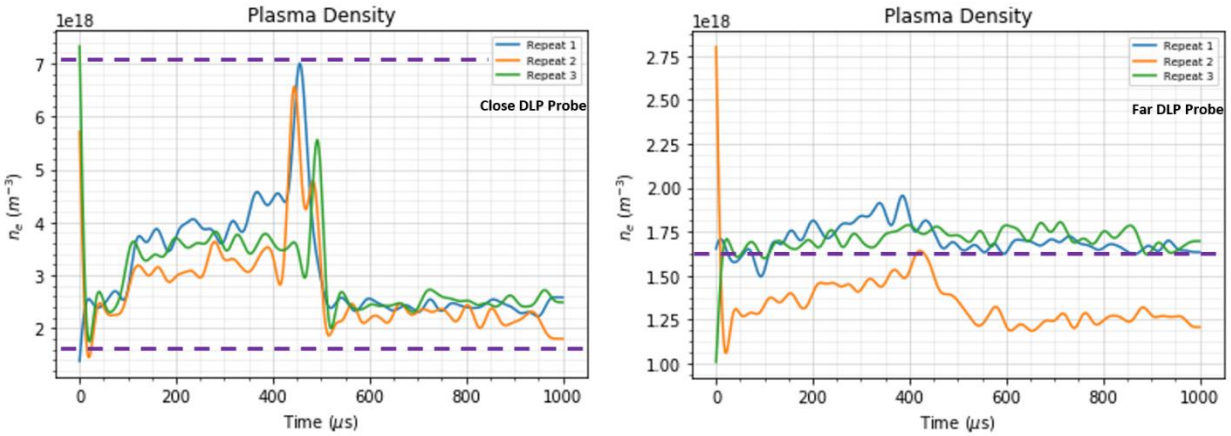

Figure 5.17: Low signal-to-noise ratio influences the Langmuir signal at far axial locations. Determination of time-of-flight and ion flux profiles become difficult due to signal dependency.

Chapter 6. Improved Cluster Thruster Configuration and Performance

The thruster architecture of the HPH cluster experiment has been updated to mitigate any potential plume asymmetries present in the initial architectural design. The newest architecture has the two HPH thrusters oriented 12.7 degree off-parallel yaw angle and 0.0 degree pitch angle. The thruster units, include the base magnets and 1st magnetic nozzles, have been placed on I-beams to elevate their thruster centerlines to be coincident with the centerline of the 2nd magnetic nozzle. In addition, the base magnets and 1st magnetic nozzles have been translated 5.5 cm forward toward the 2nd magnetic nozzles. A third magnetic nozzle configuration (variant 3) can be defined as the 1st nozzle and 2nd nozzle located 9.8 cm and 28.3 cm downstream of the Z = 0 source region. The amperage values for the base magnetic field, 1st magnetic nozzle, and 2nd magnetic nozzle are 45 A, 25 A, and 20 A respectively, unless stated otherwise. Figure 6.1 shows the newest experimental setup without pitch angle and coincident with 2nd magnetic nozzle's centerline axis. Initial plume visualization of clustered HPH plumes in the variant 3-flux conserving condition using the Edgertronic camera is shown in Figure 6.2. In the image, the left HPH thruster exhibited the characteristic blue core discharge, while the right HPH thruster exhibited a white-reddish discharge. These differences may be attributed to slight variability in the inductances of the RF-PPUs or neutral density buildup in the respective thruster units. For the 3rd data collection campaign, the variant 3-flux conserving configuration is tested with DLPs, TOF, NFP, and RF-DLP diagnostics to characterize the downstream clustered plume properties. The intrusive probe diagnostics were located 5.5 cm closer to the Z = 0 source region. Table 6.1 includes a list of probe diagnostics and their respective axial locations from the Z = 0 source region. All diagnostic measurements are taken at the thruster centerline, R = 0, unless stated otherwise.

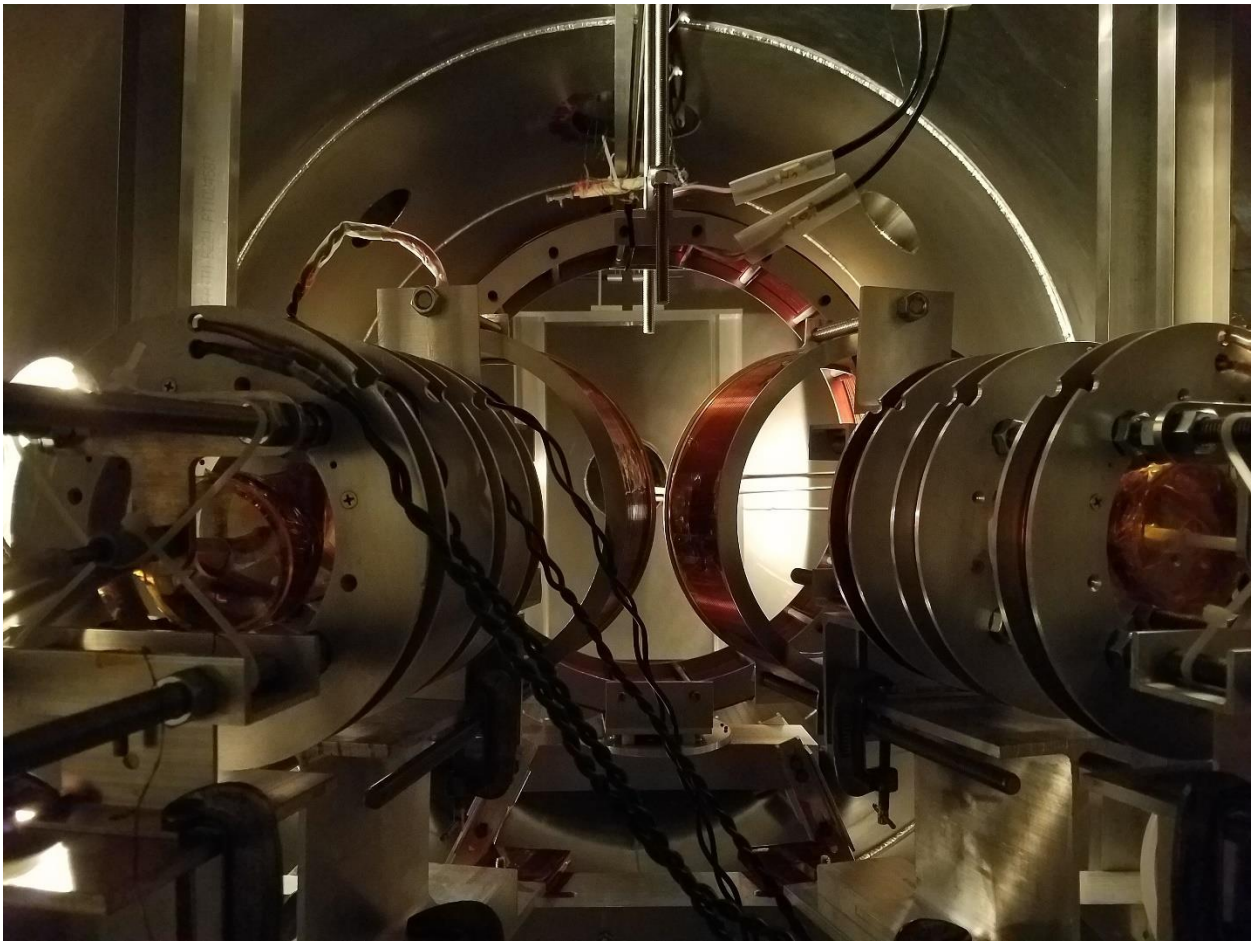

Figure 6.1: Newest thruster architecture, 12.7 degree off-parallel yaw angle and 0.0 degree pitch angle. Thruster units have been elevated using I-beams to align their centerlines with the 2nd magnetic nozzle's centerline axis.

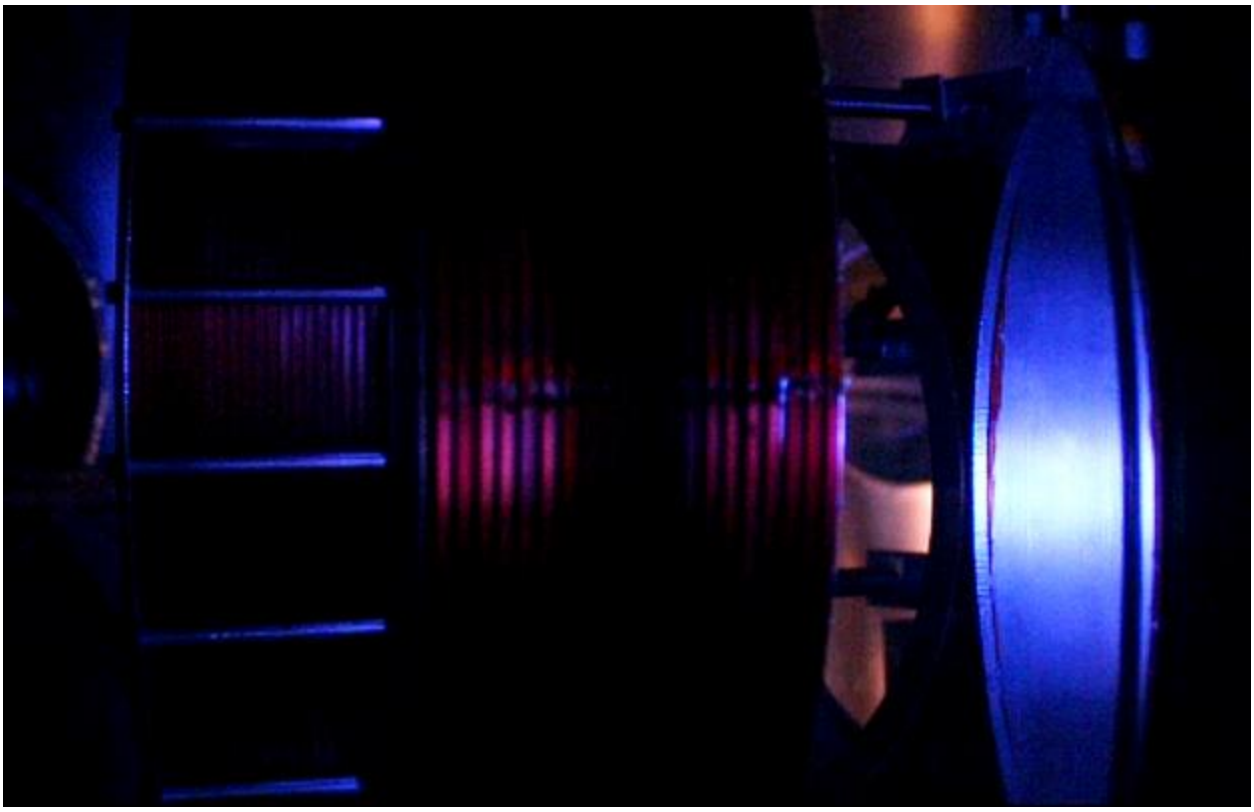

Figure 6.2: Initial plume visualization of the HPH cluster in the variant 3-magnetic flux conserving configuration.

Table 6.1: Probe diagnostics at their respective axial locations from the Z = 0 source region in the variant 3-flux conserving configuration

Probe Diagnostic	**Downstream Axial Location from Z = 0 Source Region**
Nude Faraday Probe (NFP)	Z = 48.9 cm
RF-compensated Double Langmuir Probe (RF-DLP)	Z = 54.7 cm
Double Langmuir Probe, DLP #1	Z = 68.2 cm
Double Langmuir Probe, DLP #2	Z = 128.2 cm
Retarding Potential Analyzer (RPA)	Z = 131 cm
Double Langmuir Probe, DLP #3	Z = 133.7 cm
Time-of-Flight (TOF) Probe	Far TOF Probe i.e. DLP#2 @ Z = 128.2 cm; DLP#3 @ Z = 133.7 cm; $\Delta z = 5.5\ cm$

The first set of diagnostic measurements in the variant 3-flux conserving configuration used the RF-DLP to measure the plasma density. The RF-DLP was located at an axial location of Z = 54.7 cm away from the source region. Density measurements for different thruster modes of operation, with all magnetic nozzles acitve were shown in Figure 6.3. In the figure, left HPH and right HPH thrusters have fairly uniform flat-top profiles for the 400 μs interaction period. The double HPH has fairly uniform plasma density for the first 300 μs and rises toward a peak value in the last 100 μs of the interaction period. Adjusting for a floor of 2.2×10^{18} m^{-3}, the peak plasma density for left HPH, right HPH, and double HPH thruster with all magnetic nozzles active is 3.2×10^{18} m^{-3}, 1.8×10^{18} m^{-3}, and 7.4×10^{18} m^{-3} respectively.

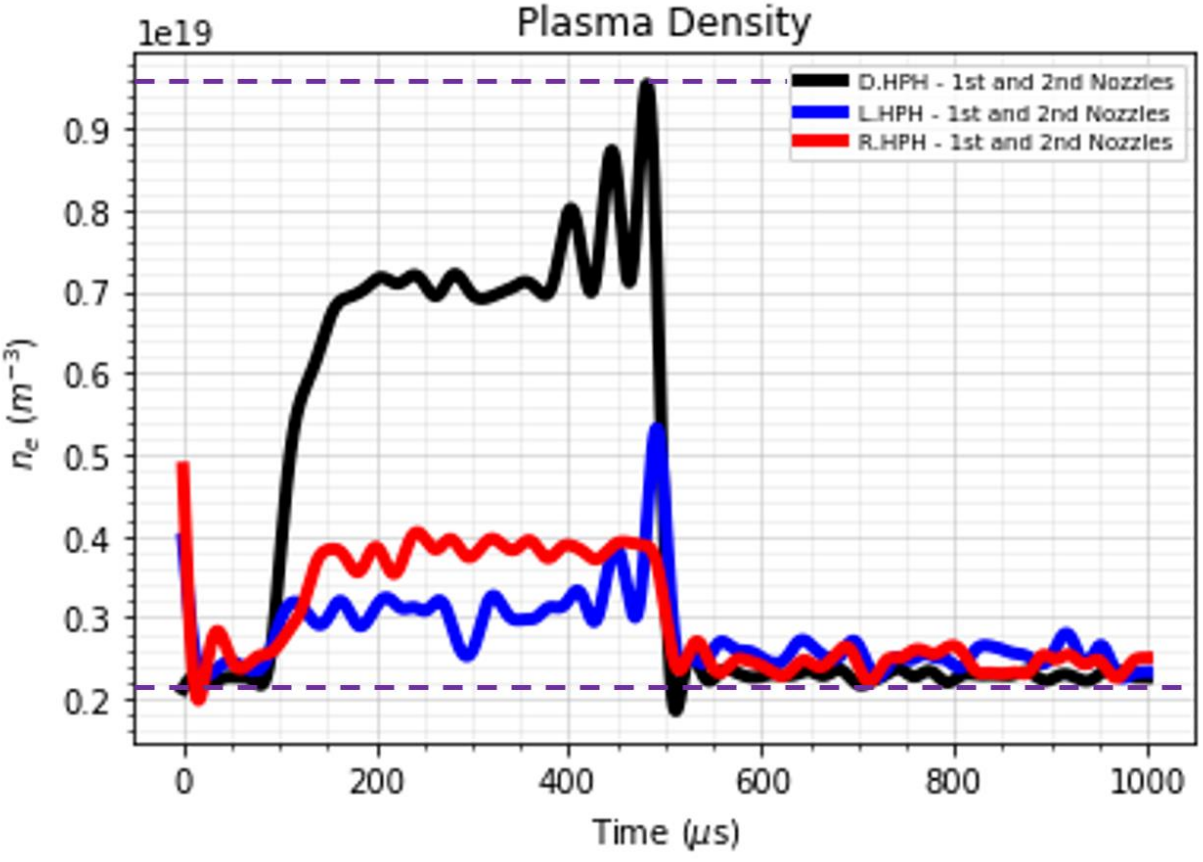

Figure 6.3: On-axis density measurements of left HPH, right HPH, and double HPH thrusters with all magnetic nozzles active in the variant 3 flux conserving configuration.

The second set of diagnostic measurements in the variant 3-flux conserving configuration used the TOF probes to estimate the ion velocity. It consisted of the RF-DLP probe at axial locations of Z = 54.7 cm and DLP#2 at Z = 128.2 cm, separated axially 73.5 cm and biased at -65 V, to determine the time-of-flight of the clustered plasma plume. In Figure 6.4, the peak-to-peak current technique is used to estimate the ion velocity between the adjacent axial probes at thruster centerline. With a time-of-flight of 34.9 μs, the estimated ion velocity corresponds to 21.1 km/s for the double HPH operation.

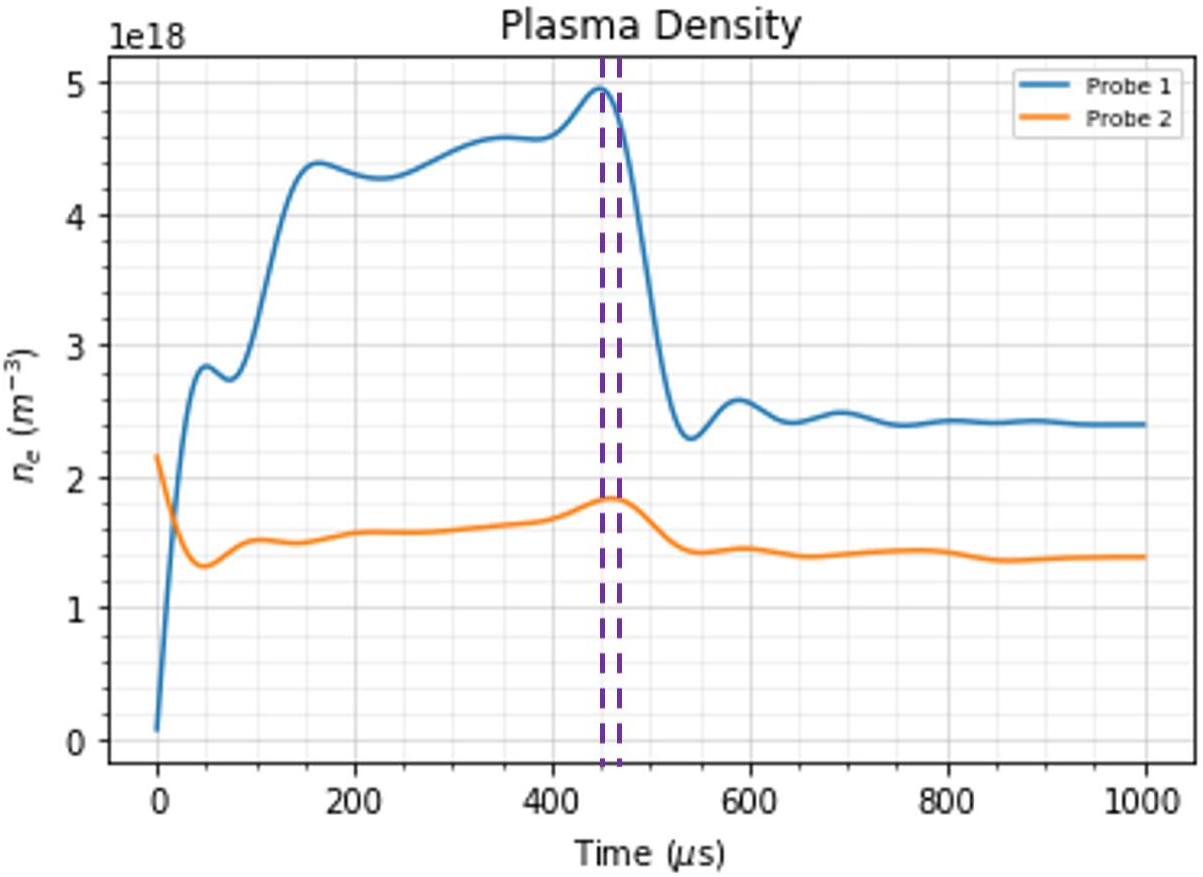

Figure 6.4: Using a peak-to-peak current technique between probe traces, a time of flight of 34.9 μs was determined for variant 3 flux configuration, corresponding to an estimated ion velocity of 21.1 km/s for double HPH thruster.

Peak ion flux calculations were determined by multiplying the peak plasma density and the ion velocity for double HPH operations in the variant 3 flux conserving case. Table 6.2 provided the peak ion flux calculations. Variant 3 flux conserving case increased in peak ion flux ~71% higher than the variant 2 flux conserving case for double HPH operations. From these results, transitioning to a more compact magnetic nozzle configuration could potentially further enhance overall beam collimation and exit velocity. Radial profiles provided insight about the beam width and divergence of the clustered HPH plumes.

Table 6.2: Peak Ion Flux Calculations for the Variant 3 Flux Conserving Configuration

Ion Fluxes Calculations (Variant 3)			
Thruster Mode	**Plasma Density, n_i**	**Estimated Ion Velocity, v_i**	**Peak Ion Flux, <nv>**
Double HPH	$7.4\ x\ 10^{18}\ m^{-3}$	21.1±1.1 km/s	$\mathbf{15.6\ x\ 10^{22}\ m^{-2}s^{-1}}$

Radial density profiles were determined using the RF-DLP at an axial location of Z = 54.7 cm from the Z = 0 source region. Figure 6.5 shows the radial density profile of double HPH thruster operation. The plasma density of 7.4 x 10^{18} m^{-3} is peaked on-axis and exhibited a monotonically decrease in density ±5 cm in radial extent, then plateaued around 3.0 x 10^{18} m^{-3} as the probe traveled toward ±20 cm radial extent. A fit was applied to the experimental data. The FWHM is approximated as 16 cm or 0.70 large magnet radii. It should be noted that a ~54.3% drop in beam width was observed from the variant 2-close flux condition to the recent variant 3-flux conserving condition.

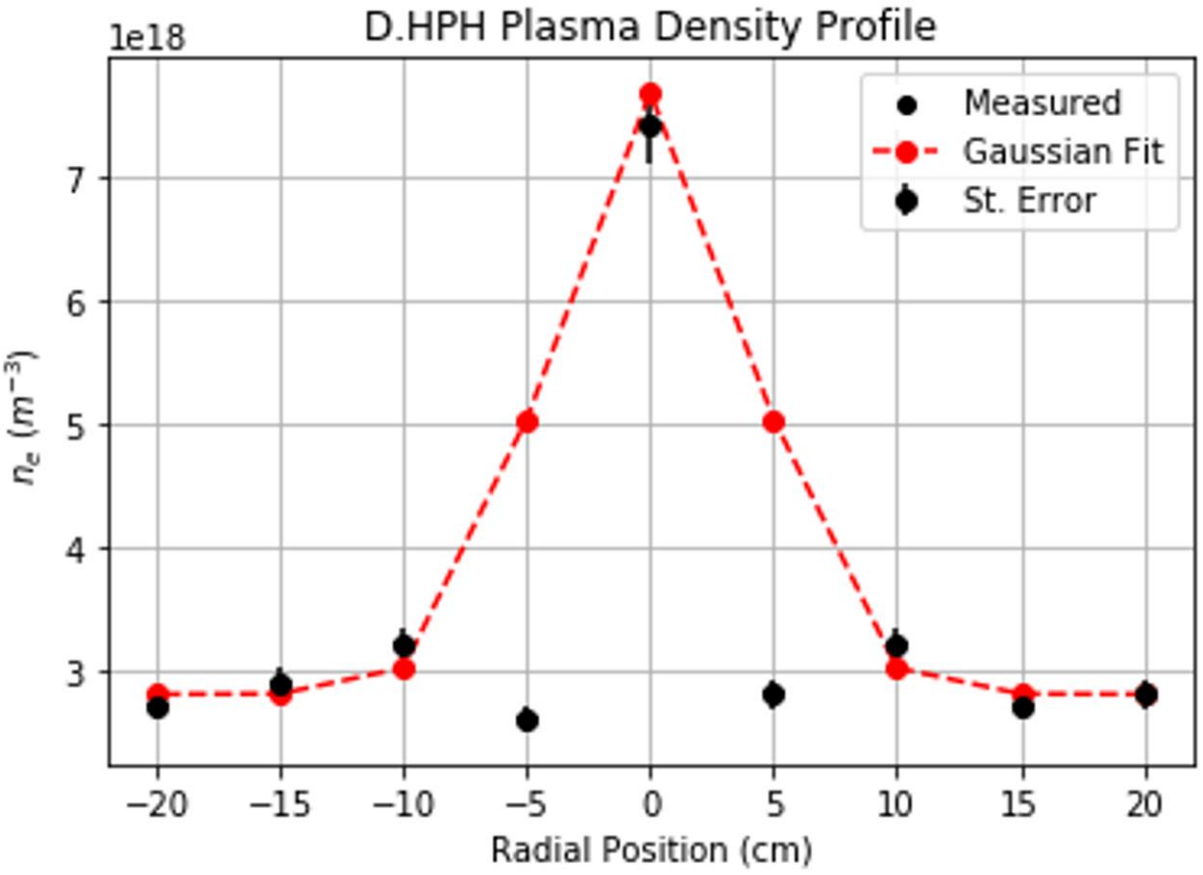

Figure 6.5: Radial density profile of the double thruster operation, with all magnetic nozzles active in the variant 3-flux conserving configuration. FWHM is approximated as 16 cm or 0.70 large magnet radii.

The third set of diagnostic measurements in the variant 3-flux conserving configuration used the NFP probe to determine the ion current density. Figure 6.6 shows the radial ion current density profile for double HPH operations. The current density is peaked on-axis at 318 A/m^2 and decreases off-axis until $\pm$10 cm in radial extent. The current density plateaued around 130 A/m^2 current density as the probe traversed toward $\pm$20 cm in radial extent. It should be noted that a ~42% drop in current density was measured from the variant 2-close flux condition to the recent variant 3-flux conserving condition. A justification for the decrease in variant 3 current density

could be attributed to less charge-exchange collisions entering the periphery of the NFP due to lower background facility pressures [Ref. 62, 67], minimizing sheath effects and thereby producing a more realistic current density measurement. As a comparison, the current density profiles of variant 2 and variant 3 flux conditions were displayed in Figure 6.7. In variant 2 flux condition, the orientation, pitch, and high background neutral pressure of $5\,x\,10^{-6}\,Torr$ may have contributed to a higher population of charge-exchange (CEX) collisions entering the NFP. Artificially higher off-axis current densities can be a characteristic effect of CEX collisions in high background environments, leading to a "winged" shaped profile [Ref. 67] as seen in the variant 2 case. Without any pitch angle and lower background pressures of $3\,x\,10^{-6}\,Torr$, the variant 3 current density profile exhibited a narrower beam profile, with a FWHM of ~16 cm or 0.70 large magnet radii. It should be noted that the variant 3 beam width decreased by more than two-fold in comparison to the variant 2 beam width.

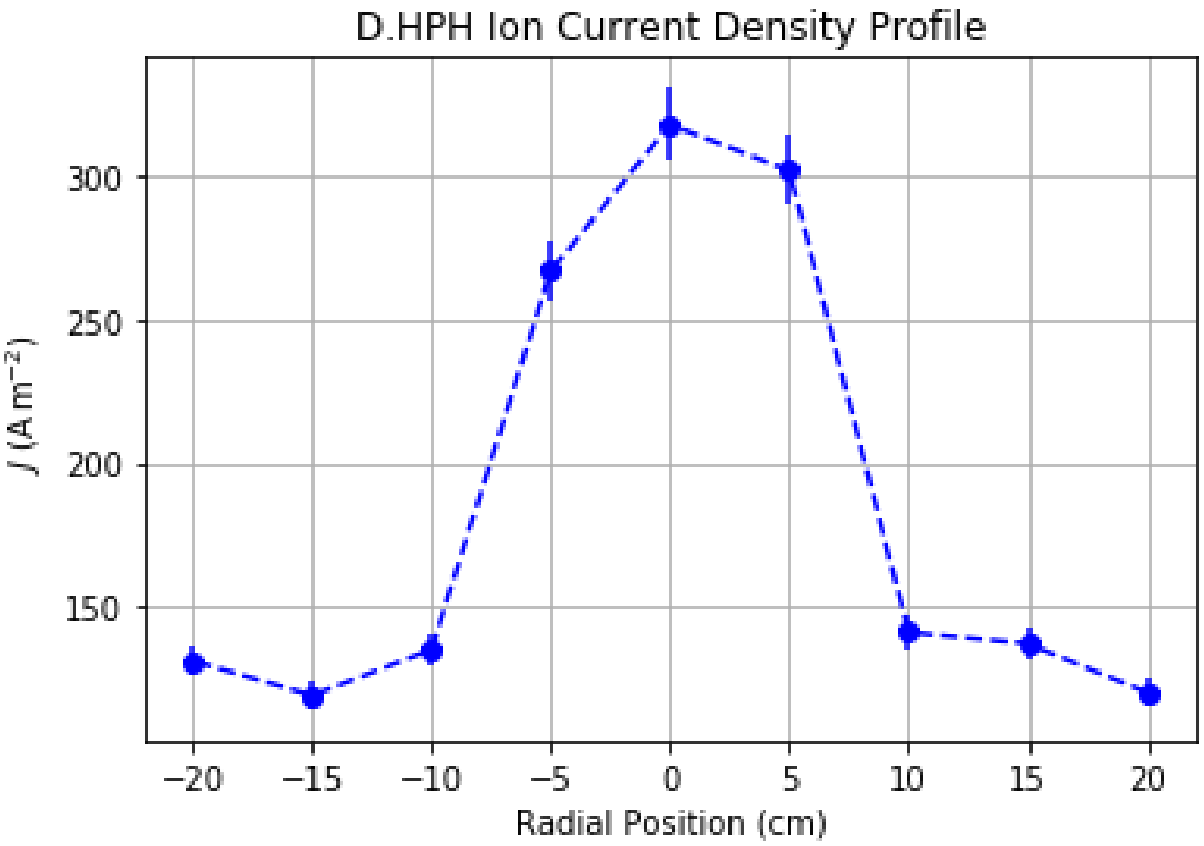

Figure 6.6: Radial density profile of the double thruster operation, with all magnetic nozzles active in the variant 3-flux conserving configuration. Current density is peaked on-axis at 318 A/m^2. FWHM is approximated as 16 cm or 0.70 large magnet radii.

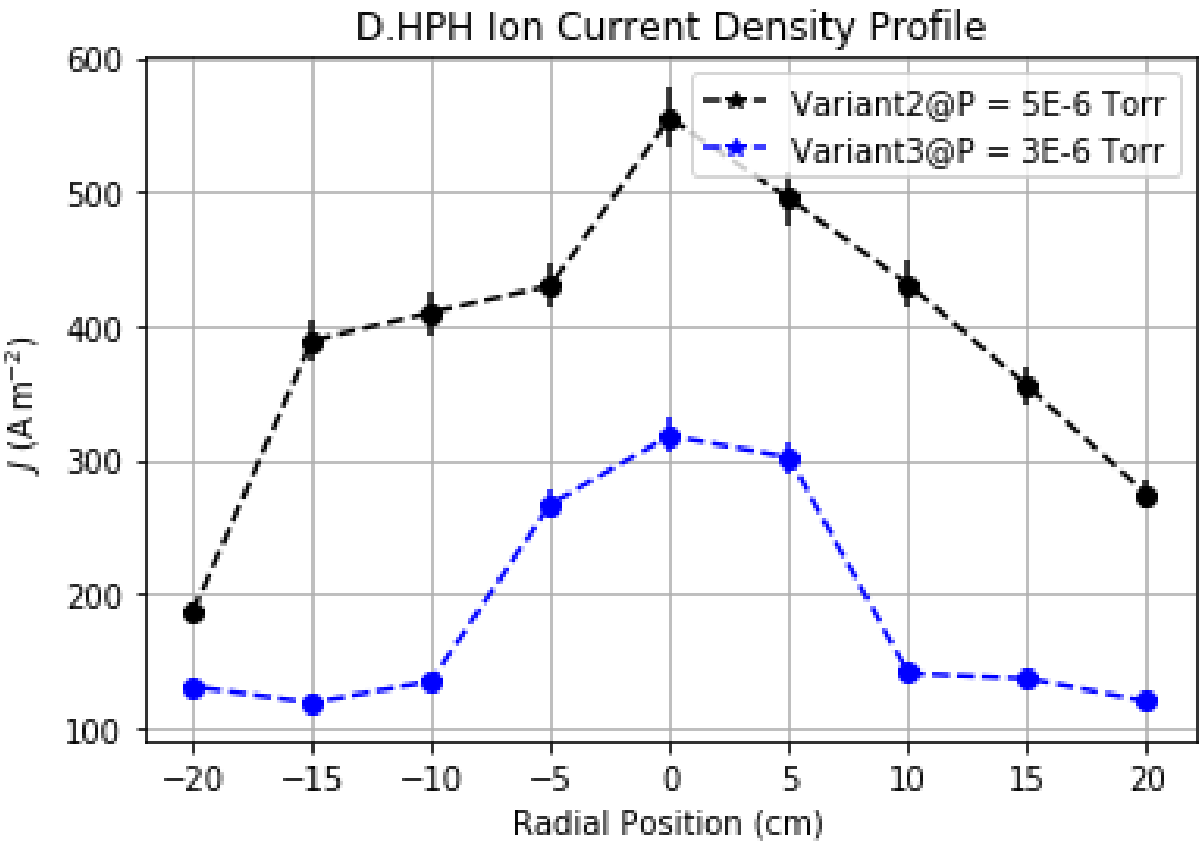

Figure 6.7: Comparative analysis of ion current density profiles. Variant 2 current density (black) exhibited "winged" shape profile characteristic of CEX collisions at higher background pressures. Variant 3 (blue) has more than a two-fold decrease in the beam width than the variant 2 case.

The fourth set of diagnostic measurements in the variant 3-flux conserving configuration used the RF-DLP probe to better predict the electron temperature. The RF-DLP was located at an axial location of Z = 54.7 cm from the source region. A current-voltage (I-V) curve is depicted in Figure 6.8. Based on the regression fits at ion saturation, electron retarding, and electron saturation regimes, the ion saturation current is 14 mA, saturation voltage is 30 V, and the electron temperature is determined to be approximately 15 eV. The variant 3 flux conserving case demonstrated a 50% increase in electron temperature in comparison to the variant 2 flux

conserving case. The exit velocity scales proportional to the square root of the electron temperature. As such, the ratio of the square root of the electron temperatures for variant 3 and variant 2 suggest a ~ 22% increase in the exit velocity. Using the TOF probes, the ion velocity was estimated to be 18.3 km/s (variant 2) and 21.1 km/s (variant 3). The variant 3 exit velocity increased by ~15%, which is not far from ~22% electron temperature ratio estimate. Further optimization efforts to boost clustered HPH performance in terms of electron temperature, plasma density, ion velocity, ion energy, and ion current density are discussed in the next subsequent conclusion and future recommendations section.

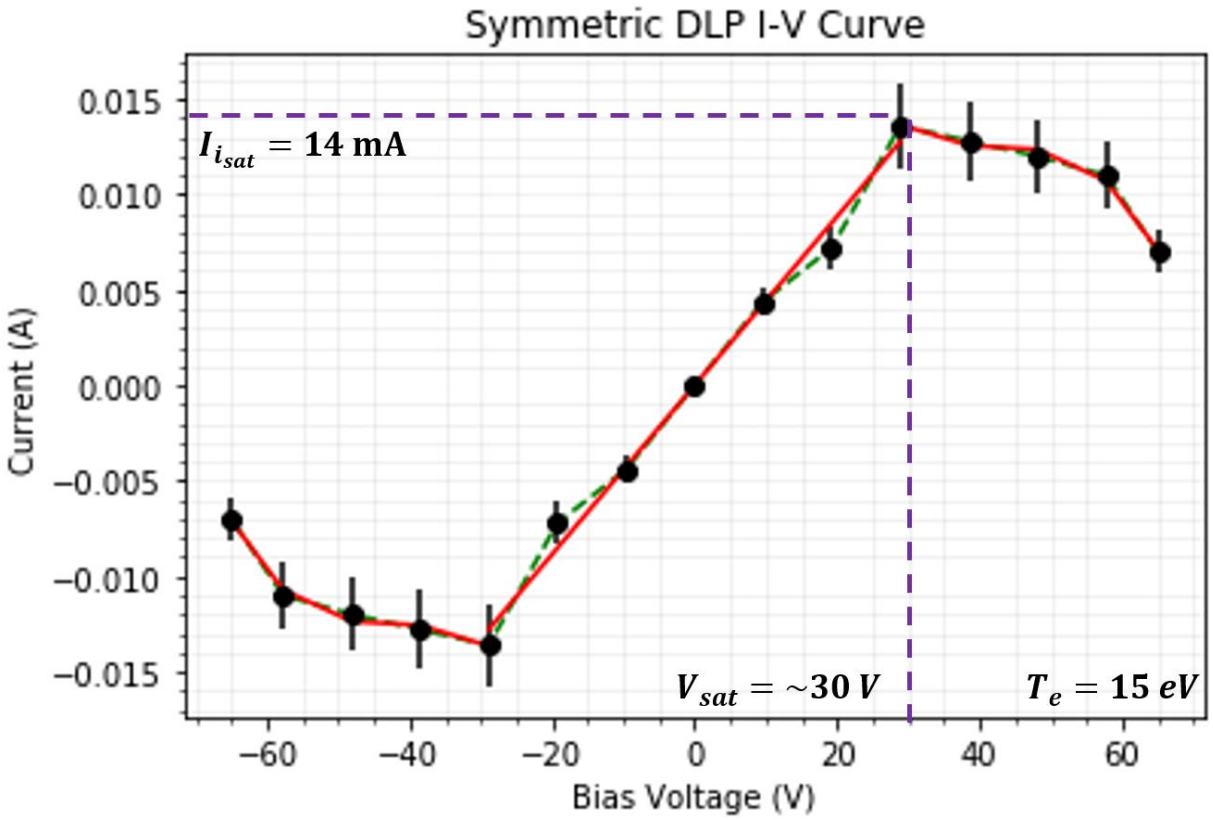

Figure 6.8: A current-voltage (I-V) curve using an RF-DLP diagnostic at thruster centerline (R = 0) to better predict the electron temperature of clustered HPH plumes in the variant 3 flux conserving configuration.

Chapter 7. Conclusion and Future Recommendations

7.1 Summary of Key Findings

In this research, three flux conserving, magnetic nozzle configurations were tested using a suite of plasma diagnostics to improve helicon thruster performance in terms of beam collimation and high exit velocity while minimizing the beam divergence. Diagnostics were able to characterize the electron temperature, plasma density, ion velocity, and ion current density for the clustered HPH plumes. In variant 1 configuration, the DLP diagnostic was used to determine the plasma densities for left HPH, right HPH, and double HPH operations with 1st magnetic nozzle active. The double HPH plasma density was 50% greater than the sum of the left and right HPH thrusters. In variant 2 configuration, the double HPH plasma density was 117% (2.17-fold) larger than the sum of the left and right HPH thrusters' plasma density. The ion velocity was estimated as 18.3 km/s and the peak ion flux was calculated as $9.15\ x\ 10^{22}\ m^{-2}s^{-1}$ for double HPH operations compared with ion velocity of 11 km/s and peak ion flux of $\sim 1.29\ x\ 10^{22}\ m^{-2}s^{-1}$ for single HPH operations. The variant 2 double HPH peak ion flux was 256% (3.56-fold) larger than the sum of the left and right HPH thrusters. The FWHM from variant 2 current density profiles were 2.34-fold larger than the variant 3 current density profiles. Variant 2 double HPH radial sweeps showed wide beam profiles, FWHM ≥35 cm, for plasma density and ion current density which could suggest large divergence angles. In variant 3 configuration, the architectural design was modified to remove the pitch angle and reposition magnetic nozzles closer to the source region. The variant 3 plasma density, ion velocity, ion flux, and electron temperature increased by 48%, 15%, 71%, and 50% respectively in comparison to the variant 2 configuration. Variant 3 radial sweeps showed narrow beam profiles, FWHM ~16

cm, for plasma density and ion current density which could suggest smaller divergence angles. Based on these research results, a new optimum clustered configuration can be suggested for enhanced beam collimation and high exit velocities.

7.2 Suggestions for Future Work

Future Investigations 1: An optimum clustered configuration, a super close flux configuration could further enhance beam directivity and exit velocities for a cluster of two HPH thrusters by repositioning the magnetic nozzles much closer to the Z = 0 source region. An illustration of the suggested magnetic topology can be seen in Figure 7.1. In this configuration, the 1st and 2nd magnetic nozzles are moved to Z = 2.3 cm and Z = 15.3 cm downstream of the source region. With proper shielding and minimal electrical cross-talk between adjacent thruster circuits, the super close flux conserving configuration (variant 4) could lead to significant improvement in beam collimation and high exit velocities. In the newest magnetic nozzle variant, the clustered research would like to achieve even higher beta ($\beta > 1$) plasma thruster plumes, where the ion kinetic energy dominates over the magnetic pressure, to achieve higher exit velocities while minimizing the beam divergence angle. The same set of plasma diagnostics could be used to characterize the downstream plume properties i.e. electron temperature, plasma density, ion current density, ion energy, and ion velocity.

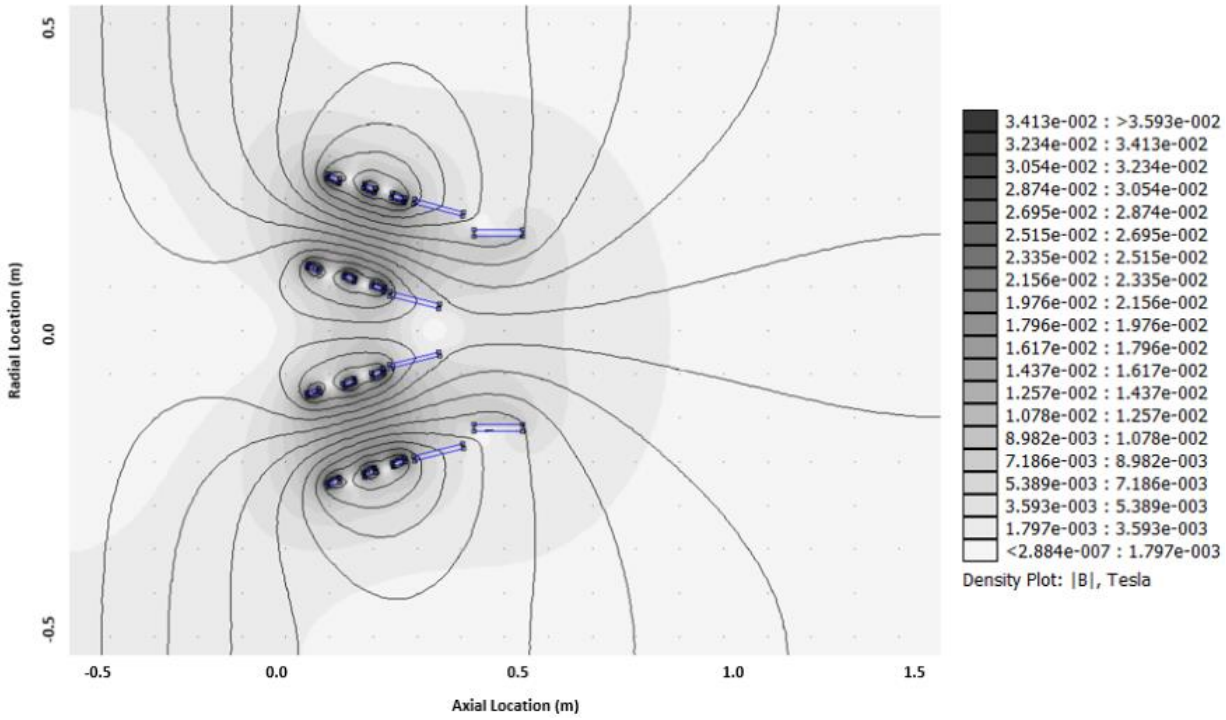

Figure 7.1: Super close flux conserving configuration (variant 4), where the 1st magnetic nozzle is located at Z = 2.3 cm while the 2nd magnetic nozzle is moved to Z = 15.3 cm away from the source region.

Future Investigations 2: Characterization of the downstream plume properties from the super close flux configuration using an assortment of propellant gas species. The clustered HPH experiment has focused on Argon propellant as a fuel source while adjusting operating knobs to achieve a high density, high specific impulse system with low beam divergence. Once these aims have been fully explored in the super close flux configuration, the research could investigate the effects of Krypton or Xenon propellant on the downstream thruster plume properties. It is desirable to choose a propellant source that has a low ionization energy such as Xenon or Krypton, however these propellants are not as abundant and cost-prohibitive if enormous quantities are needed for ground-based testing or future interplanetary missions. Since HPH devices are electrodeless

systems, propellant studies can also investigate the use of molecular propellants and measure the effect on beam collimation and exit velocities.

Future Investigations 3: Numerical simulations of clustered helicon sources could provide insights on the magnetic nozzle effect on multiple plasma beam coalescence and propagation. In addition, RF antennas and FEMM magneto-static simulations could be fed into a commercially-available numerical electromagnetic/particle-in-cell (PIC) solver i.e. CST Studio Suite [Ref. 68-71], to improve the power absorption and coupled dynamics of the clustered HPH system. As more thruster units are incorporated into the architectural chassis design, either triple HPH or quadruple HPH, 3d numerical simulations could be needed to further streamline the experimental campaigns.

Future Investigations 4: As more thruster units are considered for the clustered HPH experiment, facility and equipment upgrades might need to be considered. One area of improvement could be the development of an actuated rotary diagnostic platform atop a 2-axis translation stage inside the vacuum facility for precise translations in the R-Z plane. This rotary actuated diagnostic platform could enable two-dimensional mapping as well as performing hemispherical sweeps of the plasma plume using the suite of optical and probe diagnostics. In addition, the platform will allow researchers to follow Faraday probe best practices [Ref. 61], to conduct either radially sweeps or hemispherical sweeps, to calculate the beam divergence of HPH clustered plumes. This actuated platform also resolves the low signal-to-noise ratio issues experienced with the DLP and RPA diagnostics at far axial locations and avoids adding complex amplification circuitry to improve signal response. The author suggests a few wall-mounted probes

be kept in proximity to the source region to validate rotary platform measurements. The actuated platform could minimize sources of error i.e. probe alignment and lever arm droop and allow for reliable diagnostic translations. The rotary diagnostic platform would need to be large enough to accommodate six different plasma diagnostics i.e. DLP, RF-DLP, TOF, NFP, RPA, OES. A 1-axis rotary diagnostic platform has been implemented into a 1000-L vacuum facility to refine actuation and testing protocols as seen in Figure 7.2. The results of this work, subject to a forthcoming publication, could provide design insights for the 2-axis diagnostic platform. Another area of improvement could be adding turbopumps in parallel with the first turbopump to increase the pumping capacity of the vacuum facility. Based on capacitive manometer measurements [Ref. 41], a 12 ms gas puff at each respective thruster corresponds to an Argon propellant mass flow rate of 12 Torr-L/s (947 sccm). As more thruster units are activated, an increase in power and propellant mass flow could affect plume dynamics due to neutral and wall effects. As such, an increase in the pumping capacity could reduce the gas load on each pumping line and shorten the time in between experimental shots. Moreover, the RF-PPU units need to be upgraded or modified to accommodate $\geq$ 3 HPH thruster operation. Furthermore, the thruster architecture could use some structural reinforcement to accommodate more thrusters as well as a centralized hub for electrical and gas routing. Renderings for triple HPH or quadruple HPH operations are shown in Figure 7.3 and Figure 7.4 respectively. Further enhancements in ion beam collimation and exit velocities could be expected due to the coherent addition of three or four helicon waves.

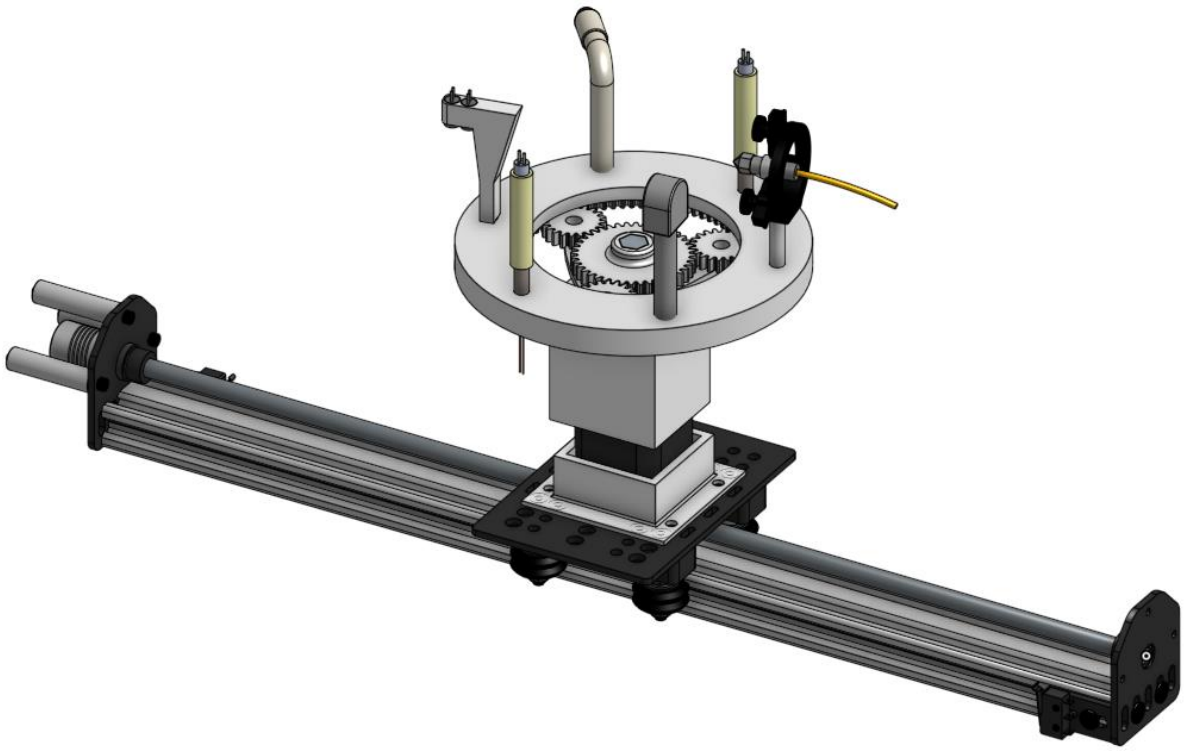

Figure 7.2: CAD rendering of the 1-axis rotary actuated diagnostic platform. A test platform to refine actuation and testing protocols prior to the development of a 2-axis actuated diagnostic platform.

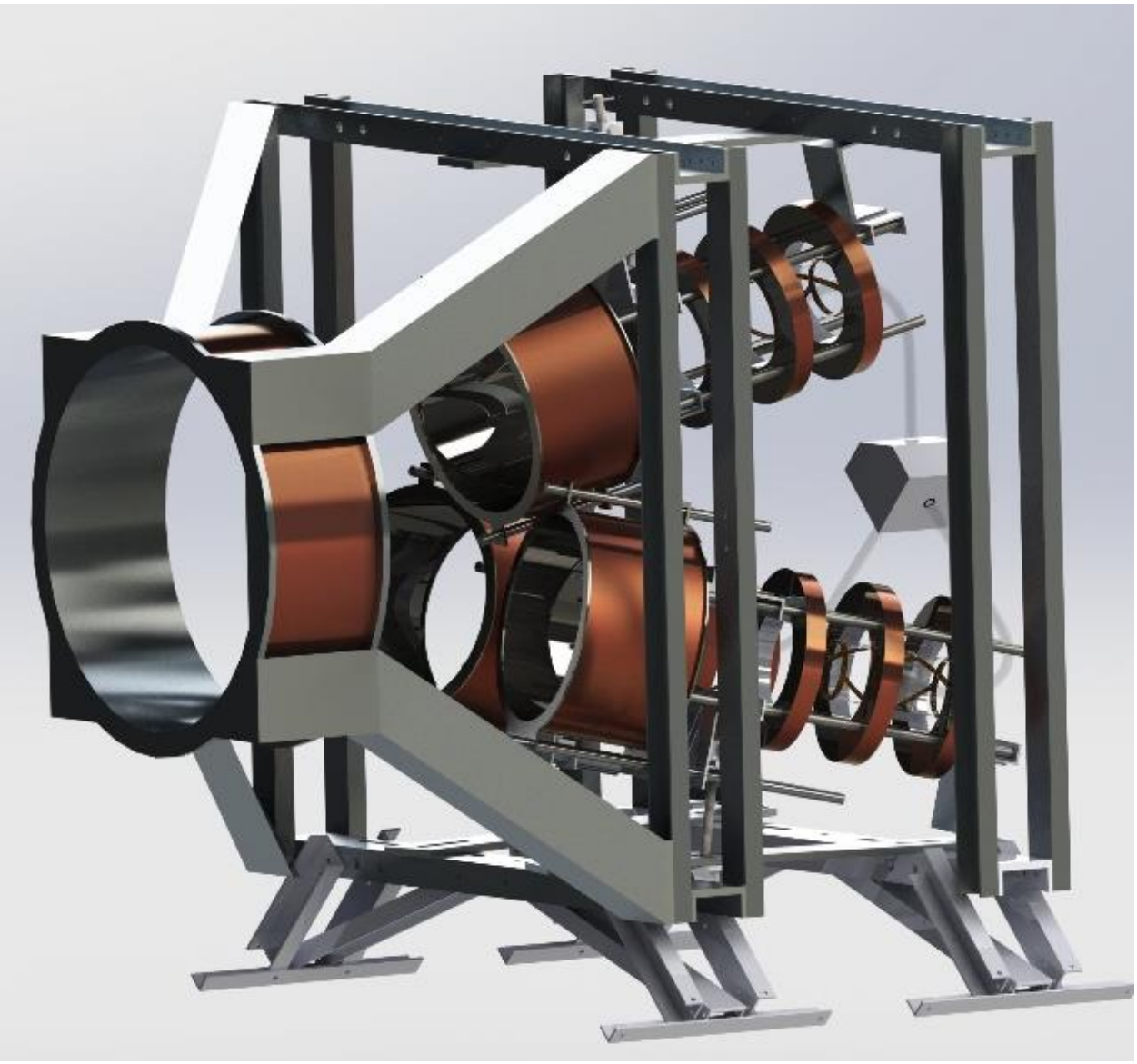

Figure 7.3: CAD rendering of the three HPH thrusters (triple HPH) aimed toward the centerline axis of the 2nd magnetic nozzle. A gas distribution box evenly distributes the gas flow into each respective source region.

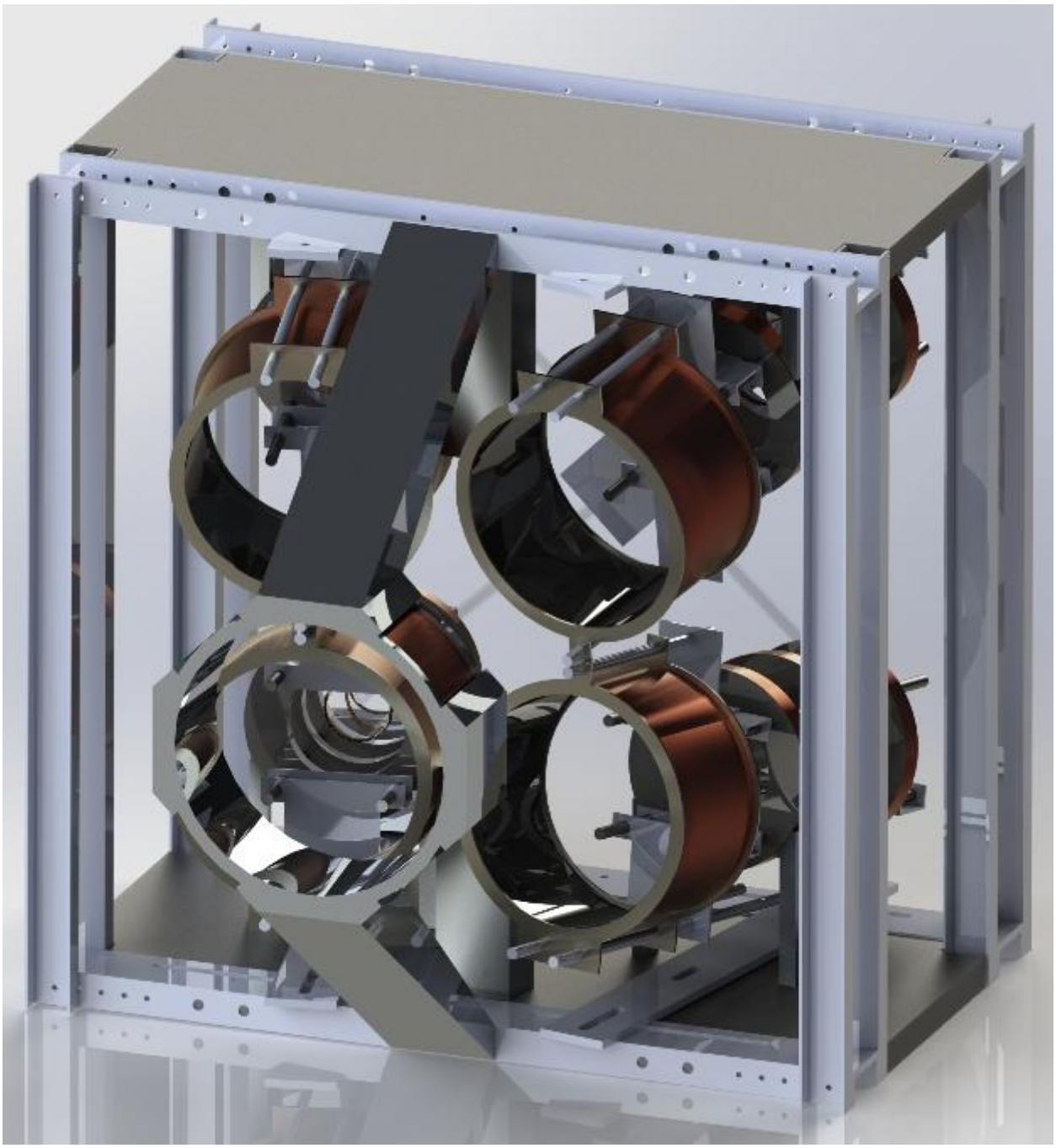

Figure 7.4: CAD rendering of the four HPH thrusters (quadruple HPH) aimed toward the centerline axis of the 2nd magnetic nozzle. A gas distribution box can be seen in the background.

Future Investigations 5: With a suite of probe diagnostics potentially mounted atop of an actuated rotary platform inside the large vacuum facility, an in-direct thrust measurement

could be inferred from these precise swept diagnostics. Ion momentum flux density profiles could be corroborated using a plasma momentum flux sensor (PMFS). A PMFS has been used by the VASIMR group to determine the imparted ion momentum flux onto a target plate in the downstream plume region [Ref. 72]. With the use of a PMFS, the total force can be determined by integrating the ion momentum flux density over one full plume diameter. The integration of the quadruple HPH and the PMFS diagnostic inside the vacuum facility can be seen in Figure 7.5. Once ion momentum flux density (thrust) measurements have been determined via in-direct or direct methods, the plasma jet power, thruster efficiency, and thrust-to-power ratio can be calculated to fully quantify clustered HPH performance. With detailed quantitative analysis of the clustered HPH system, beam-target interactions could be further investigated. Applications could include space debris remediation, beamed-momentum transfer onto power-limited satellites, and using an energetic ion beam source for testing advanced radiation shielding systems.

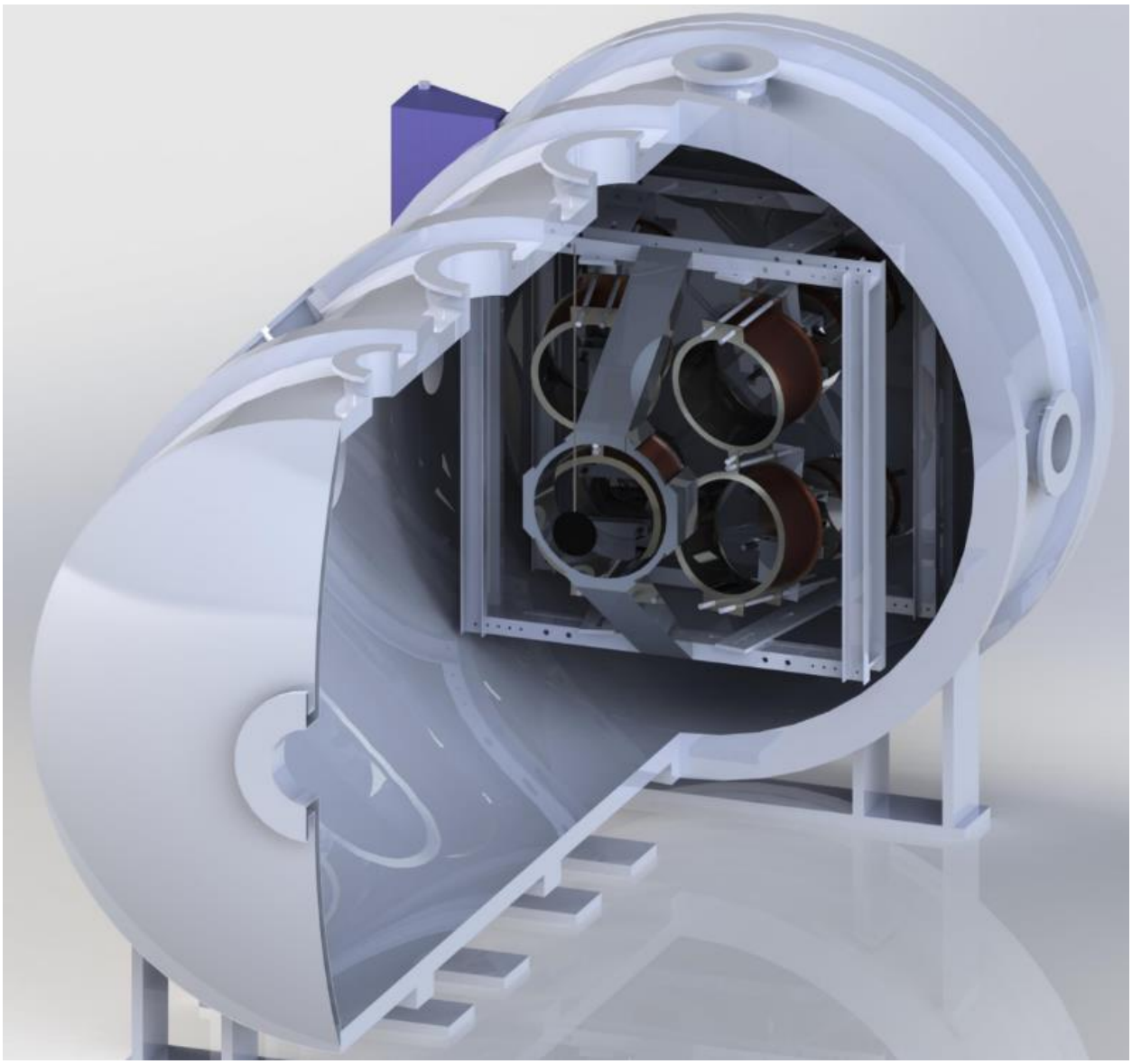

Figure 7.5: CAD rendering of the four HPH thrusters (quadruple HPH) and PMFS diagnostic mounted inside the 4800-L vacuum facility.

Appendices

High-power mission scenarios enabled by the clustered HPH architecture, the plasma phased array (PPA), are discussed in Appendix A and Appendix B. Appendix A discusses high-power ≥100 kW solar electric propulsion applications in the near-Earth and cislunar space environments. Appendix B discusses high power ≥1 MW nuclear electric propulsion applications toward the Moon, Mars, and beyond. Several of these applications are the subject of forthcoming feasibility study publications that will discuss mission concepts and operations, orbital trajectories, transit times, and mass fuel consumption.

Appendix A: High-Power Solar Electric Propulsion (SEP) Mission Studies

High-power solar electric propulsion (SEP) missions are considered near-term solutions to enable robotic and heavy cargo transportation within the near-Earth and cis-lunar space environment. A feasibility study has been performed to actively remove orbital debris from the LEO environment using the PPA architecture [Ref. 73]. The internal sub-systems of the SEP-PPA architecture can be seen in Figure A.1. For the active debris removal scheme, the PPA architecture performs rendezvous operations to detumble, capture, and deorbit multiple large orbital debris toward a pre-defined disposal orbit. The operation modes can be illustrated in Figure A.2. Additional feasibility studies are planned for active debris removal in the (1) densely populated megaconstellations LEO orbits and (2) the geostationary orbit (GEO) toward a graveyard orbit (GYO). The SEP-PPA architecture is equipped with a multi-arm robotic manipulator to enable on-orbit servicing and space tug applications. Cis-lunar space applications include (1) near-Earth asteroid (NEA) scouting and planetary defense missions as seen in Figure

A.3, and (2) heavy cargo transportation from geosynchronous transfer orbit (GTO) to a lunar near-rectilinear halo orbits (NRHO) as seen in Figure A.4.

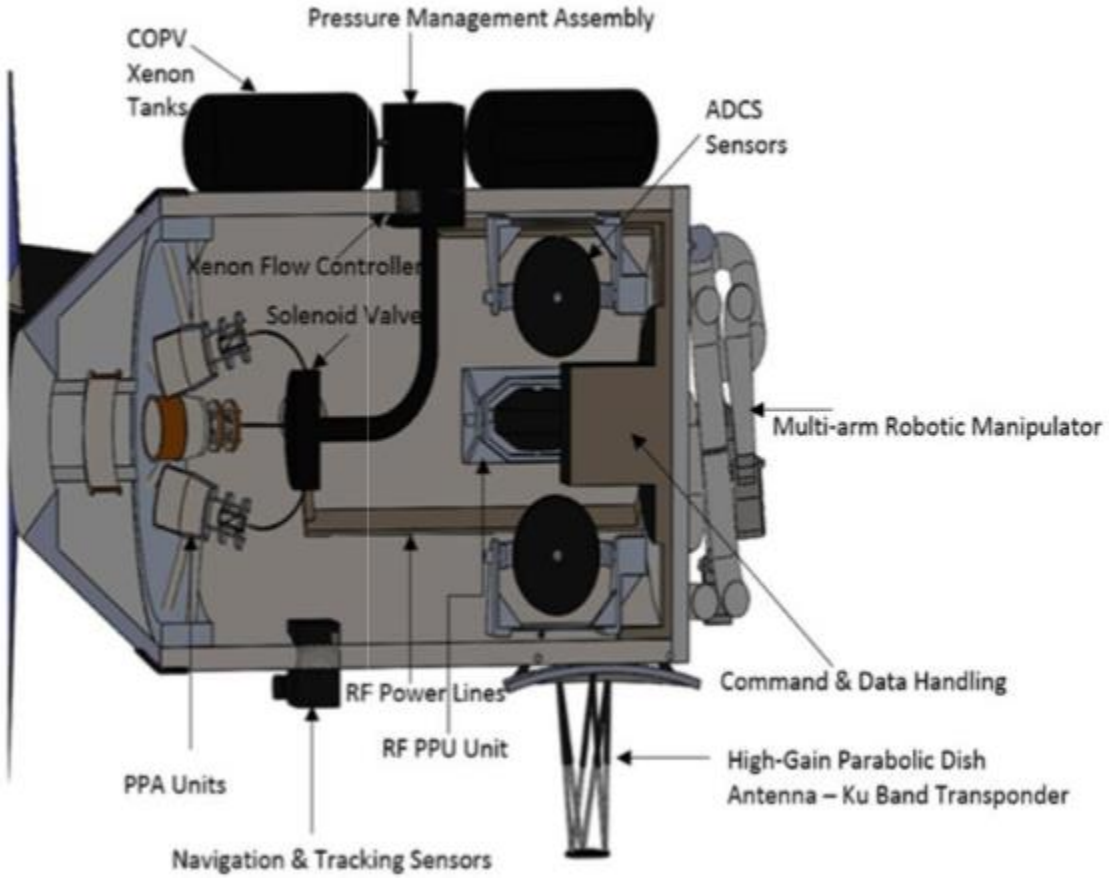

Figure A.1: The internal components and key sub-systems of the SEP-PPA architecture.

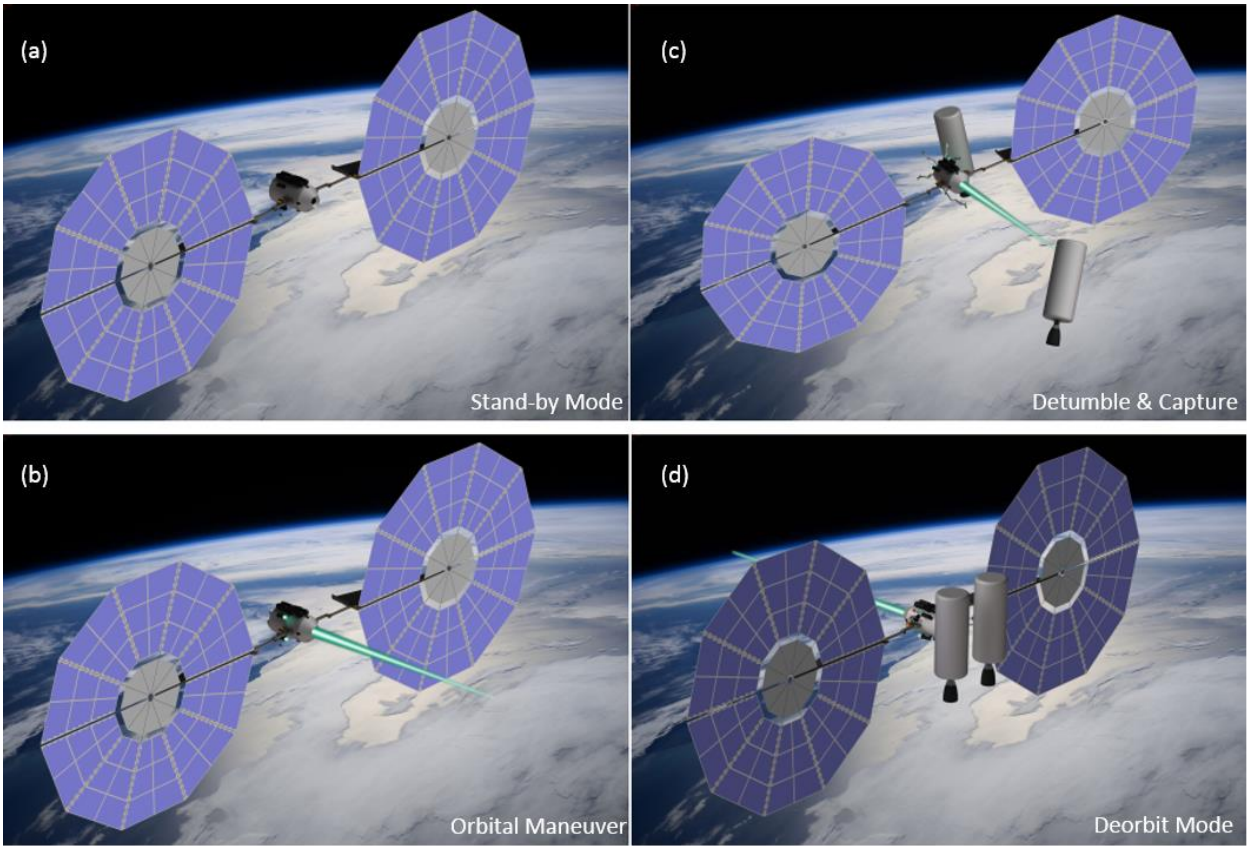

Figure A.2: (a) Stand-by mode, (b) Orbital maneuvers to rendezvous with orbital debris, (c) Detumble rotational debris and capture for transport, (d) Deorbit the entire cluster of large orbital debris at once toward a pre-disposal orbit of 300 km.

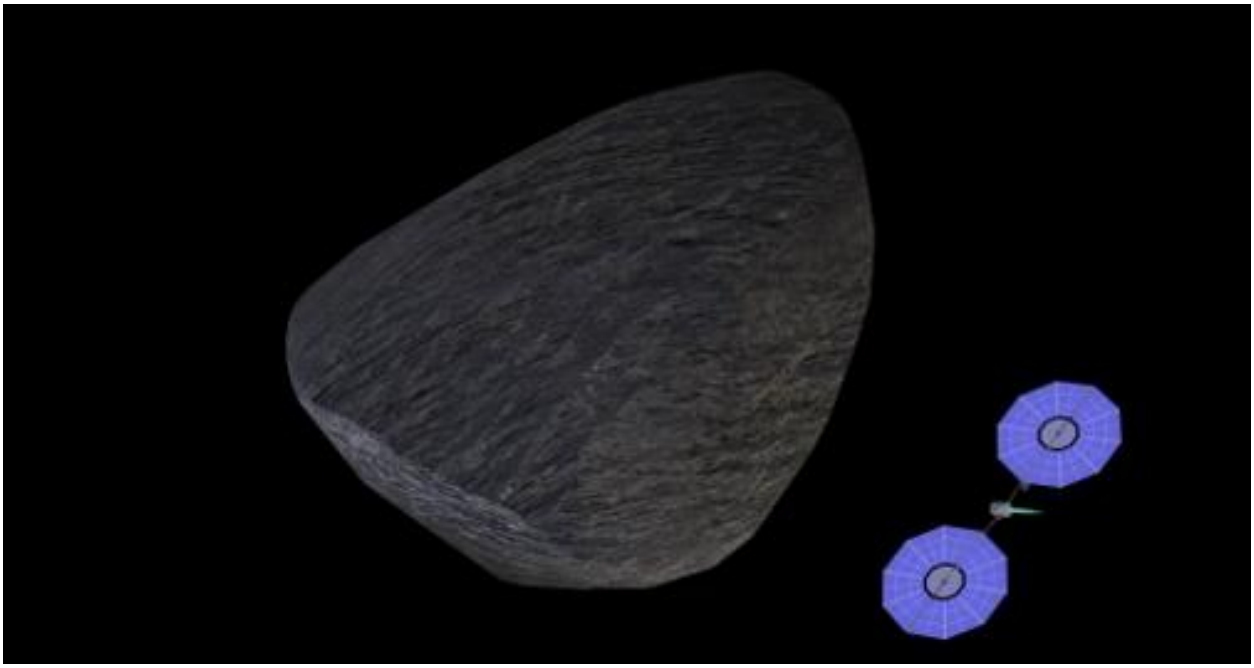

Figure A.3: SEP-PPA architecture performs flyby interactions of a near-Earth asteroid. The spacecraft's onboard sensors are used to determine the size, shape, orientation, and spin rate of NEAs. The data is relayed back to Earth to improve tracking models.

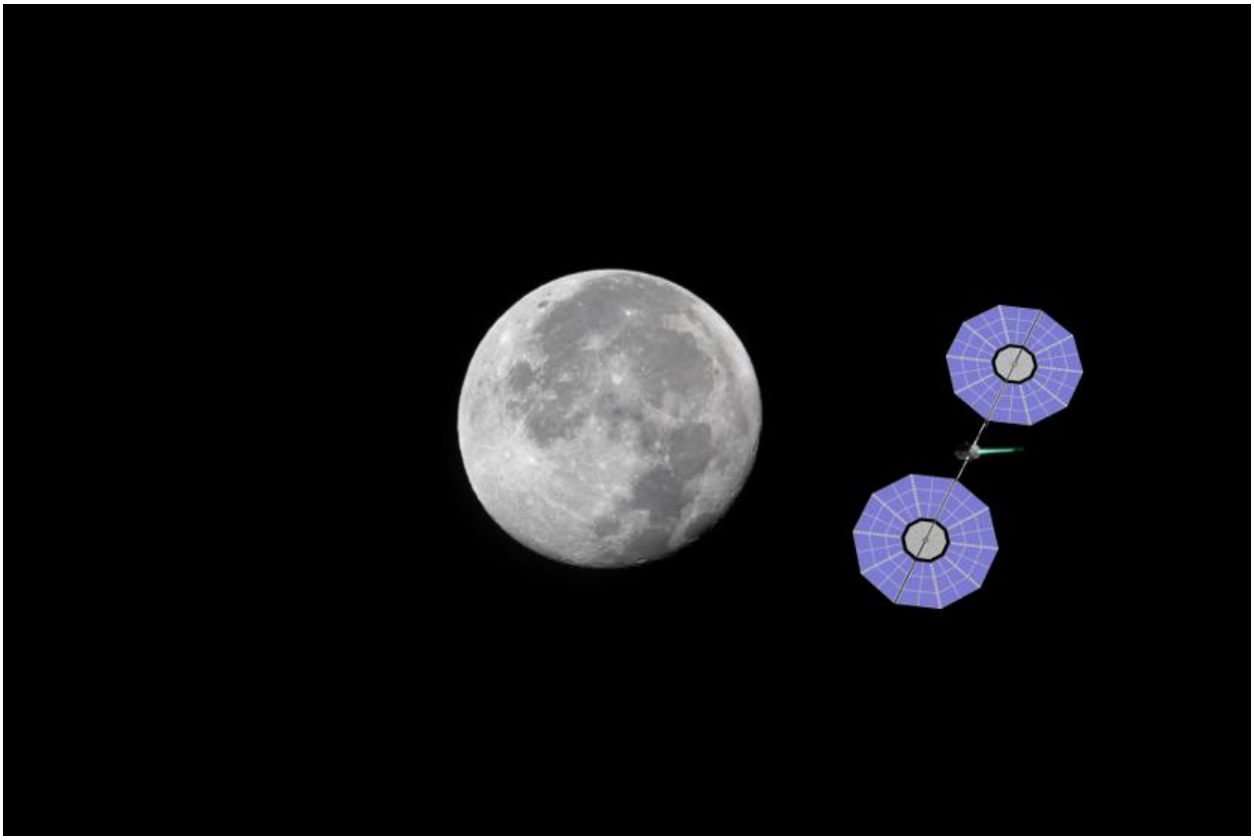

Figure A.4: SEP-PPA architecture performs lunar flybys in preparation for future heavy cargo transportation near the NRHO lunar orbit.

Appendix B: High-Power Nuclear Electric Propulsion (NEP) Mission Studies

High-power nuclear electric propulsion (NEP) missions are considered far-term solutions allowing for ambitious human and robotic deep space exploration endeavors. A NEP-PPA architecture has been developed to improve launch window flexibility, spacecraft maneuverability, and larger payload fractions toward Mars and beyond. The NEP flagship uses low-enriched uranium (LEU) fission reactors, advanced Brayton energy conversion units, high-temperature radiators, and high-power helicon thrusters. With the NEP flagship, there are a total of twenty helicon thrusters, split across two large advanced helicon architectures, that can

operate at multi-megawatt power levels using solid-state switching units. Each thruster unit can process electrical power from 100 – 400 kW_e which allows for a range of mission specific scenarios to be explored. As seen in Figure B.1, the propulsion module consists of a total of ten HPH engines, whereby two sets of four HPH engines are used for primary maneuvers while two HPH engines are back-up redundant units in the event of an emergency. A feasibility study is planned to use the NEP-PPA architecture for cargo and crewed missions to Mars. A cargo NEP flagship, incorporating the advanced PPA architecture, can be seen in Figure B.2. The cargo NEP flagship is ~143 m in length and enables the transport of an orbital fuel depot, large-science payloads, and planetary monitoring small satellites. A human-crew NEP flagship can be seen in Figure B.3. The crewed NEP flagship is ~122 m in length and enables the transport of a human crew utilizing advanced radiation shielding and artificial gravity systems to minimize the physiological effect on human crew during long-term microgravity exposure.

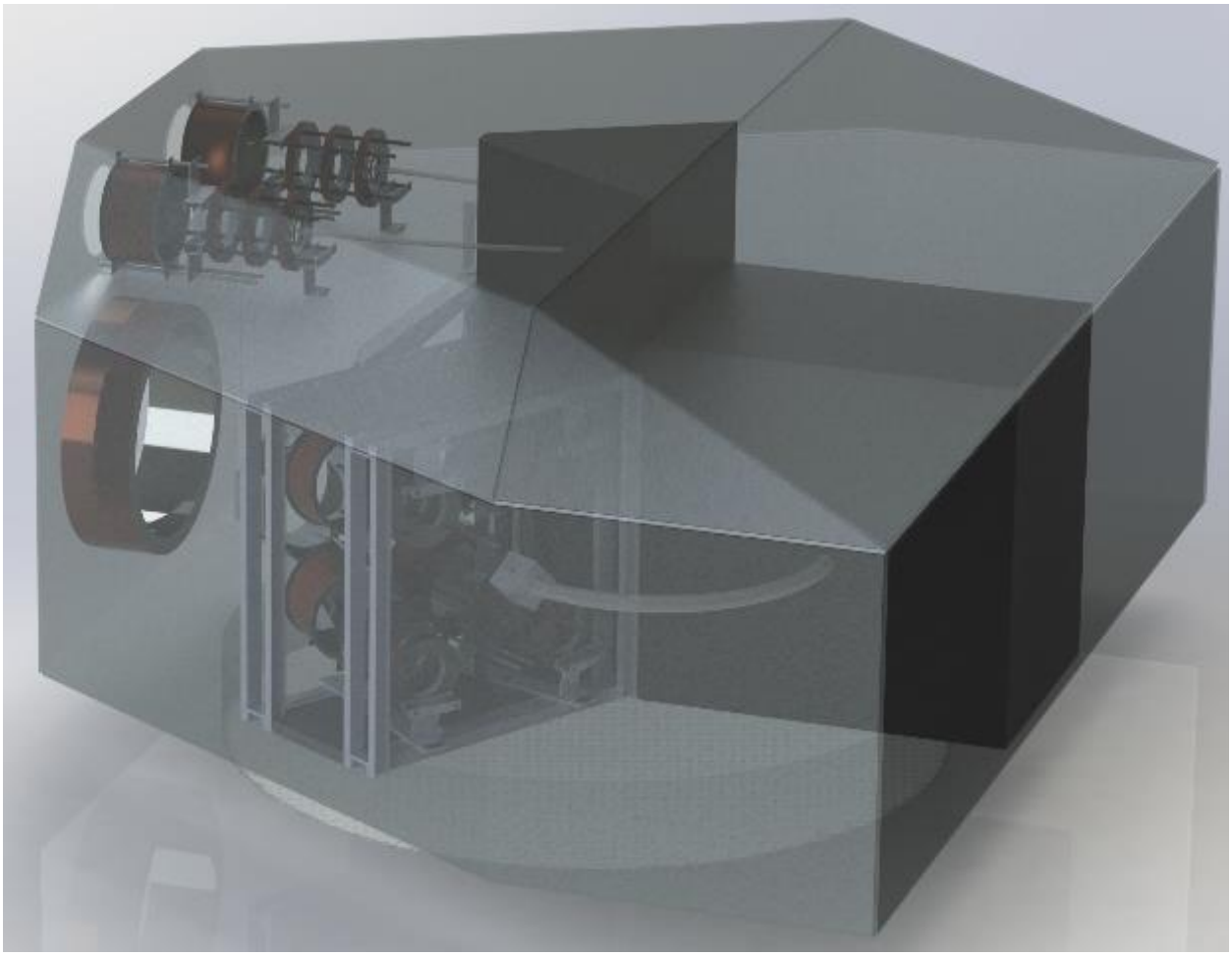

Figure B.1: A propulsion module for the NEP-PPA architecture. The propulsion module consists of a total of ten HPH engines that each can process electrical power between 100 – 400 kW_e for mission specific scenarios. Two sets of four HPH engines are used for primary maneuvers while two HPH engines are back-up redundant units in the event of an emergency.

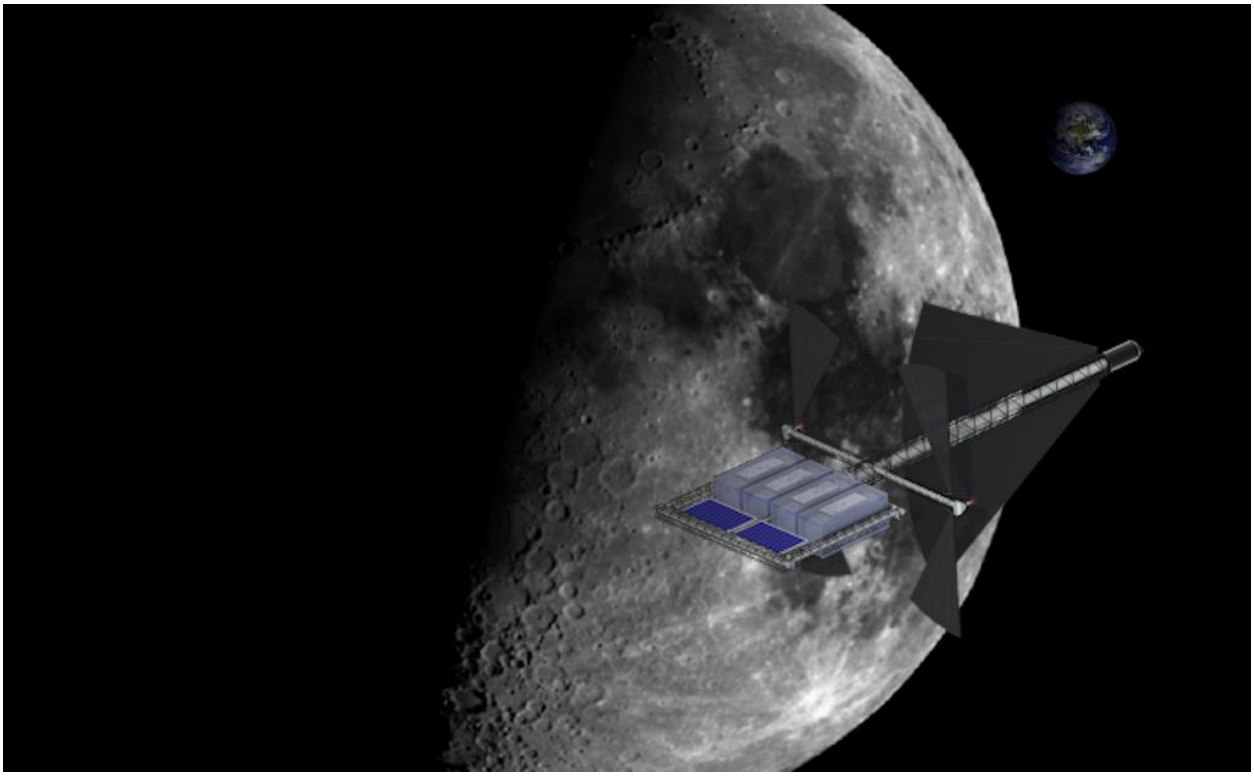

Figure B.2: A multi-megawatt NEP flagship ferrying heavy cargo and scientific payload from the Moon to Mars. The cargo NEP flagship ~143 m in length.

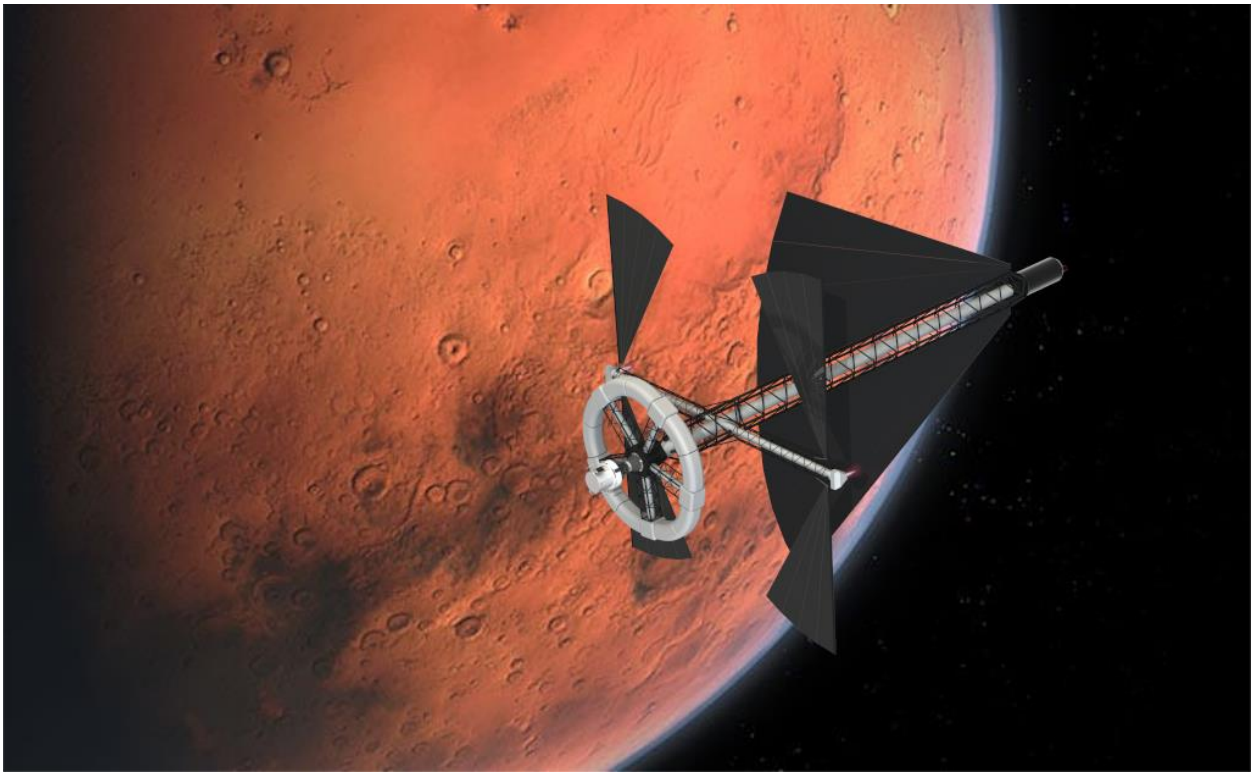

Figure B.3: A multi-megawatt NEP flagship ferrying a human crew to Mars. The crewed NEP flagship ~122 m in length.

References

1. Mazouffre, Stéphane. "Electric propulsion for satellites and spacecraft: established technologies and novel approaches." Plasma Sources Science and Technology 25.3 (2016): 033002.

2. Hoskins, W. Andrew, et al. "30 years of electric propulsion flight experience at Aerojet Rocketdyne." 33rd International Electric Propulsion Conference. 2013.

3. Zube, Dieter M., Keith D. Goodfellow, and Chris Hearn. "Development of a Hydrazine Arcjet System Operating at 100 Volts Input Voltage." (2017).

4. Arrington, Lynn A., et al. "A performance comparison of pulsed plasma thruster electrode configurations." (1997).

5. Northway, Paige, et al. "Pulsed Plasma Thruster Gains in Specific Thrust for CubeSat Propulsion." 53rd AIAA/SAE/ASEE Joint Propulsion Conference. 2017.

6. Florenz, Roland Edward. "The X3 100-kW Class Nested-Channel Hall Thruster: Motivation, Implementation, and Initial Performance." (2014).

7. Hall, Scott. "Characterization of a 100-kW Class Nested-Channel Hall Thruster." (2018).

8. Liang, Raymond. "The Combination of Two Concentric Discharge Channels into a Nested Hall-Effect Thruster." (2013).

9. Walker, Mitchell Louis Ronald. Effects of facility backpressure on the performance and plume of a Hall thruster. University of Michigan, 2005.

10. Boswell, Roderick William. "Very efficient plasma generation by whistler waves near the lower hybrid frequency." Plasma Physics and Controlled Fusion 26.10 (1984): 1147.

11. Light, Max, and Francis F. Chen. "Helicon wave excitation with helical antennas." Physics of Plasmas 2.4 (1995): 1084-1093.

12. Chen, Francis F. "Helicon discharges and sources: a review." Plasma Sources Science and Technology 24.1 (2015): 014001.

13. Pavarin, Daniele, et al. "Low power rf plasma thruster experimental characterization." 48th AIAA/ASME/SAE/ASEE Joint Propulsion Conference & Exhibit. 2012.

14. West, Michael D., Christine Charles, and Rod W. Boswell. "Testing a helicon double layer thruster immersed in a space-simulation chamber." Journal of Propulsion and Power 24.1 (2008): 134-141.

15. Trezzolani, F., et al. "Low power radio-frequency plasma thruster development and testing." Proceedings of the 33rd International Electric Propulsion Conference. 2013.

16. Batishchev, Oleg. "Mini-helicon plasma thruster characterization." 44th AIAA/ASME/SAE/ASEE Joint Propulsion Conference & Exhibit. 2008.

17. Squire, Jared P., et al. "Advances in Duration Testing of the VASIMR® VX-200SS™ System." 52nd AIAA/SAE/ASEE Joint Propulsion Conference. 2016.

18. Ziemba, T., et al. "Plasma characteristics of a high-power helicon discharge." Plasma Sources Science and Technology15.3 (2006): 517.

19. Prager, James, et al. "Wave propagation downstream of a high-power helicon in a dipolelike magnetic field." Physics of Plasmas 17.1 (2010): 013504.

20. Ziemba, Timothy, et al. "High power helicon thruster." 41st AIAA/ASME/SAE/ASEE Joint Propulsion Conference & Exhibit. 2005.

21. Winglee, R., et al. "Simulation and laboratory validation of magnetic nozzle effects for the high-power helicon thruster." Physics of Plasmas 14.6 (2007): 063501.

22. Prager, James, et al. "Ion energy characteristics downstream of a high-power helicon." Plasma Sources Science and Technology 17.2 (2008): 025003.

23. Roberson, B. Race, Robert Winglee, and James Prager. "Enhanced diamagnetic perturbations and electric currents observed downstream of the high-power helicon." Physics of Plasmas 18.5 (2011): 053505.

24. Murakami, Nao, and Robert Winglee. "Downstream Plasma Velocity Measurement and Scaling Law of High-Power Helicon Double Gun Thruster." 51st AIAA/SAE/ASEE Joint Propulsion Conference. 2015.

25. Manzella, David H., and Kurt Hack. "High-power Solar electric propulsion for future NASA missions." 50th AIAA/ASME/SAE/ASEE Joint Propulsion Conference. 2014.

26. Landis, Geoffrey A., Steven R. Oleson, and Carolyn R. Mercer. "Solar electric propulsion for future NASA missions." Photovoltaic Specialist Conference (PVSC), 2015 IEEE 42nd. IEEE, 2015.

27. Loghry, Christopher S., et al. "LEO to GEO (and Beyond) Transfers Using High Power Solar Electric Propulsion (HP-SEP)." (2017).

28. Brophy, John, et al. "300-kW solar electric propulsion system configuration for human exploration of near-earth asteroids." 47th AIAA/ASME/SAE/ASEE Joint Propulsion Conference & Exhibit. 2011.

29. Murphy, David M., et al. "UltraFlex and MegaFlex-Development of highly scalable solar power." Photovoltaic Specialist Conference (PVSC), 2015 IEEE 42nd. IEEE, 2015.

30. Jackson, Jerry, et al. "Development of High Power Hall Thruster Systems to Enable the NASA Exploration Vision [STUB]." (2018).

31. Jorns, Benjamin, et al. "Update on the Nested Hall Thruster Subsystem for the NextSTEP XR-100 Program." 2018 Joint Propulsion Conference. 2018.

32. Squire, Jared P., et al. "Run-time Accumulation Testing of the 100 kW VASIMR® VX-200SS Device." 2018 Joint Propulsion Conference. 2018.

33. Herman, Daniel A., et al. "Overview of the Development and Mission Application of the Advanced Electric Propulsion System (AEPS)." (2018).

34. Spores, Ronald, et al. "Overview of the USAF Electric Propulsion Program." 37th Joint Propulsion Conference and Exhibit. 2001.

35. Beal, Brian Eric. Clustering of Hall effect thrusters for high-power electric propulsion applications. University of Michigan, 2004.

36. Lobbia, Robert B., and Alec D. Gallimore. "Performance measurements from a cluster of four Hall thrusters." Proc. 30th IEPC. 2007.

37. Squire, Jared P., et al. "Development Toward a Spaceflight Capable VASIMR® Engine and SEP Applications." AIAA SPACE 2014 Conference and Exposition. 2014.

38. Nicholson, Dwight Roy. Introduction to plasma theory. New York: Wiley, 1983.

39. Chen, Francis F. "Plasma ionization by helicon waves." Plasma Physics and Controlled Fusion 33.4 (1991): 339.

40. Light, Max, and Francis F. Chen. "Helicon wave excitation with helical antennas." Physics of Plasmas 2.4 (1995): 1084-1093.

41. Prager, James Robert. Experimental investigation of plasma downstream of a high-power helicon. University of Washington, 2008.

42. Slobodov, Ilia. Performance Characterization of the High-Power Helicon Plasma Thruster with Varying Magnetic Nozzle Configurations. Diss. University of Washington, 2011.

43. Sinenian, Nareg. "Propulsion mechanisms in a helicon plasma thruster." (2008).

44. Williams, Logan Todd. Ion acceleration mechanisms of helicon thrusters. Diss. Georgia Institute of Technology, 2013.

45. Chen, F. F. "Double helix: The dawson separation process." From Fusion to Light Surfing: Lectures on Plasma Physics Honoring John M. Dawson, Addison-Wesley, New York(1991): 191-211.

46. Chen, Francis F. "Helicon discharges and sources: a review." Plasma Sources Science and Technology 24.1 (2015): 014001.

47. Blackwell, David D., and Francis F. Chen. "2D imaging of a helicon discharge." Plasma Science, 1997. IEEE Conference Record-Abstracts., 1997 IEEE International Conference on. IEEE, 1997.

48. Roberson, Brandon Race. Experimental Investigation into the Enhanced Diamagnetic Perturbations and Electric Currents Downstream of the High-Power Helicon Plasma Thruster. Diss. 2013.

49. Urrutia, J. M., and R. L. Stenzel. "Whistler modes in highly nonuniform magnetic fields. I. Propagation in two-dimensions." Physics of Plasmas 25.8 (2018): 082108.

50. Stenzel, R. L., and J. M. Urrutia. "Whistler modes in highly nonuniform magnetic fields. II. Propagation in three dimensions." Physics of Plasmas 25.8 (2018): 082109.

51. Stenzel, R. L., and J. M. Urrutia. "Whistler modes in highly nonuniform magnetic fields. III. Propagation near mirror and cusp fields." Physics of Plasmas 25.8 (2018): 082110.

52. Preuss, Robert D., and D. Richard Brown. "Retrodirective distributed transmit beamforming with two-way source synchronization." Information Sciences and Systems (CISS), 2010 44th Annual Conference on. IEEE, 2010.

53. Abdul Latef, Tarik, Salam Khamas, and Ahmed Wasif Reza. "Gain enhancement for circularly polarized double layered printed hemispherical helical antenna arrays." Journal of Electromagnetic Waves and Applications 29.10 (2015): 1342-1353.

54. Xia, Minghua, and Sonia Aissa. "On the efficiency of far-field wireless power transfer." IEEE Transactions on Signal Processing 63.11 (2015): 2835-2847.

55. Roberson, B. Race, et al. "Effects of Magnetic Nozzles and a Downstream Antenna to the High-Power Helicon Thruster." 52nd AIAA/SAE/ASEE Joint Propulsion Conference. 2016.

56. Murakami, Nao, et al. "Downstream Flow Analysis of High-Power Helicon Double Gun Thruster with Application to Spacecraft Propulsion Systems." 50th AIAA/ASME/SAE/ASEE Joint Propulsion Conference. 2014.

57. Randolph, T., et al. "Facility effects on stationary plasma thruster testing." 23rd International Electric Propulsion Conference. 1993.

58. Goebel, Dan M., and Ira Katz. Fundamentals of electric propulsion: ion and Hall thrusters. Vol. 1. John Wiley & Sons, 2008.

59. Lieberman, Michael A., and Allan J. Lichtenberg. "Principles of plasma discharges and materials processing." MRS Bulletin30.2 (1994): 899-901.

60. Conway, G. D., A. J. Perry, and R. W. Boswell. "Evolution of ion and electron energy distributions in pulsed helicon plasma discharges." Plasma Sources Science and Technology 7.3 (1998): 337.

61. Brown, Daniel L., et al. "Recommended practice for use of Faraday probes in electric propulsion testing." Journal of Propulsion and Power 33.3 (2016): 582-613.

62. Walker, Mitchell, Richard Hofer, and Alec Gallimore. "The effects of nude Faraday probe design and vacuum facility backpressure on the measured ion current density profile of Hall thruster plumes." 38th AIAA/ASME/SAE/ASEE Joint Propulsion Conference & Exhibit. 2002.

63. Sudit, Isaac D., and Francis F. Chen. "RF compensated probes for high-density discharges." *Plasma Sources Science and Technology* 3.2 (1994): 162.

64. Castro, R. M., et al. "A comparative study of single and double Langmuir probe techniques for RF plasma characterization." *Contributions to plasma physics* 39.3 (1999): 235-246.

65. Caneses, Juan F., and Boyd Blackwell. "RF compensation of double Langmuir probes: modelling and experiment." *Plasma Sources Science and Technology* 24.3 (2015): 035024.

66. Yu, Pengcheng, et al. "Double flush-mounted probe diagnostics and data analysis technique for argon glow discharge plasma." *Review of Scientific Instruments* 88.1 (2017): 013502.

67. Hofer, Richard R., Mitchell LR Walker, and Alec D. Gallimore. "A Comparison of nude and collimated Faraday Probes for Use with Hall Thrusters." *27th International Electric Propulsion Conference*. Fairview Park, OH: Electric Rocket Propulsion Soc., 2001.

68. Stratakos, Yorgos, Angelos Zeniou, and Evangelos Gogolides. "Electromagnetic simulation of helicon plasma antennas for their electrostatic shield design." *Journal of Vacuum Science & Technology A: Vacuum, Surfaces, and Films* 34.3 (2016): 031307.

69. Stratakos, Yorgos, Angelos Zeniou, and Evangelos Gogolides. "Comparison of helical and helicon antennas as sources of plasma excitation using a full wave 3D electromagnetic analysis in vacuum." *Plasma Processes and Polymers* 14.4-5 (2017): 1600107.

70. Afsharmanesh, M., and M. Habibi. "A Simulation Study of the Factors Affecting the Collisional Power Dissipation in a Helicon Plasma." *IEEE Transactions on Plasma Science* 45.8 (2017): 2272-2278.

71. Soltani, B., M. Habibi, and H. Zakeri-khatir. "The effect of Landau damping on the power absorption in a helicon plasma source driven by an m= 0 antenna." *Contributions to Plasma Physics* 57.9 (2017): 362-372.

72. Chavers, D. Gregory, et al. "Momentum and heat flux measurements using an impact target in flowing plasma." *Journal of propulsion and power* 22.3 (2006): 637-644.

73. Vereen, Keon, et al. "An Active Debris Removal Mission using a Plasma Phased Array Architecture." 2018 AIAA SPACE and Astronautics Forum and Exposition. 2018.